$^{18}O + {}^{18}O$ REACTIONS

Thesis by

Ren-Feng Yuan

In Partial Fulfillment of the Requirements

for the Degree of

Doctor of Philosophy

California Institute of Technology

Pasadena, California

1988

(Submitted July 24, 1987)

ACKNOWLEDGMENT

It has been a great pleasure and privilege to learn physics from my advisor, Professor C. A. Barnes, whose guidance, encouragement, and calm diplomacy made this work possible.

I am deeply grateful to all of the faculty, staff, and students of the Kellogg Radiation Laboratory, who provide a helpful and stimulating atmosphere. Special thanks are due Dr. J. Thomas and Dr. S–C. Wu for many helpful discussions.

ABSTRACT

Cross sections for the $^{18}O + ^{18}O$ reactions (fusion, inelastic excitation and transfer reactions) have been determined in the range $6.73 \leq E_{c.m} \leq 13.24$ MeV by measuring the low–lying γ–ray transitions in the residual nuclei with a high resolution Ge detector. A statistical model calculation of the populations of the residual nuclear states was employed in deducing cross sections from the measured γ–yields. γ–ray angular distributions were determined at $E_{lab} = 20.0$ MeV. The total fusion cross sections were compared with an IWBC calculation employing a parameter set obtained from fitting elastic scattering data. The interaction barrier shape has been obtained by means of the BKN inversion procedure and compared with the barriers for other oxygen isotopes. The inelastic scattering cross section and the two–neutron transfer reaction cross section are reproduced well by the DWBA approach.

TABLE OF CONTENTS

LIST OF TABLES

LIST OF FIGURES

CHAPTER I

Heavy Ion Reactions

I.A Physical Description

Heavy ion reactions have captured the interest of many nuclear physisists over many years. During that time the increasing availability of heavy–ion accelerators and appropriate experimental techniques caused an impressive growth of new experimental data, which, in turn, has sparked new ideas and insights into the reactions. A heavy ion reaction is one of the more drastic processes that may re–arrange the nuclear many–body system. This re–arrangement makes it possible to search for information on both nuclear structure and nuclear reaction mechanisms:

(1) What happens when the two nuclei are approaching each other? What is the mechanism of nuclear dissipation while they are overlapping? What is the relaxation process if a compound system is formed?

(2) How are these processes linked to the structure of the two nuclei and to the interaction potential between them? How many degrees of freedom are brought into play in their interactions? How do the coupling of other degrees of freedom to the one dimensional relative motion affect the quantum tunneling?

With these questions in mind we have studied sub–barrier $^{18}O + ^{18}O$ reactions. This thesis will present measurements of various $^{18}O + ^{18}O$ reactions, and investigate several factors which may affect the reactions. They are : (1) shell effects in the entrance channel, (2) role of valence neutrons in the fusion reaction, (3) fusion enhancement due to the nuclear deformation and due to coupling of transfer and inelastic reactions, and (4) nuclear cluster behavior in ^{18}O during the collision. This Chapter will provide a brief general description of the heavy ion reaction,

and discuss the physical background which is related to the technique employed to measure the cross sections of the different reactions.

In the simplest treatment, the heavy–ion reaction is considered as the collision of two structureless sphere–like particles interacting through a one–dimensional potential V(r). r is the distance between the centers of the two ions. V(r) is the sum of $V_C(r)$, the long–range electric repulsion, and $V_N(r)$, the short–range nuclear interaction.

$$V(r) = V_C(r) + V_N(r) \begin{cases} > 0, & for \quad r > R_t \ ; \\ < 0, & for \quad r \leq R_t \ . \end{cases} \tag{1.1}$$

where $R_t = R_1 + R_2 + d_0$, R_1 and R_2 are radii of the two nuclei, d_0 is possitive correction term, which is related to variation of the nuclear potential near the surfaces of the nuclei. Fig.1 shows an example of such a potential.

This barrier–well potential plays an essential role in heavy ion reactions especially at energies under and near the top of the barrier. The potential can be a trap for positively charged particles in the negative energy well, while it repells ions outside from entering the attractive region. These aspects of the potential curve are responsible for the shapes of cross sections for incident energies around the Coulomb barrier. At energies far below the barrier, reaction cross sections rise roughly exponentially with increasing energy because of the barrier penetration factor. As the kinetic energy, E, in the center–of–mass system reaches and passes over the barrier, E_B, the cross sections exhibit a roughly linear increase with energy. At high energies, $E \gg E_B$, other reaction mechanisms become dominant and fusion cross section decreases.

Although the heavy ion reaction is a problem that must be dealt with by quantum mechanics, a semi–classical orbit theory (see, for example, Ho 78) suffices to

explain its obvious characteristics. Fig.2 shows an overall classification scheme for a nuclear collision. It is based on the classical concept of a well–defined impact parameter. However it must be kept in mind that there is a small spreading of the wave packet about the classical trajectory, and the shape of the intermediate dinuclear complex develops with increasing classical interaction time. For energies below the Coulomb barrier the reactions, which are energetically forbidden in classical mechanics, proceed purely by the quantum tunneling effect.

As the impact parameter b decreases from case 1 to case 4 in fig.2, the overlapping of the two nuclei increases, which increases the nucleon exchange, energy damping, reaction time and equilibration of the reacting system. The reactions can be roughly classified as pure Coulomb interaction in case 1, nuclear elastic and inelastic scattering and few–nucleon exchange in case 2, deep–inelastic reaction in case 3, and fusion reaction in case 4. In the region known as 'light heavy–ion physics', *i.e.*, in the mass region $9 \leq A \leq 40$, the reaction mechanism is usually divided into only two extreme cases: direct and compound nuclear reactions. The first category corresponds to case 2 in fig.2. The reaction products are mainly peaked in the forward direction. The outgoing nuclei are not very different from those before the reaction. The time scales are of the order of the Rutherford scattering time scale. The compound processes occur when nuclei mingle closely so that kinetic energy is completely damped, and transferred to excitation energy of the compound nucleus. The compound nucleus has little in common with the original configuration; it undergoes deexcitation, usually leading to evaporation residues.

The angular momentun l in quantum mechanics corresponds to the impact parameter b in classical mechanics with the formula :

$$\sqrt{l(l+1)} \;=\; b\, K_\infty \tag{1.2}$$

where K_∞ denotes the wave number of the initial (asymptotic) relative motion. At low energies, the reaction cross section is dominated by the Coulomb barrier penetration factor. Because the centrifugal potential for small values of l, which corresponds to $b \sim 0$ from (1.2), is small, at low energies only those waves with small l will be able to penetrate the barrier to form a compound nucleus. In other words, the fusion cross section constitutes the main part of the reaction cross sections at low energies until the maximum geometrical overlap is reached. Beyond this maximum, higher partial waves may penetrate the interaction barrier, but the incident flux is significantly depleted by exit channels such as inelastic scattering and nucleon exchange. The total reaction cross section then becomes a linear function of $1/E_{c.m}$, and the fusion cross section starts to drop below and deviate from the reaction cross section, $\sigma_f < \sigma_R$. Complete theoretical treatments were done by, for example, U.Mosel and P.Fröbrich (Mo 85 and Fr 84); an example is illustrated in fig.3.

For S–wave point–like particles the fusion cross section at sub–barrier energies is proportional to the penetration probability and inversely proportional to the energy:

$$\sigma_f(E) \;\propto \frac{1}{E} e^{-2\pi\eta} \tag{1.3}$$

where η is the Sommerfeld parameter :

$$\eta \;=\; \frac{Z_1 Z_2 e^2}{\hbar v} \tag{1.4}$$

Although all heavy ion systems exhibit roughly exponential dependence of σ_f on energy E, the cross sections predicted by (1.3) rise too rapidly with energy. This is because the ions have finite sizes, and the distances of closest approach for pairs of heavy ions may be comparable to their nuclear radii. Moreover S–waves are not the only ones that participate in fusion reactions, higher partial waves make significant contributions to $\sigma_f(E)$ as the energy increases. Fig.4 displays the relative contributions of different partial waves to the total fusion cross section in the $^{18}O + {}^{18}O$ reactions. One usually defines the S–factor as :

$$S(E) \;=\; E \;\; \sigma_f(E) \;\; e^{2\pi\eta} \tag{1.5}$$

to have the S–wave barrier penetrability energy dependence factored out of the cross sections, and to show the deviations among experimental data and various model calculations.

I.B Methods of Measurements

In fig.5 we have a schematic representation of the products of a fusion reaction involving 'light heavy ions' at the energies near the Coulomb barrier. The primary deexcitation stage involves the emission of neutrons, protons, alpha and other charged particles, and gives the evaporation recoils their angular distribution. For reactions involving moderately heavy nuclei ($A > 40$), since only a small transverse momentum is imparted to the recoiling nuclei by the evaporated light particles and γ–rays, the fast–moving evaporation residues are emitted in a small cone about the beam line. However in the light heavy–ion reactions, since the masses of the recoil nuclei may be comparable with these of the emitted particles, the laboratory angular distribution of the evaporation residues is much more spread out. The particle

emission in fusion reactions is generally assumed to be isotropic in the center–of–mass system, since it is a characteristic of a statistical model, although angular momentum considerations may make the emission non–isotropic. The emission of particles continues during the first $\sim$ 10^{-18} sec, until this process becomes energetically impossible. Then the excited residual nuclei take typically 10^{-15} *to* 10^{-3} sec to complete complex γ–ray cascades to reach their ground states. Finally, the ground state nuclei may undergo $\beta^{\pm}$–decay if they are not stable with respect to $\beta^{\pm}$–decay.

The experimental measurements are based on the ideas mentioned above.

I.B.1 Detection of the residues with a $\frac{\Delta E}{\Delta X}$ – E technique has been successful at bombarding energies well above the Coulomb barrier, since the kinetic energies of the residues are relatively large and the reaction cross sections are relatively high, compared with elastic scattering. Another method to detect fusion residues is to separate the recoiling fusion residues from beam particles, which may be ten to fourteen orders of magnitude larger, by using combinations of electrostatic and/or magnetic deflectors, velocity filters and a ΔE–E counter telescope.

I.B.2 The emitted charged particles may be detected and identified by counter telescopes, usually consisting simply of a very thin solid–state $\frac{\Delta E}{\Delta X}$ detector and a residual energy detector. Neutrons have been detected by a long–counter or by a time–of–flight system. The charged particles normally consist mainly of continuous spectra, corresponding to high–density excited states of residual nuclei. Since there is no way to tell whether such particles come from single particle emission, or from emission of two or more particles, double counting is a difficult problem. The neutron detection may also be inherently limited by the risk of double counting. This method bas been used successfully to study reactions with single particle

emissions such as $^{12}C + ^{12}C$ and $^{16}O + ^{16}O$ at very low energies. Corrections for double–counting can be estimated for work at higher energies.

I.B.3 The prompt gamma–ray method is to observe the low–lying transitions of the evaporation residue cascades. These transitions are typically in the 300 keV–3000 keV range, where the full energy peak efficiency of intrinsic Ge or Ge(Li) detectors is reasonably large. Then the residual nuclei are identified by their characteristic gamma rays in prompt gamma spectra. With energy resolution of about 2.0 keV it is usually possible to complete the identification of most if not all fusion residues from the complex prompt gamma–ray spectra. To extract the production rates of residual nuclei from the integrated yields of these gamma peaks requires information about the level structure, branching ratios, and relative populations of excited states in the reactions. The latter were determined in somewhat model–dependent calculations. Chapter III will illustrate some details of these points in the measurement of the $^{18}O + ^{18}O$ reactions.

I.B.4 The residual radioactivity method is useful to determine the cross sections for those residual nuclei which are $\beta^{\pm}$ unstable. The measurements are performed by detecting their daughter nuclei γ–rays. The details of this method will be also described in Chapter III.

I.B.5 Elastic scattering measurements can be used to extract the total reaction cross section, at least, in principle. The total amplitude for elastic scattering $f_{el}(\theta)$ is the sum of the Rutherford amplitude $f_{coul}(\theta)$ and the nuclear compound–elastic amplitude $f_N(\theta)$:

$$f(\theta) = f_{coul}(\theta) + f_N(\theta) \tag{1.6}$$

The total nuclear interaction cross section, σ_N, is the sum of the reaction cross section, σ_R, and nuclear elastic scattering cross section,σ_N^{el}

$$\sigma_N \;=\; \sigma_R \;+\; \sigma_N^{el} \;=\; \sigma_R \;+\; \int [\sigma_{el}(\theta) - \sigma_{coul}(\theta)] d\Omega. \tag{1.7}$$

where $\sigma_{el}(\theta)$ is the total differential elastic scattering cross section, determined by experiment. $\sigma_{coul}(\theta)$ is the calculated Rutherford cross section. Since nuclear matter is distributed in a small but finite geometrical region, the integration is only performed over the range $\theta \geq \theta_0$, where

$$\theta_0 \sim 1/l_{grazing} \tag{1.8}$$

The impact parameter $b_{grazing}$, coresponding to the $l_{grazing}$, is illustrated in fig.2. Thus we have an expression for the reaction cross section(Tr 80, Ho 65):

$$\begin{aligned} \sigma_R \;=\; & 2\pi \int_{\theta_0}^{\pi} [\sigma_{coul}(\theta) - \sigma_{el}(\theta)] \sin\theta d\theta \\ & -4\pi \left| f_N(0) \right|^2 \sin^2(\theta_0/2) \\ & +4\pi\lambda Im\{ f_N(0)\, exp[2i\eta \ln \sin(\theta_0/2) - 2i\delta_0] \} \end{aligned} \tag{1.9}$$

where δ_0 is the Coulomb scattering phase shift for $l = 0$. $f_N(0)$ is the nuclear scattering amplitude evaluated at $\theta = 0°$, which tends to be quite small, since the high Coulomb barrier makes compound nuclear scattering small. If $f_N(\theta)$ is neglected, (1.9) becomes

$$\sigma_R \;\approx\; 2\pi \int_{\theta_0}^{\pi} [\sigma_{coul}(\theta) - \sigma_{el}(\theta)] \sin\theta d\theta \tag{1.10}$$

For identical particles eqn (1.9) must be modified to :

$$\sigma_R \;\approx\; 2\pi \int_{\theta_0}^{\pi/2} [\sigma_{Mott}(\theta) - \sigma_{el}(\theta)] \sin\theta d\theta \tag{1.11}$$

The principle of this method is to measure the flux lost from the elastic channel due to nuclear reactions. This method results in the sum of all reactions, such as fusion reactions, inelastic scattering or transfer reactions. In the low energy region $E \leq E_{limit}$, (for example, $E_{limit} \sim 5.5$ MeV for $^{12}C + ^{12}C$) the reaction cross section rapidly becomes smaller as the energy is lowered, and eqn. (1.10) involves the subtraction of two very large quantities to obtain a small one. So the application of this method is severely limited by the available accuracy of the experimental cross section $\sigma_{el}(\theta)$.

I.C Reactions Between Oxygen Isotopes

The first pair of nuclei among the oxygen isoptopes that has been studied is $^{16}O + ^{16}O$. This reaction is believed to be important in the stellar nucleosynthesis and stellar evolution (Ba 85). According to the shell model, ^{16}O is a doubly magic nucleus; both proton and neutron p–shells are completely filled. In fact, no low–lying excited state is found in ^{16}O since it is such a strongly bound nucleus. ^{17}O may be described as an ^{16}O core plus a valence neutron. As the shell model predicts, ^{17}O has spin 5/2 in its ground state, where the valence neutron populates the lowest state ($d_{5/2}$) in the s–d shell. The excited states of ^{17}O are those expected from the naive shell model with spin–orbit coupling.

^{18}O is the heaviest nucleus among the stable oxygen isotopes . ^{18}O, with ^{18}F and ^{18}Ne, form an attractive system for the study of nuclear structure in that they make it possible to study both charge symmetry and charge independence of the nucleon–nucleon interaction, as well as the interplay of the single–particle and deformed collective–quadrupole degrees of freedom (Aj 78 and Ga 83). Indeed the coexistence of two–neutron shell model states and core–excitation deformed

states is well established in ^{18}O. For example the ground 0^+ state results mainly the coupling of $(d_{5/2})^2$, the first excited 2^+ state is a mixture of $(d_{5/2})^2$ with a small component of $(s_{1/2}d_{5/2})$. The 0_2^+ state (at 3.63 MeV) is a four particle, two hole state. The presence of a dinuclear molecular component, $\alpha + {}^{14}C$, has been suggested in ^{18}O, and two broad $\alpha - {}^{14}C$ resonances with centroids at 9.33 and 9.65 MeV were recently observed via the inelastic scattering of ^{18}O on a ^{12}C target (Ra 84). The contribution of ^6He exchange to the elastic scattering cross section of $^{18}O + {}^{12}C$ has also been reported.

Fig.6 shows the energy levels of ^{17}O and ^{18}O with the decay theshold into ^{16}O + neutron(s) as zero energy.

The coexistence of single–particle, collective–quadrupole, and cluster degrees of freedom in ^{18}O complicates the determination for the $^{18}O + {}^{18}O$ reactions of the coupling of these degrees of freedom. It was expected that more exit channels would be open for $^{18}O + {}^{18}O$ and that the reaction mechanism might be, to some extent, different from the reaction mechanisms between ^{16}O and ^{17}O nuclei. In this thesis chapter II is devoted to descriptions of our experimental measurements; chapter III provides the details of the data analysis; chapter IV is about the calculation of compound nuclear models. The last chapter will present all the results in our $^{18}O + {}^{18}O$ experiment and compare the data with those from $^{16}O + {}^{16}O$, $^{17}O + {}^{16}O$ and $^{18}O + {}^{16}O$ studies.

CHAPTER II

Experimental Arrangement and Procedure

II.A Apparatus

The $^{18}O + {}^{18}O$ reactions were induced by an energetic ^{18}O beam on an ^{18}O target in the target chamber. The ^{18}O beams were delivered by the Caltech–ONR EN tandem Van de Graaff accelerator facility.

A duo–plasmatron ion source was used to generate the ^{18}O beam, and 98.1% enriched ^{18}O water vapour was directly introduced into the source. Since ^{16}O is present as the oxide, or in an adsorbed layer on the interior of the ion source, it often masks the ^{18}O beam in the output of the ion source. It was therefore important to carefully clean the plasma cone and all inside walls in the ion source head, before an experiment, and to provide a clean, short gas–supply line, to reduce the ^{16}O yield and maximize the ^{18}O beam from the ion source. It was found that the 30 degree ion–source bending magnet did not completely separate the ^{18}O component from the ^{16}O component. Complete separation was provided by the 90° post–acceleration magnet. The $^{18}O^-$ output from the ion source could reach 10—20 μa or more.

The beam energies used ranged from 14.0 MeV to 30.0 MeV in the lab system. This corresponds to energies approximately 6.7 MeV to 14.7 MeV in the center of mass system (after energy loss correction in the target). Beam energy steps of 0.5 MeV(lab) were selected so that the experiment would be sensitive to any intermediate structure in the cross section curves on an energy scale of $\geq$ 1 MeV. Charge state 4^+ was usually used in the measurements over most of the energy region. The 3^+ beam was used for the lowest beam energies and the 5^+ for the

highest beam energies. Beam currents on target ranged from 30 na at high energies to 2.0 μa at low energies.

Anodized tantalum sheets were employed as the targets. (In the next section the details of how to make such targets will be presented.) To prevent evaporation of the oxide layer under bombardment, the target was mounted on a flat flange, which served as a bored–out blankoff to provide a path for cooling water to come in and out. The cooling water, contacting the back of Ta sheet, removed the heat produced by beam bombardment of the target.

The target and its cooling system were electrically insulated from the accelerator beam pipe. The resistance between the target and gound was measured to be greater than $10^{10}\Omega$, so that leakage current to or from the target was negligible. A permanent magnet was placed 15 cm upstream from the target to suppress secondary electrons. This assembly formed a target/Faraday cup system, which was also used to collect beam current. The collected current was then fed to a current integrator circuit. Before each experiment, the integrator circuit was connected to a resistor and a battery with known voltage to check its calibration. The results were satisfactory. The accuracy of charge collection in the target chamber was found to be reliable, after we compared the currents collected when a permanent magnet (suppressor) was in place with those when it was removed. The beam collection and current integration were found to be accurate to better than $\pm 5\%$.

A copper gasket of the same diameter as the target was placed in front of the flat flange. The target was then mounted between the gasket and a knife edge on the target holder which was a tube of 15 cm length and 3 cm inside diameter. This seal formed an ultra–high vacuum target chamber with pressure below $0.6 \times 10^{-8}\ \tau$ (τ = torr). During bombardment the pressure increased slightly due to the heat

released in the target chamber by the beam bombardment. The typical vacuum during experiment was 0.6—3×10^{-8} τ, depending on the beam currents.

To maintain an ultra–high vacuum at the target is vitally important. This is because of possible carbon buildup on the target during runs. The Coulomb– barrier of the carbon+oxygen fusion reaction is lower than that of Oxygen+Oxygen, so the $^{12}C + {}^{18}O$ could severely interfere with measuring the $^{18}O + {}^{18}O$ yields even if only a small amount of carbon was accumulated on the target. The problem of carbon buildup is aggravated since the target has to be kept cool enough during bombardment to prevent its destruction. The solution of the vacuum cleanliness problem was to insert an in–line liquid nitrogen cold trap upstream of the target to separate the vacuum in the target region from the accelerator vacuum system, in which the vapour of diffusion pump oil and the presence of elastomer gaskets are the main sources of hydrocarbon vapour that would produce carbon build–up on the target. The ultra–high vacuum in the vicinity of target was ensured by an ion–pump that pumped the target region. An aperture of diameter 5.0 mm was placed in the pumping section to finally define the beam shape on target.

Fig.7 provides a schematic view of the experimental setup : cold trap, ion pump, target system and so on.

The γ–ray yields were measured by a 150 cm^3 intrinsic Ge detector. This detector was chosen because of its large active volume and because intrinsic Ge detectors are less easily damaged by neutrons than Ge(Li) detectors. It was mounted at 0 degrees relative to the beam line, and as close to the target as possible. A 32 mil Teflon insulator and a 70 mil lead absorber were inserted between the flat flange of the target holder and the Ge detector. The lead sheet was used for preferential

absorption of the very intense low energy X–rays and γ–rays. The total distance from the Ta target to the front of the Ge crystal was about 17.5 mm.

Two kinds of γ–ray spectra were recorded with two separate multichannel analysers (MCA). The first were the prompt γ–ray spectra, which were stored in a Tracor–Northern model 7200 4096 channel MCA. A 2048 channel MCA of the same type was used to record the beam–off γ–ray spectra beginning immediately after the beam was chopped off. Several of the exit channels resulting from the $^{18}O + ^{18}O$ reaction were found from the residual γ–activity measurements, when they could not be seen in the prompt γ–spectra since their yields were very small and/or prompt γ–peaks obscured the peaks from the radioactive decays.

The prompt γ–spectra and beam–off γ–spectra were then stored in the VAX–11–750 computer. Fig.8 and fig.9 show the examples of the two kinds of spectra.

The dead–time was kept below 10% at all times to preserve good energy resolution from the Ge detector. This was monitored by triggering a pulser, which was applied to the test input of the Ge detector, while the collected beam current was fed to the beam current integrating circuit. The pulser signal peak was also integrated to verify the dead time read from the MCA, which provided live time (LT), real time (RT), and then dead–time (RT – LT). By integrating the pulser signals peaks for the two cases: (a) beam on, and (b) beam off, the accuracy of the ratio LT/RT was then checked and found to be reliable to better than 3% .

The energy resolution from the Ge detector and electronics was checked to be about 2.0 keV for ^{60}Co E_γ=1.332 MeV. This was important because there were many exit channels in the $^{18}O + ^{18}O$ reaction, and thus many γ–ray peaks were present in the pulse–height spectra, which need to be well separated from each other for good accuracy of peak integration. Of course, good energy resolution was

specially required for clearly defining γ–peak regions as many of the γ–rays were Doppler shifted and Doppler broadened, and were far from the expected (approximately) Gaussian peak shapes.

There have been some concerns about whether the γ–rays emitted from the compound nucleus were distributed isotropically. 0° and the 90° γ–spectra measurements were made to find the answer to the question. The target was 4.0 inches from the front surface of the Ge detector in these anisotropy measurements. At this large distance only a small angle $\Delta\theta$ was subtended by the detector. The detection efficiencies in the two measurements were carefully checked with an ^{88}Y source. The final results have shown that the γ–ray distribution is not isotropic; however, most of the γ–rays of interest are anisotropic by no more than 20%. Effects of this small anisotropy are further reduced by the large solid angle of detection used for the data runs.

In all measurements, the Ge detector was heavily shielded from room background γ–radiation by at least 10 cm of lead in all directions, except in the target direction, of course.

A constant consideration in the $^{18}O + {}^{18}O$ experiment was to limit neutron damage of the Ge crystal, and its attendant loss of energy resolution. It was necessary to monitor the neutron flux which was expected to be higher than in other heavy ion reactions studied here, because there are two valence neutrons in both target and incident nuclei. It was possible to estimate the neutron flux sufficiently accurately from the counts in the $^{18}O + {}^{18}O$ pulse–height spectrum peaks at 596 keV and 691 keV. These lines come from neutron inelastic scattering on ^{74}Ge, and ^{72}Ge, respectively.

$$^{72}Ge\,(n,n')\,^{72}Ge^{*}$$

$$^{74}Ge\,(n,n')\,^{74}Ge^{*}$$

The $^{72}Ge^{*}$ nuclei decay entirely by internal conversion, followed by X–ray emission. The $^{74}Ge^{*}$ nuclei deexcite mainly by emitting 596 keV γ–rays that may be absorbed in the detector. Each of these reactions formed a peak in the pulse–height spectra with a high energy tail, which corresponds to the collection of the recoil energies of the ^{72}Ge or ^{74}Ge nuclei, resulting from the neutron collisions. Those peaks areas were used to estimate the fast neutron flux.

For example, a 22.0 MeV(lab) ^{18}O beam with a total fluence $F = 10^{14}$ on the target produced A=6.3 $\times$ 10^4 counts in the 691 keV line. Then

$$A = 2.2 \;\; F \;\; \sigma_f \;\; N_{target} \frac{1}{M_n} \frac{\Delta\Omega}{4\pi} \tag{2.1}$$

The factor 2.2 is the average number of neutrons produced in each $^{18}O+^{18}O$ fusion, which was obtained from both Hauser–Feshbach calculations and experiments. It will be discussed later. $\frac{\Delta\Omega}{4\pi}$=0.25 is the geometric efficiency for $\theta_{max} = 59.0°$, the maximum angle spanned by the crystal of the Ge detector. σ_f = total fusion cross section at the beam energy. $N_{target} = 0.44 \times 10^{18}/cm^2$ is the target thickness. With one count in the 691 keV line, the total number of neutrons which were produced in $^{18}O + ^{18}O$ reactions and reached the front surface of the Ge crystal is about:

$$M_n = 300 \; neutrons \; per \; count \tag{2.2}$$

or 10 neutrons per cm^2 in the detector. With this information, the total neutron fluence, Φ_n, was kept at or below 10^5 neutrons per cm^2 for the measurements at each beam energy.

The details of the efficiency of the γ–ray detection are presented in II.C. γ–ray identification and γ angular distribution are presented in III.A and III.B.

II.B Target and Target Thickness Measurement

Studies of the $^{18}O + {}^{18}O$ reactions require the use of a very stable and compact Oxygen-18 target with an appropriate thickness which could be accurately determined. Besides that, contamination with carbon, oxygen–16, and other low-Z elements in the target must be kept to the lowest possible level.

Initially it appeared that the most promising target would be $W\,{}^{18}O_3$ evaporated onto a gold backing. However, it was soon found that the stoichiometry of the oxide was not stable when bombarded by beam from the accelerator.

In the present experiment we have adopted the method to make ^{18}O targets pioneered by J.Pringle (Pr 72 and Ph 76), in which tantalum metal is anodically oxidized in an electrolyte made up with isotopically enriched ^{18}O water. Tantalum sheets from Morton Thiokol, Inc., 99.5% pure, were chosen as the metal to be anodized. The strength of Ta is enough to seal the high vacuum system of the target chamber. We verified by experiment that the purity of tantalum is sufficient for our experiment, and that the ^{18}O tantalum oxide layer is very stable during bombardment. Another advantage of tantalum is that the anodized targets are uniform in thickness and can be made to the desired thickness. That point is important because we need a layer of ^{18}O nuclei sufficient thick to do the experiment in a reasonable time; on the other hand, we wish the correction due to beam energy loss in the target to be as small as possible. The possibility of controlling the target thickness made it possible to reach a satisfactory compromise.

At the beginning, several disks of diameter 48.0 mm were punched from the 0.25 mm thick tantalum sheet. These were then chemically treated as described in the following polish procedure :

1. 10 minutes in hot trichlorethylene to remove grease.

2. 30 minutes in concentrated HNO_3 to strip any other metal or metal salt from the tantalum surfaces.

3. 10 seconds in the usual 5:2:2 mixture of concentrated sulfuric, nitric and hydrofluoric acids. This is the main chemical polishing process.

4. The next step was a stripping process. The tantalum surface layer was stripped again by inserting the tantalum disks into HF reagent, saturated by NH_4F to remove fluoride contamination or any remaining oxide layer from the tantalum disks.

5. Rinse disks in distilled water.

To minimize any possible contamination on the polished surfaces the disks were oxidized in the anodizing cell as soon as possible after the chemical polishing process. The anodizing apparatus is shown in fig.10. The cell was made of Lucite, and about 1.6 ml of enriched ^{18}O water was placed in the round well shown, with inner diameter 1.6 cm. Approximately 3 mg of KI was added to bring the concentration to about $0.01N$ KI. This particular electrolyte was chosen because the anion contains no oxygen, and the salt crystallizes without water of hydration.

The ^{18}O water from Isotec, Inc. was enriched to 98.12 atom % .

Composition :

OXYGEN–18	=	98.12 *atom* %
OXYGEN–17	=	0.54 *atom* %
OXYGEN–16	=	1.34 *atom* %

A negative DC supply was connected to a Ta–ring to make it the cathode. The Ta discs were connected to ground potential as the anode. The anodizing current was controlled at a constant 1.6 ma. The thickness of target during the anodizing process is roughly proportional to the final voltage drop between the

anode and cathode, from which we can monitor the thickness of the ^{18}O target. For example, a final voltage drop of 50 volts corresponds to an ^{18}O thickness of about 7.0 $\mu g/cm^2$. The uniformity of the target thickness could be checked by the colours on the tantalum surface, which were directly related to the thickness of the oxide layer on the tantalum disks. Fig.10 shows the detail of the anodizing apparatus.

Anodic tantalum oxides produced in this manner are homogeneouus, extremely uniform in thickness, and stoichiometric. The thicknesses of the targets used in our experiment were from 7.0 μg to 20 $\mu g\ /cm^2$ of ^{18}O. It usually took about one hour to make a target, and about 0.1 ml water was exhausted per target made in that manner.

The tantalum oxide layer, however, has a relatively high sputtering rate and so the target could degrade during beam bombardment. The cure for this problem was to evaporate about 160 $\mu g\ /cm^2$ of Au onto each target; this was sufficient to retain the low energy sputtered ions. The Au evaporation was carried out in a big bell jar with a vacuum of 10^{-6} Torr. A cold trap separated the diffusion pump from the bell jar to reduce the possibility of the diffusion of pump oil vapour into the evaporation system.

The stability of targets made in the way can be verified from the thickness measurements as listed in the following table:

TARGET THICKNESS ^{18}O $\mu g/cm^2$				
Date	gamma 1	gamma 2	gamma 3	Average
July/9/86*	13.00	12.85	13.75	13.20
Sept/12/86	13.12	12.91	14.05	13.36
Oct/4/86**	13.15	12.45	12.94	12.89

* (measured at beginning of exp.)
** (measured after exp. totally done)

The three gamma–rays, the peaks of which were integrated from the $^{16}O + ^{18}O$ reaction (the γ–spectrum of $^{16}O + ^{18}O$ is plotted in fig.11), are

gamma 1 = 1273 keV from ^{29}Si

gamma 2 = 2028 keV from ^{31}P and ^{29}Si

gamma 3 = 2230 keV from ^{32}P and ^{32}S

The maximum deterioration of the target after $50mC$(milli– Coulomb) Oxygen beam bombardment (total dosage on the target above) was less than 4%.

The determination of the target thickness is another interesting challenge to experimentists. In similar experiments in our laboratory with ^{16}O, J.Thomas employed Rutherford backscattering of ^{16}O ions at 20 MeV (lab). The effect of the tantalum oxide on the Ta surface is to reduce the density of Ta, and this can clearly be seen as a small step in height of the ^{16}O backscattering spectrum. Then the target thickness can be estimated from the energy width of the step and published stopping power ($\frac{dE}{dX}$) data.

We took a different approach to the problem. The essential idea is that we want to count the nuclei in a special calibration target directly instead of determing the indirect effect of the oxygen in the targets, to achieve better accuracy for the oxygen layer thickness. Then we could transfer the thickness of the calibrated target to that of the $T_a - ^{18}O$ target which will be used in the $^{18}O + ^{18}O$ experiments. An aluminum–backed $W\,^{16}O_3$ target was chosen as the special calibration target.

The whole process is divided into two steps:

First, we made an aluminum–backed $W^{16}O_3$ target by evaporating tungsten oxide onto aluminum foil, and its target components were studied by 2.0 Mev (lab) α-particle backscattering. An oxygen peak distinctly appeared on the aluminum background. See fig.12.

The ^{16}O thickness in the $W^{16}O_3$ target can be determined from the formula:

$$T_{16} = \frac{A}{Q_\alpha \frac{d\sigma(\theta)}{d\omega} \Delta\Omega} \tag{2.3}$$

Where A = yield of α–particle peak

Q_α = fluence of α–particles

$\Delta\Omega$ = solid angle

The Rutherford scattering cross section in the laboratory system is

$$\frac{d\sigma(\theta)}{d\omega} = \left(\frac{Zze^2}{mv^2}\right)^2 \frac{1}{\sin^4\theta} \frac{\left\{\cos\theta + \sqrt{1-(m/M)^2\sin^2\theta}\right\}^2}{\sqrt{1-(m/M)^2\sin^2\theta}} \tag{2.4}$$

where θ = *scattering* angle

m, z = *mass, charge* of incident particle α

v = *speed* of incident particle α

M, Z = *mass, charge* of target nucleus

The thicknesses obtained from the measurements at different angles were

$$T_{16}(\theta = 160.0°) = 27.4 \pm 2.1 \ \ \mu g/cm^2$$

$$T_{16}(\theta = 163.2°) = 27.8 \pm 2.1 \ \ \mu g/cm^2$$

They agree well with each other. The second step was to measure the $^{16}O + ^{18}O$ γ–spectrum when a 24.0 Mev ^{18}O beam was on the $W\ ^{16}O_3$ target. Afterward another $^{16}O + ^{18}O$ γ– spectrum was recorded while a 21.33 Mev ^{16}O beam was incident on the T_a–^{18}O target. The different beam energies were chosen so that the two $^{16}O + ^{18}O$ measurements were at the same center of mass energy, 11.29 MeV.

A simple and small correction for the energies lost in the two different targets was made. The difference of the effective energies in the two center of mass systems was found to be very small. Then the following relation may be used to find the ^{18}O thickness of the Ta–^{18}O target.

$$A1 = Q_{18} T_{16} \sigma(E_1) \eta \tag{2.5a}$$

$$A2 = Q_{16} T_{18} \sigma(E_2) \eta \tag{2.5b}$$

where A1,A2 = counts of the same γ–peak in the two cases

Q_1,Q_2 = total beam charge of ^{18}O and ^{16}O, respectively

T_{16},T_{18} = thichnesses of ^{16}O,^{18}O targets

σ = cross section, corresponding to the γ–ray of interest

E_1, E_2 = kinetic energies in the two systems after beam energy corrections

η = the detection efficiency for the γ–ray

Then we have for the ^{18}O target thickness

$$T_{18} = \frac{A2}{A1} \frac{Q_{18}}{Q_{16}} \frac{\sigma(E_1)}{\sigma(E_2)} T_{16} \tag{2.6}$$

The difference of E_1 and E_2 after the corrections of the beam energies lost in the targets is so small that a good approximation is that

$$\sigma(E_1) = \sigma(E_2) \tag{2.7}$$

in the vicinity of $E_{c.m}$=11.29 MeV, because of the small slope of the $^{16}O + {}^{18}O$ excitation curves in that energy region.

Thus we have simply, to a sufficiently good approximation,

$$T_{18} = \frac{A2}{A1}\frac{Q_{18}}{Q_{16}}T_{16} \tag{2.8}$$

The α–particle scattering on the $W^{16}O_3$ target backed by aluminum was performed in the 24.0 inches scattering chamber. The measurements were carred out twice at scattering angles of $\theta = 160.0°, 163.2°$ respectively. A surface–barrier semiconductor detector was used to detect the backscattered α–particles. The detector aperture of diameter $d_a = 0.0938 \pm 0.0002$ inches subtended a solid angle $\Delta\Omega = 1.209 \times 10^{-4}$ sr.

An upper limit for the ^{16}O contamination of the ^{18}O target can be determined by integrating the peak of the ^{29}Si and ^{31}P 2028 keV γ–ray in the spectra from the $^{18}O + ^{18}O$ runs. Even if all of the 2028 keV γ-rays were assumed to come from the reaction of the ^{16}O contamination on the ^{18}O target with the ^{18}O beam, the amount of ^{16}O in the ^{18}O target would not exceed 2.0%.

The signature of a carbon contamination in the ^{18}O targets would be the 390 keV γ–ray from ^{25}Mg, which is a product of an open channel for the $^{12}C + ^{18}O$ reaction, but not for the $^{18}O + ^{18}O$ reaction. No indication of the γ–ray could be found when the ^{18}O beam fluence on the target was less than 3 mC(milli Coulomb). The total carbon build-up after the $^{18}O + ^{18}O$ measurements were completed was found to be about 0.3 $\mu g/cm^2$ when the beam fluence reached 15 mC. In addition, the reaction $^{12}C + ^{18}O$ has been studied recently, and the relative yields of various γ–rays were used to estimate the ^{12}C impurity in the ^{18}O targets of the present experiment.

Summary:

The tantalum–^{18}O target made in the way described above has a number advantages:

a. The strength of the Ta sheets is enough to seal the high vacuum system.

b. The ^{16}O contamination was less than 2%, depending on the composition of the ^{18}O enriched water, from which the targets were made. The ^{16}O introduced in the anodizing process appears to be negligible.

c. The amount of ^{12}C in targets was very small. It could not be detected at the beginning of the experiment. However a small carbon build-up during the experiment was observed. It could possibly have been improved if the target was kept in the ultra–high vacuum target chamber instead of being exposed to the atmosphere between accelerator runs. Possibly some CO, CO_2 or other carbon containing material was adsorbed on the target surface while the target was exposed to the atmosphere.

d. The approach chosen to measure the target thickness was reliable. We did not need to rely on the published stopping power data ($\frac{dE}{dX}$) and on the assumption of the composition of tantalum and oxygen in targets(Ta_2O_5). The main error in the thickness determinations came from the statistical error in the integration of the γ– peaks. The total error in the ^{18}O target thickness is 8%.

e. The stability of the target under beam bombardment was satisfactory.

II.C Detector Efficiency

Absolute photopeak efficiencies for γ–transition energies in the range 276 keV$\leq$ $E_\gamma \leq$ 3250 keV were determined using several standard calibration sources with known branching ratios. Since the photopeak efficiencies are sensitive to the relative position of the sources and detector(a 1 mm shift of the source to detector distance

results in about 6% change in efficiency) the radioactive sources were placed in the same position as the target, with water in the cooling jacket and all other conditions, including the teflon sheet and the lead absorber similar to those when the data were taken.

The sources we used to calibrate the detector are

^{60}Co 0.994 μc on June/1/1986 $T_{\frac{1}{2}} = 5.26$ Yr

^{88}Y 1.045 μc on June/9/1985 $T_{\frac{1}{2}} = 106.6$ Ds

^{22}Na 0.089 μc on Nov/1/1975 $T_{\frac{1}{2}} = 2.603$ Yr

^{133}Ba 4.14 μc on June/3/1969 $T_{\frac{1}{2}} = 10.5$ Yr

^{56}Co 0.0107μc on Oct/17/1986 $T_{\frac{1}{2}} = 78.76$ Ds

^{125}Sb 0.252 μc on Oct/17/1986 $T_{\frac{1}{2}} = 2.70$ Yr

The γ–ray sources and their γ–rays energies of interest are listed in table 1.

The ^{56}Co source was produced by the reaction $^{56}Fe(p,n)^{56}Co$ in our own laboratory, with unknown intensity. However the intensity was found from the assumption that the photopeak efficiencies are related to the γ energies as

$$\eta_{eff} \sim \frac{1}{E_\gamma} \tag{2.9}$$

over the small energy range of $E_\gamma = 1173$ keV (^{60}Co), 1275 keV(^{22}Na), 1333 keV(^{60}Co).

With the known photopeak efficiencies of the three γ–rays listed above the ^{56}Co 1238 keV photopeak efficiency was found to be

$$\eta_{eff}(1238) = \frac{1}{3}\left(\eta_{eff}(1173)\frac{1173}{1238} + \eta_{eff}(1274)\frac{1274}{1238} + \eta_{eff}(1333)\frac{1333}{1238}\right) \tag{2.10}$$

From the peak area of the 1238.3 keV γ–ray the intensity of the ^{56}Co source was determined to be 0.0107 μc. In the same way, the strength of the ^{125}Sb source was determined to be 0.252 μc. The intensities of the two sources were measured on Oct/17/86.

The summing effect was considered when a source with cascade γ– decays was used to calibrate the detector efficiency. As an illustration the ^{60}Co peak area is

$$A_{1333} = I \times 3.7 \times 10^4 \times \exp(-\lambda \Delta T) \times [1 - \epsilon_t(1173)] \tag{2.11}$$

where

$$\lambda = 0.693 \times \frac{1}{T_{\frac{1}{2}}} \tag{2.12}$$

ΔT is the period from the time when the source was calibrated to the time when it was used to calibrate the efficiency of the detector.

The total detection efficiency of a γ–ray is estimated as

$$\epsilon_t(E_\gamma) = \int d\Omega \{1 - \exp[-\mu_a(E_\gamma)\, l(\theta,\phi)]\} \exp\left[-\sum_i \mu_i(E_\gamma)\, l_i(\theta,\phi)\right] \tag{2.13}$$

Where the $\mu_i's$ are the absorption coefficients of the γ–rays for all materials between the target and the front surface of the Ge detector active volume.

μ_a is the absorption coefficient of γ–rays for the element Ge.

$l(\theta,\phi)$ is the length of path through the crystal at the direction specified by θ *and* ϕ

$l_i(\theta,\phi)$ are the lengths of material between the target and the front surface of Ge detector active volume.

The curve of total efficiency versus gamma energy was normalized at the 661.0 keV energy point. We used the experiment–determined total efficiency of the γ–ray from a ^{137}Cs source, which has only one γ–ray with energy 661.0 keV.

The photoefficiencies determined with the sources are listed in the table 1. The curve of the photoefficiency versus E_γ is drawn in fig.13.

In this chapter and the chapters following, the absolute γ–ray abundances and branching ratios are taken from ref. (Aj 78, Bo 74, En 78 and Mi 78).

CHAPTER III

Data Analysis

III.A Identification of Reaction Channels

The recorded prompt γ–ray and residual radioactivity γ–ray spectra constituted a vast amount of information, from which it was possible to make a reliable identification of the most significant outgoing reaction channels. In some cases, it was of crucial importance for a correct identification and to get accurate integrated yields to know the Doppler shifts and Doppler broadening of the γ–lines. A typical $^{18}O + ^{18}O$ γ–spectrum at a beam energy 20.0 MeV is shown in fig.8. Table 2 is a complete list of γ–ray transitions, with their corresponding residual nuclei and their unshifted energies, originating from the $^{18}O + ^{18}O$ reactions. Also shown in the figure are the γ–rays produced by inelastic scattering on target constituents, or by the scattering or capture of neutrons (from the $^{18}O + ^{18}O$ fusion reactions) by surrounding material, especially by detector materials or shielding material. The γ–rays identified from residual radioactivity measurements are also listed in the table.

Since the Doppler effect plays an important role in analyzing the present experimental data, a simple model was developed to estimate the distortion of γ–peaks by the Doppler effect. In this model, we took the same target–detector geometry as in our experiment, and employed the $\frac{dE}{dX}$ data from Northcliffe and Schilling (No 70). The residual nucleus produced in the reaction was assumed to initially carry all of the momentum of the incident particle; γ–emission was assumed to be isotropic.

With the assumption given above, the momentum carried by the residual nuclei, at the moment they were produced, equals the momentum of the incident ^{18}O particle $P_{ion,0} = P_{inc}$, The kinetic energy of the residual nucleus (ion) is $E_{ion,0} = \frac{P_{ion,0}^2}{2M_{ion}}$ at the moment of its formation.

Of course, the momentum of the ion decreases with time because the ion loses its kinetic energy when moving through the target material. Simply,

$$E_{ion,t} = E_{ion,0} - \int_0^{X(t)} \frac{dE}{dX} dX \tag{3.1}$$

and

$$P_{ion,t} = \sqrt{2M_{ion}E_{ion,t}} \tag{3.2}$$

The γ–quantum energy E_γ at the detector is therefore a function of the angle θ, at which the γ–ray was emitted, and the time t between formation of the excited nucleus and γ–ray emission.

$$\frac{E_\gamma(\theta,t)}{E_\gamma^0} = 1 + \frac{P_{ion,t}}{M_{ion}c}\cos\theta = 1 + \beta(t)\cos\theta \tag{3.3}$$

where E_γ^0 is the unshifted energy of the γ–rays.

We ignore terms of higher than the first power in β since $\beta \ll 1$. The ion was assumed to be completely stopped after it lost 98% of its energy. The γ–absorption in the Ge detector is θ–dependent:

$$\eta(\theta) = 1 - e^{-\mu_a l(\theta)} \tag{3.4}$$

Summing over θ and t, we obtained the Doppler broadened and Doppler shifted shapes of the γ–peak. The results of such calculations for the nuclei ^{30}Si and ^{34}S at beam energy 20.0 MeV are plotted in fig.14. The shape for the ^{30}S 2236 keV γ–ray is quite similar to that observed from the $^{18}O + ^{18}O$ pulse height spectrum.

However, this is not the case for the ^{34}S 2127 keV γ–ray at high beam energies. This is caused by the fact that the ^{34}S nuclei have a large probability to be populated in highly excited states at high beam energy; they undergo many steps of cascade γ–decay before they reach their first excited state. Thus the ^{34}S nuclei lose most of their momentum before emitting 2127 keV γ–rays, and smaller Doppler effects are observed. As the beam energy is reduced, the ^{34}S nuclei are more likely to be populated in lower excited states. Thus the similarity between the model–calculated shape and the observed one for the ^{34}S 2127 keV γ–ray is restored.

With the nuclear level diagrams and the analysis of the Doppler shifts and spreading, the exit channels of the $^{18}O + {}^{18}O$ sub–barrier reactions observed in both prompt and residual γ–ray pulse–height specta were identified as follows:

(1) The ^{34}S + 2n exit channel : In the series of decays starting from the compound nucleus ^{36}S and leading to a variety of exit channels, the sequential neutron decay from ^{36}S to ^{34}S plays a major role as the trunk of a tree, from which many exit channels such as ^{33}S, ^{33}P, and ^{30}Si are branches. The nucleus ^{34}S was produced with large probability, mostly in high–lying excited levels, which de–excite almost exclusively by emitting charged particles. Only with a small probability is ^{34}S populated in low–lying excited states which decay to the ground state by γ–ray emission.

The 2127 keV γ–ray is dominant. It comes from the ^{34}S first excited state to ground state transition. The life–time of the ^{34}S first excited state, 0.28 ps, is so small that it is comparable with the stopping–time of ^{34}S ions in the target material (about 1.0 ps). Thus Doppler shift and broadening are observed in the prompt γ–spectra at low beam energies. However the higher the beam energy, the less the Doppler effects, as discussed above. A small correction must be made for the 2127

keV γ–ray yield because of the small contribution from the ^{34}P β^-–decay with a 15% branch to the ^{34}S 2127 keV state. This correction is about 6.5%.

The 1001 keV and 2561 keV γ–rays are in the cascade γ–decay that starts from the 5689 keV state and proceeds to the 4688 keV state, and then to the 2127 keV state, finally decaying to the ground state with the emission of a 2127 keV γ–ray. Another mode of deexcitation for the 5689 keV state is to emit a 1067 keV γ–ray to the 4622 keV state and then go to the first or the second excited states, while four γ–rays 2495 keV,1317 keV, 3304 keV and 1177 keV are emitted.

We have obtained the cross sections for this channel from both 2127 keV and 2561 keV γ–ray yields to check the reliability of the calculated population probabilities. We found the cross sections obtained from the two γ–yields to agree with each other very well. The error on the average is less than 15%. See fig.15.

(2) The ^{34}P + n + p , ^{34}P + d exit channels : ^{34}P is a neutron–rich radioactive nucleus with a short life–time, 12.6 sec. It is not a well–investigated nucleus; there are only 5 known excited levels in its level diagram, with incomplete information. Only two γ–rays (429.0 keV and 1891 keV) are assigned to ^{34}P. The 429 keV γ–ray is the transition from the first excited state to the ground state, and the 1876 keV γ–ray is likely to be the transition from the ^{34}P 2305 keV state to the 429 keV state. The possibility that these γ–rays come from other exit channels is excluded by the γ energies. In addition, the 1177 keV peak might be partly from the 1606 keV state to the 429 keV state transition.

(3) The ^{31}Si + n + α exit channel : The γ– transition from the second excited state at 1695.1 keV to the ground state characterized this exit channel. The 752.5 keV γ–ray emitted from the first excited state overlapped the high–energy tail of the ^{72}Ge 691 keV peak. The 1438 keV peak from the γ transition of the 3133

keV state to the 1695.1 keV state is close to the ^{33}P 1431 keV peak, interfering with the extraction of the yields.

(4) The ^{28}Mg + 2α exit channel : The 1474 keV γ–peak in the prompt $^{18}O + ^{18}O$ γ–spectra characterizes the residual nucleus ^{28}Mg as one of the products in the $^{18}O + ^{18}O$ fusion reactions. So do the 401 keV and 1342 keV γ–rays from ^{28}Al and the 1779 keV γ–ray from ^{28}Si in the residual spectra. Those γ rays are produced after ^{28}Mg β^-–decay.

(5) The ^{24}Ne + ^{12}C , ^{24}Ne + 3α exit channel(s):

This exit channel (^{24}Ne formation) was determined from the residual activity measurements. Along with the β^- decay chain, ^{24}Ne *to* ^{24}Na *to* ^{24}Mg, three γ–rays with energies 472.3 keV, 1369 keV and 2754 keV were observed. They were the evidence for the production of the nucleus ^{24}Ne in the $^{18}O+^{18}O$ reactions. However, only the yield of the 472.3 keV γ–ray was used to determine the production cross section of ^{24}Ne, while the yields of the others were not useful in calculating the cross section because they come from the nucleus ^{24}Na which has a large half–life, 15 hours.

(6) The ^{33}S + 3n channel: The nucleus ^{33}S could be populated in its first excited state with energy 840.4 keV. However the 840.4 keV γ–peak was severely blurred by several other γ–rays. One of these is the 834.95 keV γ–peak, with its high energy tail, from the second excited state of ^{72}Ge which was produced by neutron inelastic scattering on ^{72}Ge in the Ge detector . The reactions ^{56}Fe(n,n') and ^{27}Al(n,n') also contribute to this region with very close γ energies, 846.8 keV and 843.8 keV, respectively, where Fe is the main component of the target chamber and Al is the package material of the Ge detector. In addition to these contributions, ^{27}Mg undergoes β^- decay to ^{27}Al, which emits 843.8 keV γ–rays. With so many

γ–rays overlapping together, the γ–ray near 840 keV could not be used to find the ^{33}S production cross section.

The 967.3 keV and 1966 keV γ–rays were from the 2934 keV state. Both were analyzed to obtain the yield of the ^{33}S+3n channel. The life–time of the 2934 keV level, which emits 967.3 keV γ–ray in the transition to the 1966 keV state, is about 30 ps, much longer than the ion's stopping–time, so its γ–ray peak is narrow and Gaussian. But the 1966 keV peak was far from that shape because of its short life–time, 0.12 ps. The Doppler effect played an important role in determining its shape. The peak region of the 1966 keV γ–ray was carefully checked by comparing its shapes as detected in 0° and 90° γ–spectra measurements. It was found that this peak extended from 1966 keV to about 2050 keV. A 1982 keV peak from $^{18}O^*$ overlapped with the Doppler shifted and broadened peak region, but this was easy to handle since the ^{18}O peak has a nice, narrow Gaussian shape in the spectra.

The cross sections obtained from the 967.3 keV and 2934 keV γ–yields were found to agree with one another within 15%; however, they are about 35% higher than that derived from 1966 keV γ–ray yield. The cross section listed in table 5 for this channel is obtained from 1966 keV γ–yield because this peak has good statistics

.

A small peak at 1933 keV was the characteristic for the population of ^{33}S in its 4865.7 keV state, which emits that γ–ray to deexcite to the 2933.7 keV state.

(7) The ^{33}P + 2n + p exit channel : Two dominant lines of 1431.4 keV and 1847.6 keV come from the transition of the ^{33}P first and second excited states to its ground state. A small branch from the second excited state to the first excited state formed a small peak at 417 keV. In addition, there are two γ–decay cascades. They originate from the 5638 keV and 5453 keV levels, and emit 1412

keV or 1226 keV γ–rays, respectively. They reach the same 4227 keV state, which decays by 2777 keV γ–ray emission. ^{33}P could be also populated in the 3627 keV state with a γ–transition to the 1847.6 keV state. The energy is nearly the same as the 1778.9 keV γ–ray in ^{28}Si, which could be the product of ^{28}Mg β^- decay, or could come from the reaction of the ^{18}O beam with ^{12}C contamination in the target.

(8) The ^{30}Si + 2n + α channel : The 2235.5 keV transition in ^{30}Si appears strongly in the $^{18}O + ^{18}O$ γ–spectra, and shows Doppler broadening in the pulse–height spectra. The nuclei such as ^{31}P , ^{31}S , ^{32}S , *and* ^{32}P which could, in principle, emit γ–rays with energies close to the ^{30}Si γ–ray, were excluded from possible significant contribution to that peak area because of their unfavorable Q–values for $^{18}O + ^{18}O$. The integrated yield of this γ–transition was chosen to find the cross section for the ^{30}Si exit channel with good accuracy.

Other γ–rays, 1094 keV, 1263 keV, 2452 keV, 3044 keV, 3498 keV and 3715 keV formed several large or small peaks in γ spectra. All of them were apparently from the residual nucleus ^{30}Si, populated in higher excited states. The 3715 keV γ–ray, the highest observed in the energy region from 100 keV to 4000 keV, represents the transition from the 5950 keV state to the first excited state of ^{30}Si, followed by a 2235.5 keV γ–transition. The 1094 keV γ–ray comes from a transition from the 7.044 keV state(the highest state we isolated by γ–identification in the $^{18}O + ^{18}O$ reactions) to the 5950 keV state. This implies that ^{30}Si could be populated in still higher states with enough energy to emit one more neutron or proton to form new nuclei ^{29}Si and ^{29}Al. The experimental results validated this conjucture.

(9) The ^{29}Si + 3n + α channel : This channel has a simple γ–spectrum for $^{18}O + ^{18}O$ at subbarrier energies because only one γ–transition was found, which

came from the first excited state at 1273.3 keV. With a 0.28 ps life–time, the 1273.3 keV γ–ray was Doppler shifted and broadened. The second excited state could be reached only when the incident beam energy was as high as 25.5 MeV or higher.

(10) The ^{29}Al + n + d + α exit channel: Due to its small probability of production this channel could not be seen in the prompt γ–ray measurements. However, in residual radioactivity γ–spectra, a sharp peak at 1273.3 keV required the existence of the residual nucleus, ^{29}Al, which undergoes β^- decay to ^{29}Si with an 89% branch to the 1273.3 keV, first excited state. The life–time of the 1273.3 keV γ–ray was checked to be the life–time of ^{29}Al, about 7 min. This excluded possible contributions of this γ–peak from the nuclei ^{22}Na and ^{22}F, because they have very different life–times, although they undergo β–decay to ^{22}Ne and then emit a γ–ray with energy 1274.6 keV, very close to the ^{29}Al γ–ray energy.

(11) The ^{27}Mg + n + 2α exit channel : At high incident beam energy the ^{27}Mg first excited state was found with its 984.6 keV peak in the prompt γ–spectrum. But the probability of forming this channel was more reliably determined by examining the ^{27}Mg residual activity. The ^{27}Mg decays to ^{27}Al with the emission of 843.8 keV and 1014.5 keV γ–rays. The identification of ^{27}Mg was checked by verifying its half–life which was found to be about 9 min, in agreement with its known half–life, 9.46 min.

(12) The ^{18}O inelastic scattering channel : The ^{18}O nuclei in the beam or in the target could be excited by nuclear and Coulomb interaction to their 2^+, first excited state. Such excitation is then followed by γ–decay to the ground state. The cross section for producing $^{18}O^*$ was simply determined from the yields of the 1982.2 keV γ–ray, which show up in the prompt $^{18}O + ^{18}O$ γ–spectrum as a sharp peak superimposed on the 1966 keV, Doppler broadened peak from ^{33}S.

(13) The $^{20}O + ^{16}O$ exit channel: As a product of a two–neutron transfer reaction in the $^{18}O + ^{18}O$ system, the ^{20}O nucleus can be populated in its ground state or excited states. This was verified by the 1673.7 keV γ–ray which comes from the transition from the ^{20}O first excited state to its ground state. ^{20}O is unstable to β^- decay; it decays to the ^{20}F first excited state at 1056.9 keV. ^{20}F, in turn, β^- decays to the ^{20}Ne first excited state at 1633.8 keV. Therefore two γ–rays, with energies 1056.9 keV and 1633.8 keV were emitted along with the β^- chain. Both of the 1056.9 keV and 1633.8 keV γ peaks are well defined, and both were used for the calculation of the two–neutron transfer reaction cross section, with good agreement (see fig. 15).

(14) The $^{19}O + ^{17}O$ exit channel : A 1357 keV γ–ray would be a good indication of the one neutron transfer reaction; this γ–ray was produced after the decay of ^{19}O to ^{19}F, which emits γ–rays with energy 1357 keV. However this reaction was observed only at high incident beam energies.

(15) The $^{14}C + ^{22}Ne$ exit channel : The details of this channel are presented in section **V.D**.

III.B The Angular Distribution of γ–rays in $^{18}O + ^{18}O$

In reactions such as those studied in the present work, γ–rays angular distributions are usually assumed to be of the form

$$W_i(\theta) \sim 1 + a_i \cos^2\theta \tag{3.5}$$

where θ is the angle between the incident particle and the emitted γ–ray, and the a_i are coefficients that describe the departure from an isotropic distribution. The subscript i labels the γ–rays of interest. In principle, higher powers of $\cos\theta$ can

be present for multipoles higher than dipole. In most cases, previous particle or γ–ray emissions reduce the complexity of the angular distribution to $\cos^2\theta$, approximately. Odd powers of $\cos\theta$, arising from interference between states of even and odd parity, do not appear in the γ–ray angular distributions because the initial and final (bound) states have well–defined parity.

The compound nuclei are excited to the high energy region of overlapping states. Moreover, the beam energy resolution is much greater than the separation of the states; hence, the cross sections are averages over these states. The angular distributions of γ–rays tend to be reduced by the overlapping of many compound nucleus states with different J–values. Thus the distributions are not expected to be far from isotropic and the a_i's are expected to be small numbers. Generally, compound nucleus theory for the case of many overlapping resonances predicts approximate forward—backward symmetry for the particle emissions. As noted above, forward–backward symmetry for the γ–ray emission follows from the well–defined parity of the bound γ–emitting states.

Because the detector was far from the target during the measurement of the γ–ray angular distributions, the variation in the values of $\cos^2\theta$ over the detector was small enough that we could take W(0°) and W(90°) as representing the γ–rays yields when the detector was set at 0° or 90° respectively.

Thus the ratio of the γ–yields from the measurements at 0° and 90° is

$$\frac{Y_i(0°)}{Y_i(90°)} = \frac{Q(0°)}{Q(90°)}\frac{\varepsilon(0°)}{\varepsilon(90°)}\frac{T(0°)}{T(90°)}\frac{W_i(0°)}{W_i(90°)} \tag{3.6}$$

where $Q(0°)$ and $Q(90°)$ are the integrated beam charges.

$\frac{\varepsilon_i(0°)}{\varepsilon_i(90°)}$ is the ratio of the detection efficiencies of the i^{th} γ–ray in the two positions, which was determined to be very close to unity by looking at the ^{88}Y

γ–peaks at 898 keV and 1836 keV, for the two detection angles. The average values for the two γ–rays energies is $\frac{\varepsilon_i(0°)}{\varepsilon_i(90°)} = 0.98 \pm 0.03$. $\frac{T(0°)}{T(90°)}$ is the ratio of the target thicknesses at the two angles, which was was found to be 2.03.

As there was a small spread of the angle θ in the detector $\delta\theta \sim \pm 5°$, a tiny correction was made, although it could probably have been ignored.

$$\frac{W_i(0°)}{W_i(90°)} \doteq \frac{1 + a_i \cos^2(0° + \delta\theta)}{1 + a_i \cos^2(90° + \delta\theta)} \doteq \frac{1 + 0.98a_i}{1 + 0.02a_i} \simeq 1 + 0.96a_i \qquad (3.7)$$

The a_i coefficients are listed in the same table.

The conclusion can be drawn that most of the γ–rays in the $^{18}O + ^{18}O$ sub–barrier reactions differ from isotropy by less than $\pm 20\%$; only a few γ–rays were slightly outside these limits, and these were found to come from the de–excitation of higher excited states.

A nearly isotropic angular distribution of γ rays in fusion reactions is in agreement with the expectations of the statistical model. This occurs because of the fact that there are many partial waves participating in the reaction. In addition, further averaging occurs in the successive emissions of particles and gamma rays. However some exceptions can be expected since there might be a dominant resonance for a single partial wave at some particular beam energy and angular momentum.

An angular distribution measurement of the gamma–rays in the $^{18}O + ^{18}O$ reaction was performed at an incident beam energy 20.0 MeV. As the beam energy increases, the anisotropy may increase somewhat because the average orbital angular momentum of the compound nucleus increases with energy.

The γ–ray spectra at 0° and 90° are plotted in fig.16. The measured ratios, $\frac{W_i(0°)}{W_i(90°)}$, and coefficients, a_i, for these γ–rays of interest are tabulated in table 3.

III.C Effective Energy and Cross Sections

There are several reaction mechanisms in the $^{18}O + ^{18}O$ system. Fusion reactions are the dominant ones in the energy region of the present work. The characteristic gamma rays of the residual nuclei correspond to different partial cross sections for different outgoing channels. The yields of these γ–rays were used to obtain partial and total fusion cross sections. The ^{18}O nuclei in the beam and the ^{18}O nuclei in the target may also interact with each other and cause one (or both) to be excited to the first 2^+ state. At low energies this process is expected to be dominanted by Coulomb excitation, and, at high energies, by nuclear inelastic scattering. The third reaction mechanism is neutron transfer, in which one or two neutrons is(are) transferred from one of the ^{18}O nuclei to the other; resulting in the production of an $^{17}O + ^{19}O$ pair of nuclei or an $^{16}O + ^{20}O$ pair. However only the two neutron transfer reaction was observed at sub–barrier energies because of its small negative Q–value, Q=–0.628 MeV. The Q–value for one neutron transfer is Q=–4.068 MeV. The neutron transfer reactions were described by DWBA (Distorted Wave Born Approximation) in calculating excitation functions (curves of yield versus beam energy).

Because the beam graduately loses its kinetic energy while it is passing through the target, and at sub–barrier energies the cross sections fall so rapidly with decreasing energy, the beam reacts with higher probability with the outer half of the Ta–^{18}O target layer. The effective beam energy in the target should thus be slightly higher than the energy half way through the target, E_C. A suitable effective energy is defined by

$$E_{eff} = \frac{\int_{E_c-\Delta E}^{E_c+\Delta E} E\,\sigma(E)\,dE}{\int_{E_c-\Delta E}^{E_c+\Delta E} \sigma(E)\,dE}, \tag{3.8}$$

where ΔE is half of the energy loss in the Ta—^{18}O layer. It was found that the frequently–used simple analytic form for the cross section at sub–barrier energy, $\sigma(E) \sim \frac{1}{E} e^{-2\pi\eta}$ $(\eta = \frac{Z_1 Z_2 e^2}{\hbar v})$ is steeper than the experimental data for $\sigma(E)$. Instead, the experimental cross section was used in the formula (3.8), and assumed in the small energy region from $E_c - \Delta$E to $E_c + \Delta$E (about 270 keV) to be of the form,

$$\sigma(E) \sim \frac{1}{E_{c,i}} e^{K_i E} \tag{3.9}$$

The coefficients K_i were determined from the experimental curve of $\sigma(E)$. The calculated effective energies are listed in table 5. It was found that the E_{eff} was not far from E_C. In the worst case (lowest beam energy)

$$E_{eff} - E_C \simeq 12\ keV \tag{3.10}$$

which is about the size of the energy straggling, Ω. The fluctuation of energy loss in the gold layer, or energy straggling, is given in the modified Bohr theory (Ch 77b) by

$$\Omega^2 = f(Z_1, Z_2, E)\ \Omega_b^2 \tag{3.11}$$

and

$$\Omega_b^2 = 4\pi\ Z_1^2\ Z_2\ e^4\ Ng \tag{3.12}$$

where $Z_1 = 8$ is the atomic number of the projectile,$Z_2 = 79$ is the atomic number of gold, $Ng \simeq 7 \times 10^{17}$ atoms per cm^2 is the area number density of the gold layer on the surface of the target, and $f(Z_1, Z_2, E) \simeq 0.2$ is a correction coefficient to the Bohr formula. Ω is defined as the standard deviation of the energy broadening and is equal to the FWHM / 2.355. In the present experiment $\Omega \simeq 14$ keV. This value includes a small contribution from the TaO layer.

The cross section for inelastic scattering to the first excited state of ^{18}O was obtained from the yield of the 1982 keV γ–ray, Y_{1982}.

$$\sigma_{in}(E) = \frac{Y_{1982}}{N_t \ \phi \ \eta_{1982}} \tag{3.13}$$

The cross section for the two neutron transfer reaction could be determined from the yield of the 1057 keV γ–ray (^{20}F) or from the yield of the 1633 keV γ–ray (^{20}Ne). Both gave results in good agreement.

$$\sigma_{trans}(E) = \frac{Y_{1057}}{N_t \ \phi \ \eta_{1057}} \tag{3.14}$$

where N_t is the target thickness, ϕ is the incident fluence, and η is the Ge detector photopeak efficiency.

However, we must take a more complicated approach to the fusion cross sections.

$$\sigma_f(E) = \frac{Y_i}{N_t \ \phi \ \eta_i \ \beta_i} \tag{3.15}$$

The β_i's are the summing–branching correction factors. The subscript i represents any particular exit channel with its characteristic γ–ray, for which the yield was obtained. The β_i's are functions of the relative populations of excited states for the residual nuclei of interest. The populations, in turn, are related to the reaction mechanism, the dynamics of the parent cascade, and the structure of the cascade γ–decay of the residual nucleus. Also the β_i's depend on the incident beam energy and the detection geometry. The quantity $\eta\beta$ is the probability that a residual nucleus in a given distribution of excited states formed in an $^{18}O + {}^{18}O$ reaction will produce a count in the full energy peak of a specified γ–transition.

The calculations of the populations of excited states and ground states for every residual nucleus were performed with a Hauser–Feshbach statistical model.

The computer code HAUSER*5, used in our calculations, was written by Frederick M.Mann and revised slightly by others at Caltech. Since the statistical model is quite involved, the technical details are gathered together in the next chapter. To illustrate what the β–values mean: assume an evaporation residue with two excited states , $E_2 > E_1 > E_0$. Once the populations of the states P_2, P_1, P_0 with $P_2 + P_1 + P_0 = 1$ are calculated, the numbers of counts in the photopeaks at E_1 and E_2 will be

$$Y_1 = N\ \eta_1\{P_1 + P_2\ B\,(E_2 \rightarrow E_1)\,[1 - \epsilon_t\,(E_2 - E_1)]\} \tag{3.16}$$

and

$$Y_2 = N\ \eta_2\ P_2\ B\,(E_2 \rightarrow E_0) \tag{3.17}$$

where N is the production yield of the residual nucleus, η_1 and η_2 are the photopeak efficiencies for γ–rays at E_1, E_2 respectively. $\epsilon_t(E_2 - E_1)$ is the total detection efficiency for the γ–ray of energy $E_2 - E_1$. $B(E_2 \rightarrow E_1)$ *and* $B(E_2 \rightarrow E_0)$ are the branching ratios for the second excited state to the first excited state and to the ground state, respectively.

Thus we have the β–values for gamma rays with energy E_1, E_2

$$\beta_1 \ = \ \eta_1\{P_1 + P_2\ B\,(E_2 \rightarrow E_1)\,[1 - \epsilon_t\,(E_2 - E_1)]\} \tag{3.18}$$

and

$$\beta_2 \ = \ \eta_2\ P_2\ B\,(E_2 \rightarrow E_0) \tag{3.19}$$

respectively.

The production yield is

$$N \ = \ N_t \phi \sigma \tag{3.20}$$

Realistic summing–branching factors are much more complicated because they must be related to many discrete levels, (for example, over 26 levels are summed in the case of ^{30}Si). We have used the experimentally determined information for those bound states: energies, spins, parities and branching ratios. However the main task of establishing the summing–branching factors was to find the relative population probability of bound states as P_0 , P_1 , P_2, *etc.*, for all residual nuclei. We completed the calculations with the statistical model. The factors $\beta_i(E)$ as functions of incident beam energy are presented in the next chapter.

CHAPTER IV

The Statistical Model and Fusion Cross Sections

IV.A Hauser–Feshbach Theory

The compound nucleus statistical model (Ha 52), in contrast to a direct reaction model, is based on the two extreme hypotheses :

(1). Independence hypothesis. The two nuclei in the collision form a compound nucleus with high excitation energy. This energy is rapidly shared among the constituent nucleons of the compound nucleus until a statistical equilibrium energy distribution is reached. So the decay process of the compound nucleus will be independent of how the compound nucleus was formed. The formation and decay process of the compound nucleus at sub–barrier energy takes $\sim 10^{-18}$ sec, much longer than the transit time of one nucleus past another, $\sim 10^{-21}$ sec.

(2). Statistical hypothesis. Since the level density of the compound nucleus at such high excitation energy is very high, and the width of individual states is larger, in general, than their energy separation, the energy levels overlap each other strongly. Within the beam energy resolution there are so many states excited that a statistical description of the compound nuclear process is valid.

The two hypotheses and the reciprocity theorem are sufficient to derive the Hauser–Feshbach expression for the energy averaged fusion cross section. We will distinguish between (a) the total fusion cross sections, (b) two–body reactions (one particle and one residue in the exit channel), (c) three–body reactions (two particles and one residue in the exit channel), and (d) four–body reactions (three particles and one residue in the exit channel).

(a) The total fusion cross section $\sigma_f(E)$ is the cross section for formation of the compound nucleus.

$$\sigma_f(E) = \frac{\pi\hbar^2}{2\mu E}\sum_{l=0}^{\infty}(2l+1)\ T_l(E) \tag{4.1}$$

where μ is the reduced mass of the projectile and target nuclei.

E is the kinetic energy in the center–of–mass system.

$T_l(E)$ is the interaction barrier transmission probability of the incoming partial wave with angular momentum $\hbar l$. In the case of $^{18}O + {}^{18}O$ the l quantum number may take even numbers only because the projectile and target nuclei are identical spinless bosons.

(b) The cross sections for two–body reactions. The compound nuclei can decay to form various pairs of particles and fusion residues (here called exit channels, no matter which excited state the fusion residue may be in). For example,

$$^{18}O + {}^{18}O \longrightarrow {}^{36}S^* \longrightarrow \begin{cases} n + {}^{35}S^* \\ p + {}^{35}P^* \\ d + {}^{34}P^* \\ \alpha + {}^{32}Si^* \\ t + {}^{33}P^* \\ {}^{3}He + {}^{33}Si^* \\ \ldots\ldots\ldots \end{cases}$$

In general, if we label the initial channel as α and the exit channel as β, then the cross section for reaction leading from $\alpha \quad to \quad \beta$ is

$$\sigma_{\alpha\to\beta}(E) = \frac{\pi\hbar^2}{2\mu E_\alpha(2I_1+1)(2I_2+1)}\sum_{J^\pi}\frac{(2J+1)\sum_{l,s}[T_\alpha]^{J^\pi}_{l,s}\sum_{l',s'}[T_\beta]^{J^\pi}_{l',s'}}{T^{J^\pi}} \tag{4.2}$$

where $I_1 \ and \ I_2$ are the spins of projectile and target nuclei, and

$$T^{J^\pi} \equiv \sum_{\gamma,l,s}[T_\gamma]^{J^\pi}_{l,s} \tag{4.3}$$

In 4.2 and 4.3, the sums are carried out first over the orbital angular momentun l and parity π values that form a given J^π, then over all possible channels that could participate in the reaction as in (4.3), and finally over J and π. Usually, known properties of energy levels were used below 6 or 7 MeV. Beyond this, an integration must be done over a parameterized level density,

$$T^{J^\pi} = \sum_i T_i^{J^\pi} + \int T(E,J)\,\rho(E,J)\,dE \tag{4.4}$$

because detailed energy level information is not available. (The information on level density will be presented in the next section). The orbital angular momentum l and channel spin s are given values to conserve total angular momentum and parity:

$$\vec{J} = \vec{l} + \vec{s} = \vec{l}' + \vec{s}\,' \tag{4.5}$$

$$(-1)^\pi = (-1)^{l+\pi_0} = (-1)^{l'+\pi'} \tag{4.6}$$

where π_0 is the intrinsic parity of the incident channel,

π' is the intrinsic parity of the exit channel, and

π is the overall parity of the system.

This calculation gives the cross section to each accessible level of the residual nucleus. An unexpected example of a two–body reaction that was found in $^{18}O+^{18}O$ is the reaction

$$^{18}O + {}^{18}O \longrightarrow {}^{12}C + {}^{24}Ne \tag{4.7}$$

inferred from the detection of the decay of ^{24}Ne. However, all of the rest of the residual nuclei formed after one particle emission, such as ^{35}S, ^{35}P, and ^{32}Si are highly excited; they mostly prefer deexcitation by emitting particles rather than γ–rays, resulting in three–body reactions. (See Q–value scheme, fig.17).

(c) The cross sections for three–body reactions. The highly excited nuclei, in turn, are like compound nuclei. For example $^{35}S^*$ may have the exit channels,

$$^{35}S^* \longrightarrow \begin{cases} n + {}^{34}S \\ p + {}^{34}P \\ d + {}^{33}P \\ \alpha + {}^{31}Si \\ \ldots\ldots\ldots \end{cases} .$$

The residual nuclei can be populated in their excited states or ground states. Thus, the cross sections of three–body reactions are the cross sections of corresponding two body reactions times the decay probability.

$$\sigma_{\alpha\to\beta\to\gamma}(E_\alpha) = \sum_{J^\pi}(2J+1)\left\{ \frac{\pi\hbar^2}{2\mu E_\alpha (2I_1+1)(2I_2+1)} \sum_{l,s}[T_\alpha]^{J^\pi}_{l,s} \right\}$$

$$\times\left\{ \frac{\sum_{l',s'}[T_\beta]^{J^\pi}_{l',s'}}{T^{J^\pi}_{\alpha\to\beta}} \right\} \times \left\{ \frac{\sum_{l'',s''}[T_\gamma]^{J^\pi}_{l'',s''}}{T^{J^\pi}_{\beta\to\gamma}} \right\} \qquad (4.8)$$

The values in the second large bracket represent the decay probabilities that the compound nucleus formed from the α–channel decays to the β–channel. Similarly the third large bracket describes the probability distribution for formation of the γ–channel after the emission of a second particle.

(d) . The cross sections for four–body reactions. This is the dominant case in the near barrier energy region for $^{18}O + {}^{18}O$ because the very high Q–value allows the compound nuclei to emit as many as three particles before reaching low–lying excited states, with relatively high probability. For example, the dominant fraction of the ^{34}S nuclei, formed after two neutron emission from the compound nucleus

^{36}S, was populated in excited states with energy higher than the threshholds for neutron, proton and alpha–particles.

$$^{34}S^{*} \longrightarrow \begin{cases} n + {}^{33}S \\ p + {}^{33}P \\ \alpha + {}^{30}Si \\ \ldots\ldots\ldots\ldots \end{cases}$$

The expression for the four–body cross section is, in principle, the cross section for a three–body reaction, $\sigma_{\alpha\to\beta\to\gamma}(E_\alpha)$, multiplied by the probability that the residue in the γ–channel may decay to the δ–channel by one more particle emission. Practically, we calculated this in three steps. First, we calculated the population distribution as a function of excitation energy of the residual nuclei formed after the first particle emission from the compound nucleus (this is the two–body problem). Second, we calculated the decay probability from this residue to each desired discrete level of the next nucleus of interest (this is the three–body problem). Then we integrate the population distribution times the decay probability of this nucleus to obtain the cross sections in which we are interested (the four–body problem). To illustrate the detailed process of calculation for a four body–reaction, we take the calculation of the cross section to form ^{30}Si in the $^{18}O + {}^{18}O$ fusion reactions as an example. Suppose we need the cross section for the 2236 keV state of the residue ^{30}Si in the decay chain:

$$^{36}S^{*} \xrightarrow{n} {}^{35}S^{*} \xrightarrow{n} {}^{34}S^{*} \xrightarrow{\alpha} {}^{30}Si \qquad (4.9a)$$

First, we calculated the population distribution of ^{35}S excited states. This is a two–body problem. Similar to the derivation of equation (4.2), we have

$$P(E_x)\,dE_x \;=\; K\sum_{J^\pi}(2J+1)\sum_{l_n,s,J_x}[T_l]^{J^\pi}_{l_n,s}\rho(E_x,J_x)\,dE_x \qquad (4.10)$$

where K is a normalization constant, independent of E_x, $P(E_x)dE_x$ is the probability of ^{35}S being populated in the levels with excitation energy E_x *to* $E_x + dE_x$, J and π are the spin and parity of $^{36}S^*$ (the compound nucleus J and π are even for $^{18}O + ^{18}O$), J_x is the spin of $^{35}S^*$, $\rho(E_x, J_x)$ is the level density of $^{35}S^*$, E_n is the neutron kinetic energy in the c.m system needed below, $S_n = \frac{1}{2}$ is the spin of the neutron, l_n is the relative orbital angular momentum of n + $^{35}S^*$, and S is the channel spin of $n + ^{35}S^*$.

$$\vec{J} = \vec{l} + \vec{S}$$

$$\vec{S} = \vec{S}_n + \vec{J}_x$$

However, the code Hauser*5 limits all orbital angular momentum to $l \leq 10$. Thus we have for the compound nucleus:

$$J = 0, 2, 4, 6, 8, 10$$

$$l_n = 0, 1, 2, 3, 4, 5, 6, 7, 8, 9, 10 \quad and$$

$$S = |J - l_n| \ , \ |J - l_n + 1|, ...|J + l_n|$$

$$J_x = |S - \frac{1}{2}| \ , \ |S + \frac{1}{2}|$$

Fig.18 shows the diagram of the decay chain, and the relation of the beam kinetic energy $E_{c.m}$, the Q–value of $^{18}O + ^{18}O$, the neutron binding energy in the compound nucleus, B_n, and the excitation energy of ^{35}S, E_x.

$$Q + E_{c.m} = E_n + B_n + E_x \tag{4.11}$$

Hauser*5 provides the transmision coefficients $T_l(E_n)$ for all possible exit channels as functions of emitted neutron energy. Also we can calculate the total cross section

for formation of ^{35}S, in all excited states, $\sigma^*(E_{c.m})$. Thus, we have the cross section for ^{35}S excited states per unit energy:

$$\frac{d\sigma\left(E_x; E_{c.m}\right)}{dE_x} = \sigma^*\left(E_{c.m}\right) \frac{P\left(E_x\right)}{\int P\left(E'_x\right) dE'_x} \tag{4.12}$$

Additional results from the calculation are the corresponding neutron production cross sections at neutron energy E_n, where E_n is related to E_x by (4.11).

$$\Phi_n\left(E_n; E_{c.m}\right) = \frac{d\sigma\left(Q + E_{c.m} - E_n - B_n; E_{c.m}\right)}{dE_x} \tag{4.13}$$

Now we turn to the calculation of the decay probability, for every excited state of $^{35}S^*$ to the desired discrete states of the final nuclei, for example, the 2236 keV level of ^{30}Si. This is treated as a two–step evaporation process; the decay probability of $^{35}S^*$ to ^{30}Si involves two factors like the last two terms in expression (4.8). Because of the way the Hauser*5 code is written, we first suppose that we form $^{35}S^*$ at E_x [the same E_x as in expressions (4.10) and (4.11)] by the fusion reaction $n + {}^{34}S$. Then we assume that the $^{35}S^*$ decays by emitting one neutron and one alpha particle successively, to reach the 2236 keV state of ^{30}Si. Following the same steps as for the three–body calculation (4.8), we obtain the total fusion cross sections for $n + {}^{34}S$, $\sigma_t(E_x)$, and the cross section for formation of the ^{30}Si 2236 keV level, $\sigma_{2236}(E_x)$. Then, the probability that the E_x state of the nucleus $^{35}S^*$ decays to the ^{30}Si 2236 keV state is

$$P_{2236}\left(E_x\right) = \frac{\sigma_{2236}\left(E_x\right)}{\sigma_t\left(E_x\right)} \tag{4.14}$$

From (4.12) and (4.14) we then have the cross section for forming the ^{30}Si 2236 keV level by the decay mode (4.9a), at an incident energy $E_{c.m}$, in the $^{18}O + {}^{18}O$ reaction:

$$\sigma^a_{2236}\left(E_{c.m}\right) = \int \frac{d\sigma\left(E_x; E_{c.m}\right)}{dE_x} P_{2236}\left(E_x\right)\, dE_x \tag{4.15}$$

Besides the path (4.9a) leading to the fusion residue ^{30}Si, there are other paths:

$$^{36}S^{*} \xrightarrow{n} {}^{35}S^{*} \xrightarrow{\alpha} {}^{31}Si^{*} \xrightarrow{n} {}^{30}Si \tag{4.9b}$$

$$^{36}S^{*} \xrightarrow{\alpha} {}^{32}Si^{*} \xrightarrow{n} {}^{31}Si^{*} \xrightarrow{n} {}^{30}Si \tag{4.9c}$$

We calculated these partial cross sections for ^{30}Si production and then summed them to form an excitation function for ^{30}Si in the 2236 keV excited state.

$$\sigma_{2236} = \sigma^{a}_{2236} + \sigma^{b}_{2236} + \sigma^{c}_{2236} \tag{4.16}$$

Following the same method as for ^{30}Si, we calculated other four–body reaction cross sections, where the first emitted particle may be a neutron, proton or α. In the calculations for four–body reactions we ignored the deuteron as the first emitted particle, since its production probability is very small compared with that of a neutron and proton pair. This was verified both by our calculations and by experiment elsewhere, where the yield of deuterons was proved to be only about 1.5 % of the p–n pair yield. (Ga 86).

The partial cross sections and excitation function for $^{30}Si + 2n + \alpha$, $^{33}P + 2n + p$, $^{33}S + 3n$, $^{27}Mg + 2\alpha n$ and $^{24}Ne + 3\alpha$ .... are shown in fig.19. The neutron spectra, as well as proton, deuteron and alpha spectra (the production cross sections of n, p, d and α) as functions of $E_{c.m}$ are displayed in fig.20. The neutron spectra are roughly similar to evaporation spectra

$$\Phi_{n}(E_{n}) \sim \sqrt{E_{n}} e^{-E_{n}/T} \tag{4.17}$$

with nuclear temperature $T \approx$ 2.8 MeV (derived from the most probable energy).

The average neutron energy $\overline{E}_n$ increases slightly with incident energy $E_{c.m}$. So do the average energies of proton, deuteron and alpha–particles.

As $E_{c.m}$ increases from 7.0 MeV to 13.0 MeV,

$$\overline{E}_n = 3.7\ MeV\ to\ 4.0\ MeV$$

$$\overline{E}_p = 5.5\ MeV\ to\ 5.9\ MeV$$

$$\overline{E}_d = 4.8\ MeV\ to\ 5.4\ MeV$$

$$\overline{E}_\alpha = 7.7\ MeV\ to\ 8.0\ MeV$$

in the c.m system.

Obviously the Coulomb barrier inhibits the emission of charged particles, which need more kinetic energy to overcome the barrier. That is why the double charged particles, α, have the largest average energy, while neutrons have the smallest kinetic energy. The difference between $\overline{E}_p$ and $\overline{E}_d$ comes from the factor that the centrifugal potential for the deuteron is only half that of the proton for the same l–value.

IV.B Level Density and Optical Potential

For simplification of the calculation, one dimensional interaction between the projectile and target nuclei was assumed. In this model, the nuclei, taken as spheres with radii R_1 and R_2, are assumed to be in their ground states. The interactions depend only on the distance between the two centers. The transmission coefficients T_l in (4.1) were obtained by specifying the nuclear potential $V_N(r)$ and the Coulomb

potential $V_C(r)$, and integrating the one–dimensional partial wave Schrödinger equation outwards from the origin :

$$\left[-\frac{\hbar^2}{2\mu}\frac{d^2}{dr^2} + \frac{\hbar^2 l(l+1)}{2\mu r^2} + V_N(r) + V_C(r) - E\right]\psi_l \;=\; 0 \tag{4.18}$$

where μ is the reduced mass of the projectile and target nuclei, E is the kinetic energy, ψ_l is the radial part of the wave function with orbital angular momentum l. The second term in the bracket is called the centrifugal potential V_{centr} , and assigned as a part of the potential

$$V_l(r) \;=\; V_N(r) + V_C(r) + V_{centr}(r) \tag{4.19}$$

in the one dimensional equation

$$\left[-\frac{\hbar^2}{2\mu}\frac{d^2}{dr^2} + V_l(r) - E\right]\psi_l \;=\; 0 \tag{4.20}$$

The integration extends to a radius, beyond which the nuclear potential has no effect on the wave functions. This distance is usually less than the classical distance of closest appoach. There the solutions were matched to radial Coulomb wavefunctions to give complex phase shifts δ_l, which correspond to the S–matrix

$$S_l = e^{2i\delta} \tag{4.21}$$

Thus the transmission coefficients are

$$T_l \;=\; 1 - |S_l|^2 \;=\; 1 - \left|e^{2i\delta_l}\right|^2 \tag{4.22}$$

In cases where the transmission coefficients are small, $T_l \ll 10^{-4}$, they can profitably be computed directly from the wave function and the imaginary part of the optical potential :

$$T_l \;=\; \int |\psi_l|^2 \, W(r) \; d^3r \tag{4.23}$$

The Coulomb interaction of the two ions was supposed to be of the form of the potential between two uniformly charged spheres with $R_0 = R_1 + R_2$,

$$V_C(r) = \begin{cases} \frac{q_1 q_2 e^2}{r} & \text{if } r \geq R_0 \ ; \\ \frac{q_1 q_2 e^2}{2R_0}\left(3 - \frac{r^2}{R_0^2}\right) & \text{if } r \leq R_0 \end{cases} \tag{4.24}$$

The choice of nuclear potential is guided by the following principles. The potential should be sound on physical grounds and describe reasonably well both the low-energy fusion reaction and the elastic scattering, as well as agreeing with experimental properties of the nuclei as determined by nucleon or electron scattering. One of such nuclear potentials is the Woods–Saxon form for the optical potential.

$$V_N(r) = -V\ f(r; R_r, a_r) - iW_v\ f(r; R_v, a_v) + 4ia_s W_s \frac{d}{dr} f(r; R_s, a_s) \tag{4.25}$$

where $f(r; R_i, a_i) = [1 + exp(r - R_i)/a_i)]^{-1}$.

The radii $R_i = r_i A^{1/3}$, where i=r,v,s, and the $a_i's$ are the diffusenesses. V, W_v , and W_s are the energy–dependent depths of the real part, imaginary volume part, and imaginary surface part of the optical potential, respectively. All the depths were, in general, given large values so they were not very sensitive in the calculation of cross sections, while the geometry parameters of the optical potential were adjustable. There were altogether 6 geometry parameters for each kind of particle emission ($R_i's, a_i's$), which were adjusted to fit experimental data. They were given different values for different pairs of particles and fusion residues. But the parameters we should pay special attention to are those for the $^{18}O + {}^{18}O$ interaction potential, since they define the total fusion reaction cross section. The choice of optical potentials for the various pairs of particle and residue affects the relative

cross sections for the different exit channels. Our choice of the $^{18}O + ^{18}O$ parameters is that which was used to fit the differential cross sections of $^{18}O + ^{18}O$ elastic scattering by D.Kalinsky et al (Ka 77). It was found that either in the statistical model calculation or in an optical model calculation, this set of parameters was successful in reproducing the experimental total fusion cross section of the $^{18}O + ^{18}O$ reaction. All of the parameters concerning the potential depths and geometry are listed in table 6 (see ref. Wi 64, Be 69, Pe 74, Mc 66 and Ka 77).

Besides the optical potential, the partial fusion cross sections are sensitive to the level densities of the residual nuclei and the intermediate nuclei (such as $^{35}S, ^{35}P$ *and* ^{32}Si). The latter were not significant final products of the decay of the compound nucleus, because they were so highly excited that they continue the decay process by successively emitting particles until low–lying states are reached. However these nuclei are directly related to the probability distribution of the various exit channels after the first step emission. The importance of level density can be seen from equations (4.2) and (4.8), where the decay probabilities are proportional to the sums or integrals of transmission coefficients over all possible levels.

The adopted form of the level density, $\rho(E, J)$, was that defined by Gilbert and Cameron (Gi 65). The parameters in this formula were fitted to the known bound states. It was found that above the highest discrete level, E_c, which has been studied in details, the nuclei may approximately be assigned a constant nuclear temperature. Correspondingly, the level density is of the form :

$$\rho(E) = \frac{1}{T_c} exp[\frac{E - E_0}{T_c}] \tag{4.26}$$

where T_c is the nuclear temperature. The two parameters T_c and E_0 were adjusted to fit as well as possible the observed cumulative number of discrete levels up to energy E,

$$N(E) = exp[\frac{E - E_0}{T_c}] \tag{4.27}$$

This formula is valid for energies below a defined energy, $U' = 2.5 + 150/A$. At energies $E > U'$, this distribution was joined smoothly to a back–shifted Fermi gas formula (Ch 77a):

$$\rho(U) = \frac{\sqrt{\pi}}{12} \frac{exp\left(2\sqrt{aU}\right)}{a^{\frac{1}{4}} U^{\frac{5}{4}}} \frac{1}{\sqrt{2\pi}\sigma} \tag{4.28}$$

where $U = E - \Delta$ and Δ is the correction for pairing and shell effects. σ is related to the moment of inertia $\Im$ for spherical nuclei,

$$\Im = \frac{2}{5}\, m\, R^2 \,, \qquad R = 1.04 A^{\frac{1}{3}} \tag{4.29}$$

In (4.28), σ is given by

$$\sigma^2 = \frac{\Im}{\hbar^2}\sqrt{\frac{U}{a}} = 0.0104 A^{\frac{5}{3}}\sqrt{\frac{U}{a}} \tag{4.30}$$

The spin dependence of the energy level distribution was assumed to be Gaussian and the two different parity levels were supposed to have equal level densities. Thus the level density as a function of excitation energy, spin and parity was assumed to be of the form :

$$\rho(E, J^\pi) = \rho(U)\,\rho'(J) = \rho(U)\,\frac{(2J+1)}{2\sigma^2} exp\left(\frac{-J(J+1)}{2\sigma^2}\right) \tag{4.31}$$

In the work of Christensen and Switkowski(Ch 77a), the parameters a and Δ for all nuclei were given as functions of their mass A and T_c, the nuclear temperature determined from fitting the accumulated number of observed low–lying levels.

Unfortunately, the level densities obtained with those parameters did not produce reasonable partial cross sections in the present work. The ' a ' parameters for ^{32}Si and ^{28}Mg obtained in the manner described above were somehow higher than those for other nuclei involved in $^{18}O + {}^{18}O$ reactions. As a result, the partial cross section for the production of ^{28}Mg, calculated from the Hauser–Feshbach model, was as high as 80 percent of the total fusion cross section in our experimental energy region. These unphysical results come from the fact that the level density in the high excitation energy region was derived solely from the available information on a few low–lying levels. Sometimes the extrapolation procedure works fine. However, since there is only a rather small number of levels known in the low energy region, they do not necessarily provide a good statistical basis for extrapolation to higher excitation energy. The behavior of nuclei at higher energies could thus be very different from that inferred from the low energy region. There is the possibility that some nuclei could have higher level density at low excitation energy than others but a lower level density at high excitation energy.

We adopted another method, proposed by J.Holmes (Ho 76), to obtain the level density at high excitation energies. In order to achieve a systematic description of level density among nuclei a vast amount of level density information for more than 200 nuclei was investigated by Holmes, covering information on bound states and resonances from experimental approaches such as α, β and γ decay spectra, cross sections from (α, α') (p,p') (n,n') and (n,γ) reactions. A Fermi gas model with an equidistant level spacing assumption was used to predict the general trend of the level density for different nuclei. In performing this parameterization of level density, the levels unobserved due to actual overlap of levels or to the limitations of experimental resolution were treated statistically and corrected for.

The parameterization process was performed by formulating the level density with several parameters, which are assumed to be common to all nuclei, and determined by fitting the experimental data for all nuclei. Thus this process creates a consistency which relates the level densities of different nuclei in a systematic way. In the process, the nuclei were characterized according to their mass, atomic number and even–odd property. The level density was formulated as a function of mass, shell structure and even–odd property.

The level density for nuclei in our range of interest ($Z \leq 30$) can be described with two parameters a_i *and* Δ_i, The subscript i is used to specify different nuclei.

$$\Delta_i = \left(\frac{P_i - 80}{A_i}\right) MeV \quad and \tag{4.32}$$

$$a_i = (q_1 + q_2 S_i)^{q_3} MeV^{-1} \tag{4.33}$$

where q_1, q_2, q_3 are parameters, A_i is the mass of the nucleus, S_i is a shell structure correction and P_i is the total pairing energy, the sum of the neutron pairing energy $P_i(n)$ and the proton pairing energy $P_i(p)$.

$$P_i = P_i(n) + P_i(p) \tag{4.34}$$

The pairing energy and shell correction are listed in table 4.

The parameters q_1 , q_2 , q_3 are defined by the even–odd property of nuclei. For nuclei with atomic number $Z \leq 30$ the values of q_1 , q_2 , q_3 are :

nuclei	q_1	q_2	q_3
odd–odd	.05264±.00054	.001593±.000362	1.2
even–even	.05264±.00051	.001901±.000288	1.2
odd–even	.05262±.00042	.002210±.000187	1.2

We are, in fact, forced to use this approach to obtain the level density. Some of the neutron–rich nuclei involved in the present study, such as ^{35}P, ^{33}Si and ^{34}P, have either not been investigated at all, or only very little information about their bound states has been reported. One can therefore not extract level densities for these nuclei if one works in the way suggested by Christensen. We applied the formulae (4.28), (4.30) and (4.31) with the parameters from J.Holmeswork and obtained the level density for these nuclei and all of the other nuclei participating in the $^{18}O + ^{18}O$ reactions.

With the level densities and the optical potentials, obtained as discussed in this section, the code Hauser*5 was then used to calculate the total fusion cross section and partial cross sections. We have used these parameters within several different model analyses, and the calculated cross sections are generally in good agreement with our experimental data. This confirms that our choice of optical potential and level densities are, at least, reasonable.

This calculation also provided the cross sections for any bound states of the nuclei of interest. As discussed in chapter III, we treated these cross sections as relative population probabilities for each individual fusion residue. Then the summing and branching factors were calculated from the relative population probability, the tabulated branching ratios(En 78) and the calculated total detection efficiency, as demonstrated in the formulae (3.18) and (3.19). Then the calculated summing and branching factors were used to obtain the partial fusion cross sections. In fig.21, some of the summing and branching factors of interest are plotted as functions of the incident energy $E_{c.m}$.

IV.C Fusion Cross Sections

The calculated total and partial fusion cross sections for most of the exit channels are plotted in fig.19. All experimental cross sections (total reaction, total and partial fusions, inelastic scattering and neutron transfer) are listed in table 5. The energies in the table are effective energies as described in section IV.A. The systematic error for the total fusion cross section is estimated as 18%. In table 5, the statistical errors for the total fusion cross section are listed in same column with the cross section. The numbers in table 5 are plotted in fig.22.

Since the γ–ray identification for each exit channel and the formulae to obtain the partial fusion cross sections have been discussed in chapter II, only a few comments are noted here:

(1). The total fusion cross section is significantly higher than those for other oxygen isotope fusion reactions. For example, at $E_{c.m}$=12.0 MeV,

For $^{16}O + ^{16}O$ σ_f=356 mb.

For $^{16}O + ^{17}O$ σ_f=380 mb.

For $^{16}O + ^{18}O$ σ_f=355 mb.

For $^{18}O + ^{18}O$ σ_f=685 mb.

The data for $^{16}O + ^{16}O$, $^{16}O + ^{17}O$ and $^{16}O + ^{18}O$ are from J. Thomas (Th 87). It should perhaps be noted that the cross sections reported for the first three cross sections have been normalized to approximately equal above 12 MeV (c.m energies). We will derive the $^{18}O + ^{18}O$ potential with the inversion procedure in section V.B, and then explain in section V.E why the $^{18}O + ^{18}O$ fusion cross section is higher than the others.

(2). As expected, the neutron channels are dominant. About 2.2 neutrons were produced per $^{18}O + ^{18}O$ fusion over the entire energy region of the experiment. The

proton and alpha particle emisions are one order of magnitude smaller, while the rate of deuteron production is only about 1.5% of the total reaction rate.

(3). Four–body reactions dominate the $^{18}O + {}^{18}O$ reactions. The sum of the cross sections for the three exit channels $^{33}S + 3n$, $^{33}P + 2np$ and $^{30}Si + 2n\alpha$ constitute about 76% of the total reaction cross section. Another observed four–body reaction channel is $^{27}Mg + n2\alpha$, which is about 0.5% of the total cross section.

All three–body reactions, $^{34}S + 2n$, $^{34}P + np$, $^{28}Mg + 2\alpha$ and $^{31}Si + n\alpha$ together constitute only about 11% in the total reaction probability.

No two–body (only a single particle emission was) observed.

(4). A five–body reaction, $^{29}Si + 3n\alpha$ was observed. The probability for production of ^{29}Si is about 8% of the total. This may be the only case of 4 successive particle emissions among all low energy light nuclear reactions. This occurs because of the fact that in the $^{18}O + {}^{18}O$ reaction both the projectile and the target nuclei are neutron–rich nuclei and they have a high Q–value in forming the compound nucleus (Q=29.1 MeV).

(5). The calculated total fusion cross sections from the Hauser–Feshbach model are in quite good agreement with the experimental data. The calculated partial cross sections for the three main 4–body reactions also agree with experiment. The predicted cross section for the production of ^{34}S, however, is very small compared with the experimental data. This may be because only a limited number (25) of discrete levels of ^{34}S were summed in the theoretical calculation, while ^{34}S is a highly excited nucleus in the $^{18}O + {}^{18}O$ fusion reaction and many more than 25 levels of ^{34}S could undergo cascade γ–decay.

The production of ^{24}Ne is hard to explain within the framework of the compound nucleus model because it is energetically improbable to emit three α's to

form ^{24}Ne. A similar problem exists with the production of ^{22}Ne. The two exit channels may result from single–step or two–step transfer reactions. We will give qualitative explanations in section V.D.

CHAPTER V

Discussion

V.A. IWBC Calculation

It is helpful to analyze the experimental data with model calculations, because they can provide further understanding of the mechanism responsible for each individual reaction and the relative cross sections of the reactions. One such model is the Hauser–Feshbach statistical model, discussed in the previous chapter. We have used this model to obtain the total and partial fusion cross sections, and also the summing–branching factors needed to reduce our data to cross sections. This model calculation is sensitive to the empirical parameters of the optical potential and to the assumed level densities. In turn, the agreement obtained between the experimental cross sections and the theoretical predictions verifies the essential ideas of the model and the choice of parameters used in the theory.

The Incoming Wave Boundary Condition (IWBC) model is based on rather different ideas, (depends on fewer parameters of potential), and does not aim to produce the detailed predictions of the statistical model. The model requires two assumptions:

(1) The total cross section is divided into two parts: direct reactions and compound reactions. Since the direct inelastic scattering and transfer reaction are much smaller than the elastic scattering over our range of energy, the amplitude for elastic scattering is taken as the amplitude for all direct reactions. Thus to good approximation, the complete scattering wave function can, in general, be considered as the sum of elastic and compound contributions:

$$\Psi = \Psi_0 + \Psi_f \tag{5.1}$$

where Ψ is the total scattering wave function, Ψ_0 is the elastic scattering wave function and Ψ_f is the compound nuclear wave function.

(2) Since there is a strong nuclear absorption inside nuclei, it is natural to assume an IWBC radius, R_d, inside the barrier, such that for $r < R_d$, we have only incoming waves (entirely compound nuclear formation), while for $r > R_d$, we have both incoming and outgoing waves. No flux is artificially removed according to this model, because the interaction potential is real and the Hamiltonian is Hermitian. Thus unitarity is valid.

The radius R_d is defined in a region inside the barrier so that in the vicinity of R_d the WKB condition

$$2\pi \frac{d\frac{1}{K_l(r)}}{dr} \ll 1 \tag{5.2}$$

valid in the one dimensional equation

$$\frac{d^2\psi_l}{dr^2} + K_l^2(r)\ \psi_l = 0 \tag{5.3}$$

where

$$K_l(r) = \sqrt{\frac{2\mu}{\hbar^2}\left(E - V_N - V_C - \frac{l(l+1)\hbar^2}{2\mu r^2}\right)} \tag{5.4}$$

In the early work of Rawischer (Ra 66) the left side of eq.(5.2) was given the value 0.4. This is small enough to make the solution stable against small changes of R_d. Inside of R_d, ψ_l is an ingoing wave only, thus the WKB approximation solution is:

$$\psi_l(r) = \frac{A}{\sqrt{K_l(r)}} exp\{-i\int_{R_d}^{r} K_l(r)\ dr\} \tag{5.5}$$

where A is a constant to match the 'external' wave function outside R_d. The external wave function has the asymptotic form:

$$\psi_l(r) \sim u_l^{(-)}(kr) - S_l u_l^{(+)}(kr) \tag{5.6}$$

where $u_l^{(-)}(kr) = F_l(kr) + iG_l(kr)$ and $u_l^{(+)}(kr) = F_l(kr) - iG_l(kr)$ are the incoming and outgoing spherical Coulomb wave functions respectively. $F_l(kr)$ and $G_l(kr)$ are the regular and irregular Coulomb functions. By integrating (5.3) numerically outside R_d and matching it to its asymptotic form (5.6) at large R (just outside the range of nuclear interaction), one can obtain S_l:

$$S_l = \frac{\psi_l(R)\left[F_l'(kR) + iG'(kR)\right] - \psi_l'(R)\left[F_l(kR) + iG_l(kR)\right]}{\psi_l'(R)\left[F_l(kR) - iG(kR)\right] - \psi_l(R)\left[F_l'(kR) + iG_l'(kR)\right]} \tag{5.7}$$

Because of the strong Coulomb interaction it is convenient to separate the contribution from Rutherford scattering by writting

$$S_l = S_{l,N} e^{2i\sigma_l} \tag{5.8}$$

where

$$e^{2i\sigma_l} = \frac{\Gamma(l+1+i\eta)}{\Gamma(l+1-i\eta)} \tag{5.9}$$

Then the scattering amplitude in a partial wave representation is

$$f(\theta) \;=\; f_N(\theta) + f_C(\theta) \tag{5.10}$$

where the nuclear amplitude is

$$f_N(\theta) \;=\; \frac{1}{2ik}\sum_l (2l+1)\, e^{2i\sigma_l}\,(S_{l,N}-1)\, P_l(\cos\theta) \tag{5.11}$$

and the Rutherford amplitude is

$$f(\theta) \;=\; -\frac{\eta}{2k}\frac{exp\left(-i\eta\ln\left(\sin^2\theta/2\right) + 2i\sigma_0\right)}{\sin^2\theta/2} \tag{5.12}$$

For collision of **identical spinless bosons**, the amplitude is $f(\theta) + f(\pi - \theta)$. Then

$$f_N(\theta) \;=\; \frac{1}{ik}\sum_{l=even} (2l+1)\, e^{2i\sigma_l}\,(S_{l,N}-1)\, P_l(\cos\theta) \tag{5.13}$$

$$f_C(\theta) = -\frac{\eta}{2k}\{\frac{exp\left(-i\eta\ln\left(\sin^2\theta/2\right)+2i\sigma_0\right)}{\sin^2\theta/2}+\frac{exp\left(-i\eta\ln\left(\cos^2\theta/2\right)+2i\sigma_0\right)}{\cos^2\theta/2}\} \tag{5.14}$$

The elastic scattering cross section is

$$\begin{aligned}\frac{d\sigma_{el}}{d\Omega} &= |f(\theta)|^2 \\ &= |f_N|^2+|f_C|^2+2\Re[f_N^*\ f_C]\end{aligned} \tag{5.15}$$

The total fusion cross section is defined as the integrated flux of particles passing through the spherical surface at the IWBC radius R_d per unit time,

$$W_f = -\int R_d^2 d\Omega\frac{i\hbar}{2\mu}\left(\Psi\frac{\partial}{\partial r}\Psi^*-\Psi^*\frac{\partial}{\partial r}\Psi\right) \tag{5.16}$$

divided by the incoming current density, $\hbar k/\mu$. where the Ψ has the form:

$$\Psi(\vec{r}) = \frac{1}{k\hbar}\sum_{l=even}(2l+1)\,i^{l+1}\psi_l(r)\,P_l(\cos\theta) \tag{5.17}$$

in the vicinity of R_d. If (5.5) and (5.17) are inserted into (5.16), the total fusion cross section is

$$\sigma_f = \frac{2\pi}{k^2}\sum_{l=even}(2l+1)\,T_l \tag{5.18}$$

where T_l is the transmission coefficient

$$T_l = \frac{K_l(R_d)}{K_l(R)}|\psi_l(R_d)|^2 \tag{5.19}$$

This is equivalent to (4.22) since unitarity requires

$$T_l = 1-|S_{l,N}|^2 \tag{5.20}$$

The nuclear potential $V_N(r)$ has been taken to have a Woods–Saxon form as in the statistical model calculation, but there is no imaginary part in the potential.

The depth of the potential V_r=-100 MeV and the diffuseness a_r=0.51 fm are those used in chapter IV to produce the total and partial fusion cross sections, while the barrier radius is increased. We define the Woods–Saxon radius R_r by defining the S–wave Coulomb barrier radius R_B, so that

$$barrier\ \ radius \qquad R_B \ = \ r_b \left(A_1^{1/3} + A_2^{1/3} \right) \tag{5.21}$$

where we choose r_b=1.76 fm in present work. Then

$$R_r \ = \ R_B - a_r ln \left(\kappa - 1 + \sqrt{\kappa^2 - 2\kappa} \right) \tag{5.22}$$

with

$$\kappa \ = \ \frac{R_B^2 V_0}{2 q_1 q_2 e^2 a_r} \tag{5.23}$$

The corresponding Coulomb barrier is

$$V_B \ \approx \frac{q_1 q_2 e^2}{R_B} \left(1 - \frac{a}{R_B} \right) \tag{5.24}$$

The height of the S–wave Coulomb barrier for $^{18}O + {}^{18}O$ is

$$V_B \ = \ 9.44\ MeV \qquad at \quad R_B \ = \ 9.225\ fm \tag{5.25}$$

which is slightly larger than that derived later from the BKN inversion procedure. The corresponding Woods–Saxon radius R_r is 6.63 fm. We found that the set of potential parameters provides reasonable fits to both the elastic scattering cross section and the total fusion cross section. The IWBC fusion cross section and the S–factor are plotted in fig.23 and fig.24 with the experiment data.

Several goups (Ka 75,77, Sh 70, and Va 74) have studied $^{18}O + {}^{18}O$ elastic scattering at energies near and above the Coulomb barrier. Kalinsky's experinental data are reproduced with a coupled–channel fit. In his calculation, the 0^+ ground

state and 2^+ excited state were coupled by both the electromagnetic and the nuclear interaction. The $^{18}O + {}^{18}O$ optical potential chosen for the coupled–channel calculation is the same as that listed in table 6. The resulting cross sections are displayed with the experimental data in fig.25 and fig.26. The curve of total elastic scattering cross section indicates a peak around 19 MeV (Lab system). This is believed to be caused by the rainbow effect.

V.B BKN Inversion

The inversion procedure, developed by Balantekin, Koonin and Negele (BKN), presents another framework for the analysis of subbarrier fusion cross sections and offers an opportunity to determine the one–dimensional effective potential directly from experimental data (Ba 83). This method describes the total fusion cross section through the partial wave penetrability, $T_l(E)$.

$$\sigma(E) = \frac{\pi\hbar^2}{2\mu E} \sum_{l=0}^{\infty} (2l+1)\, T_l(E) \tag{5.26}$$

The potential barrier, for all partial waves, is assumed to be of the form of an inverted parabola near the barrier radius R_B. The top of the parabola corresponds to the barrier height at the barrier radius, $V(R_B) = V_B$. The fusion reaction takes place while $r \leq R_B$. Thus the WKB approximation form of $T_l(E)$ in this situation is:

$$T_l(E) = \left(1 + e^{2S_l(E)}\right)^{-1} \tag{5.27}$$

where

$$S_l(E) = \int_{r_1}^{r_2} \sqrt{\frac{2\mu}{\hbar^2}[V(r) - E] + \frac{l(l+1)}{r^2}}\; dr, \tag{5.28}$$

for energy $E < V_B$, where r_1 and r_2 are the classical inner and outer turning points respectively.

The $T_l(E)$ for non–zero l is assumed to be approximately the $l = 0$ penetrability at a shifted energy, *i.e.*,

$$T_l(E) \approx T_0[E - \frac{l(l+1)\hbar^2}{2\mu R^2(E)}] \tag{5.29}$$

The sum over l is assumed to be replaced by an integral from 0 to ∞, thus

$$S_0(E) = \frac{1}{2} log\{[\frac{d}{dE}\left(\frac{E\sigma}{\pi R^2(E)}\right)]^{-1} - 1\} \tag{5.30}$$

The barrier height, V_B, is determined by requring $S_0(E = E_B) = 0$, since $r_1 = r_2$. Thus

$$\frac{d}{dE}[\frac{E\sigma}{\pi R^2(E)}]\Big|_{E=V_B} = \frac{1}{2} \tag{5.31}$$

The thickness of the barrier at energy $V < V_B$ is

$$t(V) = r_2(V) - r_1(V) = -\frac{2}{\pi}\sqrt{\frac{\hbar^2}{2\mu}}\int_V^{V_B} \frac{dS_0/dE}{\sqrt{E-V}}dE \tag{5.32}$$

Experience has shown that the derived thickness t is not particularly sensitive to the choice of $R(E)$, which is taken as the average value of the barrier radius and the Coulomb turning point:

$$R(E) = \frac{1}{2}[R_B + R_C(E)] = \frac{1}{2}[R_B + \frac{Z_1 Z_2 e^2}{E}] \tag{5.33}$$

R_B and r_2 are not directly derived from the experimental data. However they are related by the continuity of the potential at the top of the barrier. To determine R_B and r_2, a physical phenomenological nuclear potential V_N' (exponential) is assumed. Its strength and range are adjusted so that the sum of the nuclear potential and the two–point charge Coulomb potential reproduces the barrier height, V_B, determined

from (5.31). With the nuclear potential $V'_N(r)$ and the Coulomb potential, the outer turning point, r_2, is defined so that

$$V = V'_N(r_2) + \frac{Z_1 Z_2 e^2}{r_2} \tag{5.34}$$

Then the inner turning point is $r_1 = r_2 - t$

For input to the inversion procedure the $^{18}O + ^{18}O$ total fusion cross sections were assigned a systematic error of 18%. The statistical errors on the fusion data ranged from 4% for most of measured energy points to 35% for the measurement at the lowest energy. These errors were listed in table 5.

The input barrier radius, $R'_b = 8.6\ fm$, is the value for the S–wave optical potential, which was used in the Hauser–Feshbach model calculation. After 50 iterations during the inversion process, the final barrier radius and height obtained were

$$^{18}O + ^{18}O \quad R_B = 8.92\ fm, \qquad V_B = 9.26 \pm 0.12\ MeV$$

The shape of the $^{18}O + ^{18}O$ one–dimensional barrier is plotted in fig.27. In fig.28, all 4 barriers for the reactions of pairs of oxygen isotopes, are plotted together. The $^{16}O + ^{16}O$ reaction (Th 86) has the largest barrier height and the smallest barrier radius. In contrast, the $^{18}O + ^{18}O$ has the smallest barrier height and the largest barrier radius. The $^{16}O + ^{17}O$ potential has an obviously unphysical shape. At least some of the strong backbend could come from the fact that the $^{16}O + ^{17}O$ fusion cross section at low energy region may have been overestimated. It has been pointed out (Wu 86 and Th 87) that some of the apparent high yield of the $^{16}O + ^{17}O$ fusion cross section (Th 86) at low energies may have arisen from a misidentified γ–ray. Thus it is possible that the γ–ray peak identified as the 1017 keV γ–ray

from the channel $^{28}Al + p\alpha$ should have been attributed to the 1014 keV γ–ray from the channel $^{27}Al + d\alpha$, or perhaps from the $^{17}O + ^{12}C$ fusion channel (1014 keV from the channel $^{27}Al + np$). The summing and branching factors are such that this change in identification would reduce the fusion cross section derived for the $^{16}O + ^{17}O$ reaction. The lowest barrier height in $^{18}O + ^{18}O$ is linked to the largest fusion cross section among all the oxygen isotope reactions in the subbarrier energy region. To verify this we artificially decreased the total fusion cross section of $^{18}O + ^{18}O$ by 33.3%. The resulting false barrier has same barrier radius and general trend as that in $^{18}O + ^{18}O$, but the barrier height increases by 0.32 MeV. The barrier parameters obtained by the inversion procedure are as follows ($^{18}O + ^{18}O$, present work; others by J. Thomas).

$$^{16}O + ^{16}O \quad R_B = 8.24\ fm, \qquad V_B = 10.17 \pm 0.17\ MeV$$

$$^{16}O + ^{18}O \quad R_B = 8.48\ fm, \qquad V_B = 9.75\ MeV$$

$$^{18}O + ^{18}O \quad R_B = 8.92\ fm, \qquad V_B = 9.26 \pm 0.12 MeV$$

$$^{18}O + ^{18}O^{*} \quad R_B = 8.92\ fm, \qquad V_B = 9.58 \pm 0.16 MeV$$

The asterisk identifies the barrier parameters that were obtained by artificially cutting the cross section by 1/3. Fig.29 is plotted, for convenience, to look directly at the cross sections as a function of the energy below the barrier ($E_{c.m} - V_B$). The curves for $^{16}O + ^{16}O$, $^{16}O + ^{17}O$ and $^{16}O + ^{18}O$ are copied from ref.(Th 86), where the barrier heights were chosen according to the Akyuz and Winther model (Ak 80). It is worth noting that the inversion procedure is based on the assumption of one–dimensional barrier penetration. However, there are other degrees of freedom, such as deformation of the nuclei and the coupling to inelastic scattering, which

may enhance the total fusion cross sections. Such contributions to the total fusion cross section are not included here. Thus, the true barrier height of the $^{18}O + {}^{18}O$ reaction may be slightly higher than that derived in this section.

V.C Inelastic scattering

Among the curves for all of the $^{18}O + {}^{18}O$ excitation functions, the inelastic scattering cross section shows a quite different trend. It seems that the yield curve for $^{18}O + {}^{18}O$ inelastic scattering over the present energy region can be divided into three parts: Coulomb excitation in the low energy region, nuclear excitation in the high energy region, and interference between Coulomb interaction and nuclear interaction. (In fig.30, the regions are separated by two dotted lines). This phenomenon may be described in the first–order perturbation theory as follows:

The inelastic scattering amplitude for the transition from channel α to channel β (in the present case, the ^{18}O nucleus is excited from its 0^+ ground state to its first 2^+ state of energy 1982 keV) has the form:

$$f_{\beta\alpha} = \int d\mathbf{r}\ \chi_{\beta}^{(-)}(\mathbf{K}_{\beta},\mathbf{r})^{*}\left[V_{\beta\alpha}^{C}(\mathbf{r}) + V_{\beta\alpha}^{N}(\mathbf{r})\right]\chi_{\alpha}^{(+)}(\mathbf{K}_{\alpha},\mathbf{r}) \tag{5.35}$$

where $\chi^{(-)}$ and $\chi^{(+)}$ are the Coulomb distorted–wave functions, representing the relative motion of the projectile and target nuclei. $V_{\beta\alpha}^{C}$ and $V_{\beta\alpha}^{N}$ are the Coulomb and nuclear potentials as a function of separation $\mathbf{r}$. The inelastic scattering amplitude thus has two parts

$$f_{\beta\alpha} = f_{\beta\alpha}^{C} + f_{\beta\alpha}^{N} \tag{5.36}$$

and the cross section is

$$\frac{d\sigma_{\beta\alpha}}{d\Omega} = \left|f_{\beta\alpha}^{C} + f_{\beta\alpha}^{N}\right|^{2}\frac{K_{\beta}}{K_{\alpha}} \tag{5.37}$$

At low bombarding energies the Coulomb barrier inhibits the projectile entering the attractive nuclear field of the target nucleus. Thus only the tail of the nuclear potential at large separation can participate in the reaction, and this is smaller than the Coulomb interaction. Thus to first–order in the nuclear interaction, we have the approximation formula, for low sub–barrier energies,

$$\left|f_{\beta\alpha}\right|^2 \approx \left|f^C_{\beta\alpha}\right|^2 + 2Ref^{C*}_{\beta\alpha}f^N_{\beta\alpha} \tag{5.38}$$

The interference term is always negative because the nuclear interaction and the Coulomb interaction have opposite signs. In the present experiment the interference occurs in the energy region $8.7MeV < E_{c.m} < 9.7MeV$, *i.e*, near the top of the interaction barrier obtained from the BKN inversion model:

$$E_B - 0.5MeV < E_{c.m} < E_B + 0.5MeV, \qquad E_B = 9.26\ MeV. \tag{5.39}$$

The location of the transition from Coulomb excitation to nuclear excitation agrees with the assumption that the nuclear interaction would be smaller than the Coulomb interaction below the top of the barrier (see fig.27). Thus at sub–barrier energies, the Coulomb interaction dominates the inelastic scattering process. In the semi-classical approach, described by K.Alder *et al.* (Al 56), the Coulomb excitation is treated as the sum of its multipole components, and the cross section for such inelastic scattering is

$$\sigma = \sum_{\lambda=1}^{\infty} \sigma_{\lambda E} + \sigma_{\lambda M} \tag{5.40}$$

The cross section for an E2 transition, which takes the (target) ^{18}O nucleus from its 0^+ ground state to its first excited 2^+ state, is

$$\sigma_{E2} = \left(\frac{Z_1 e}{\hbar v_i}\right)^2 \frac{1}{a^2}\ B\left(E2\right) f_{E2}\left(\eta_i, \xi\right) \tag{5.41}$$

where Z_1 is the charge of the projectile nucleus, v_i is the initial relative velocity, a is half the distance of the closest approach in a head–on collision, and ξ is a dimensionless quantity related to the excitation energy ΔE:

$$a = \frac{Z_1 Z_2 e^2}{\mu v_i v_f}, \qquad \xi = \frac{Z_1 Z_2 e^2}{\hbar}\left(\frac{1}{v_f} - \frac{1}{v_i}\right), \qquad \eta_i = \frac{Z_1 Z_2 e^2}{\hbar v_i} \tag{5.42}$$

where v_f is the final relative velocity, $v_f = v_i\sqrt{(E - \Delta E)/E}$. $f_{E2}(\eta_i, \xi)$ is tabulated in Table II.5 of ref. (Al 56). $B(E2)$ represents the reduced E2 transition probability, associated with the reduced matrix element of the target nucleus:

$$B(E2) = \sum_{m_\beta, m'} \left| < I_\alpha m_\alpha | M(E2, m') | I_\beta m_\beta > \right|^2$$

$$= \frac{1}{2I_\alpha + 1} \left| < I_\alpha \| M(E2) \| I_\beta > \right|^2 \tag{5.43}$$

for the transition from spin state I_α to spin state I_β. The E2 matrix elements for the 0^+ and 2^+ states of ^{18}O were measured by A. M. Kleinfeld (Kl 75):

$$< I_\alpha \| M(E2) \| I_\beta > = \begin{pmatrix} 0 & 0.07106 \\ 0.07106 & -0.21 \end{pmatrix} e.b \qquad I_\alpha, I_\beta = 0, 2 \tag{5.44}$$

The calculated cross section for the $^{18}O + ^{18}O$ (Coulomb excitation) inelastic scattering is plotted in fig.30. The cross section shown has been obtained by multiplying the calculated target excitation cross section by two, to take account of the fact that there are two ^{18}O nuclei involved.

As the bombarding energy increases, the nuclear force can no longer be treated in perturbation theory. Strong attraction occurs between the target and projectile nuclei, and nuclear excitation competes strongly with Coulomb excitation in the inelastic scattering. It has been established by empirical analyses of the "grazing

collision" that the elastic scattering can be well represented by complex optical potentials whose imaginary parts simulate the effect of all the reaction channels. In distorted–wave Born approximation (DWBA) these potentials are used to generate distorted waves, which are then employed to obtain the form factors with the derivative of optical potentials. The DWUCK4 computer code, (Ku 87), calculates a transition amplitude for the reaction A(a,b)B, in general, of the form

$$T = J \int d\underline{r}_b \int d\underline{r}_a \Psi_f^{-*}(\underline{k}_f, \underline{r}_b) \langle b\ B \mid V \mid a\ A \rangle \Psi_i^{+}(\underline{k}_i, \underline{r}_a) \tag{5.45}$$

where Ψ_f and Ψ_i are the distorted waves, $\underline{r}_a$ and $\underline{r}_b$ are the relative coordinates for the system (a,A) and (b,B) respectively. J is the Jacobian of the transformation to these coordinates. The quantity $\langle\ b\ B \mid V \mid a\ A \rangle$ is called the form factor for the reaction and must contain a delta function for the coordinates $\underline{r}_a$ and $\underline{r}_b$. For inelastic excitation, the first–order perturbation theory (to the deformation of the target nucleus) is employed to produce collective model prescription of the form factor. The interaction term V is

$$V = -\beta_l \frac{R_0}{a} V_0 \frac{df}{x} Y_l^0(\theta) \tag{5.46}$$

The potentials in present case were taken to be of the Woods–Saxon form $V_0 f(x)$, where $f(x) = 1/(1+e^x)$ and $x = (r - R_1 - R_2)/a$. (the parameters of the potential is listed in the caption to fig.30). θ is the angle between the scattering particle and the nuclear symmetry axis. The optical potential used to compute the initial and final distorted waves has also been chosen to be the Woods–Saxon form, but its parameters were varied to fit the $^{18}O + {}^{18}O$ elastic scattering cross section. (same as that in table.6). The deformation parameter $\beta_2 = 0.16$ was chosen from R. Vandenbosch's work (Va 74). This is the value usually used to describe ^{18}O (Ka

77). The inelastic scattering cross section (nuclear excitation) is plotted as the solid curve in fig.30. As was the case at lower energies, the calculated cross section was doubled to take account of the two ^{18}O nuclei.

V.D Transfer Reactions

In addition to fusion reactions and inelastic scattering, three kinds of transfer reactions were also observed in our experiments. These reactions are:

$$^{18}O\ (\ ^{18}O, ^{17}O\ )\ ^{19}O, \text{ or } ^{17}O^*, \text{ or } ^{19}O^*$$

$$^{18}O\ (\ ^{18}O, ^{16}O\ )\ ^{20}O, \text{ or } ^{20}O^*,$$

$$^{18}O\ (\ ^{18}O, ^{14}C\ )\ ^{22}Ne, \text{ or } ^{22}Ne^*$$

1. The one–neutron transfer reaction was observed only at energies $E_{c.m} > 12MeV$.

2. The two–neutron transfer reaction was found to occur with significant reaction probability because of its favorable Q–value ($Q_0 = -0.628MeV$). One of the products in the reaction, ^{16}O, is populated in its ground state, while the other product, ^{20}O, may be populated in its 0^+ ground state or its first 2^+, 1674 keV state. The data for the measured cross sections are listed in table 5 and plotted in fig.22. (The theoretical curve shown has been obtained by doubling the calculated cross section to account for the two ^{18}O nuclei.)

D. Kalinsky and S. Kubono (Ka 77, and Ku 79) measured the angular distribution for $^{18}O + ^{18}O \rightarrow ^{16}O + ^{20}O$ at above–barrier energies. They analyzed their data in the DWBA framework, and assumed the two–neutron transfer to be a one–step process. Our data are well described by considering the one–step two–neutron transfer process in the DWBA framework. However, analysis of other $(^{18}O, ^{16}O)$

reactions indicates that both one–step and two–step two–neutron processes are frequently important. Generally, in the work, good agreement between experimental data and theoretical calculation has been obtained by summing the contributions from the two processes and including their interference. The wave function of the ^{18}O ground state is also important in the calculation. One of the suggested wave functions (As 85) is

$$| \, ^{18}O \; 0^+ > \approx \; 0.893 \, | \, (d^2_{5/2})_0 \; > \; + 0.354 \, | \, (2s^2_{1/2})_0 \; > \; + 0.275 \, | \, (d^2_{3/2})_0 > \quad (5.47)$$

3. The α–transfer from one ^{18}O to the other was evidenced by the 1274.5 keV and 2082.5 keV γ–rays. The latter corresponds to the transition from the 4^+ 3357 keV state of ^{22}Ne to its 2^+ 1274.5 keV state. It is a very tiny peak in the pulse–height spectra. The 1274.5 keV state is the ^{22}Ne first excited state, which decays to the ground state by γ–emission. In the pulse–height spectra, this γ–ray is overlapped by the Doppler broadened ^{29}Si 1273.3 keV γ–peak. The energy resolution of our detection system would not be good enough to separate them even if neither was Doppler broadened. However, we can roughly estimate the ^{22}Ne γ–ray contribution by comparing the shapes of the composite peak at different beam energies. Fig.31 shows the difference. We found that, as the beam energy goes down,the unshifted sharp peak becomes relatively more important. This is because the life–time of ^{22}Ne is 3.7 ps, while ^{29}Si has life–time of 0.28 ps (the stopping time of a residual nucleus in our experiment is about 1.0 ps). Thus the broad part of the composite peak comes from ^{29}Si only, and the sharp part of the peak may include contributions from both ^{29}Si and ^{22}Ne. We have assumed that the yield of the entire peak mainly comes from ^{29}Si at beam energies $E \geq 20$ MeV, and the 'extra' counts in the sharp part of the peak at low beam energies $E < 20$ MeV are

from ^{22}Ne. Thus we were able to obtain the contribution of the $^{22}Ne^*$ to the 1274 keV peak approximately, and to estimate the production cross section of $^{22}Ne^*$, for low beam energies only. The data are listed in table 5.

Although our experimental method could not be used to detect the production of the ground state of ^{22}Ne, the experimental results discussed above suggest the coexistence of both $\alpha + {}^{14}C$ and $2n + {}^{16}O$ clusters in the ^{18}O nucleus. Moreover, these cluster configurations may provide an explanation for the production of the nucleus ^{24}Ne in an $^{18}O + {}^{18}O$ reaction. It is hard to understand the production of the ^{24}Ne nucleus from fusion reactions such as

$$^{18}O\,(^{18}O, 3\alpha)\,^{24}Ne \qquad or \qquad ^{18}O\,(^{18}O, ^{12}C)\,^{24}Ne \tag{5.48}$$

The 3α channel seems unlikely due to its unfavorable Q–value (Q=–2.9 MeV) and the large kinetic energy that would be needed for three α–particles. The ^{12}C channel may not make a significant contribution because the statistical probability that enough energy in the compound nucleus ^{36}S would be concentrated on a cluster consisting of 6 neutrons and 6 protons is very small. The calculated cross sections for the two processes based on the Hauser–Feshbach model are plotted in fig.19; the cross sections for both the 3α channel and the ^{12}C channel are much smaller than the experimental cross section for ^{24}Ne production (fig.22).

A more likely explanation of the ^{24}Ne production comes from transfer reactions, illustrated by the following:

(two–step)

$$\begin{array}{ccccc} {}^{18}\mathrm{O} & \longrightarrow & {}^{16}\mathrm{O} & \longrightarrow & {}^{12}\mathrm{C} \\ & \downarrow 2n & & \downarrow \alpha & \\ {}^{18}\mathrm{O} & \longrightarrow & {}^{20}\mathrm{O} & \longrightarrow & {}^{24}\mathrm{Ne} \end{array} \qquad \begin{array}{ccccc} {}^{18}\mathrm{O} & \longrightarrow & {}^{14}\mathrm{C} & \longrightarrow & {}^{12}\mathrm{C} \\ & \downarrow \alpha & & \downarrow 2n & \\ {}^{18}\mathrm{O} & \longrightarrow & {}^{22}\mathrm{Ne} & \longrightarrow & {}^{24}\mathrm{Ne} \end{array}$$

or (one–step)

$$\begin{array}{ccc} {}^{18}\mathrm{O} & \longrightarrow & {}^{12}\mathrm{C} \\ & \downarrow {}^{6}He & \\ {}^{18}\mathrm{O} & \longrightarrow & {}^{24}\mathrm{Ne} \end{array} \qquad (5.49)$$

The ^{18}O cluster configuration $\alpha + ^{14}C$ has been demonstrated by many experiments. (see, for example, ref. (Ga 83), (Ra 84)). A low–lying $\alpha + {}^{14}C$ molecular band includes 0_2^+(3.65 MeV), 1^-(4.45 MeV), 2_3^+(5.26 MeV), 3_3^-(8.29 MeV) and 4_3^+(10.26 MeV); these levels are plotted in fig.6. The existence of a ^6He clustering in ^{18}O has been proposed previousely in a calculation of the elastic scattering angular distribution of $^{12}C + {}^{18}O$. (Ra 84).

Although the mechanism for the ^{24}Ne production remains unclear, the cross section for the two–neutron transfer reaction in $^{18}O + {}^{18}O$ is quantitatively reproduced with a zero–range DWBA approach. In the calculation, we take the same optical potential to produce the two distorted waves for the initial systems, $^{18}O+{}^{18}O$ and the final system, $^{16}O + {}^{20}O$. The neutron interaction with the ^{16}O core is also required; it was chosen to fit the 2–neutron transfer reaction. We found that the potential is close to the neutron potential defined by Wilmore and Hodgson (see table 6). These potentials are given in the caption to fig.32. The resulting two–neutron transfer reaction cross section is plotted in fig.32, which takes account of the fact that either ^{18}O nucleus may be the source of the transferred two–neutron pair by doubling the calculated value.

V.E Summary and Conclusion

We have presented our measurements of the fusion cross sections, transfer reaction cross sections, and inelastic excitation cross sections. We have also analyzed our total fusion cross section and elastic scattering cross section with the IWBC model. For completeness we have reproduced the experimental cross sections for inelastic scattering and two–neutron transfer reaction with DWBA model calculations. We found good agreement in most cases between the experimental data and model calculations. We determined the shape of the interaction barrier with the BKN inversion method and compared it with the interaction barriers derived for other oxygen isotopes.

At sub–barrier energies, a one–dimensional potential still provides a good explanation of the behavior of the $^{18}O + {}^{18}O$ reactions. The cross sections for $^{16}O + {}^{16}O$, $^{16}O + {}^{17}O$, $^{16}O + {}^{18}O$ and $^{18}O + {}^{18}O$ are plotted in fig.33. $^{18}O + {}^{18}O$ shows the largest cross sections of all. This can be understood as resulting from the fact that the ^{18}O nucleus has the largest radius and the largest diffuseness because of the two neutrons outside the ^{16}O core. In turn, the large nucleus radius and diffuseness reduce the Coulomb barrier and make quantum tunneling easier. In addition, simply increasing the number of nucleons in the colliding nuclei increases the density of states in the compound nucleus and the number of exit channels, and thus increases the cross sections for $^{18}O + {}^{18}O$ near and above the Coulomb barrier. Our IWBC fit to the elastic scattering data and the BKN inversion support the conclusion that the $^{18}O + {}^{18}O$ reactions have the largest cross sections. A similar effect has also been observed in reactions of the oxygen isotopes $^{16,17,18}O$ with ^{12}C and ^{27}Al (see (Ey 76) and (Ei 77)). Fig.34 and fig.35 show the increase of the reaction cross sections with an increase of the projectile mass as one goes from ^{16}O to

^{18}O. We plot the experimental cross sections of oxygen isotopes reactions in fig.33. The total fusion cross sections for $^{16}O+^{17}O$ and $^{16}O+^{18}O$, measured by J. Thomas (Th 86), were simply normalized to those of $^{16}O+^{16}O$ near $E_{c.m} = 12\ MeV$. An attempt should be made to obtain independent absolute normalizations for these reactions at a few energies. It would then be possible to compare the cross sections among the fusion reactions for various pairs of oxygen isotopes more meaningfully, to see how they vary as a function of the number of valence neutrons.

In addition to the one-dimensional barrier tunneling effect, the coupling of other intrinsic degrees of freedom, such as inelastic or transfer channels, may play some role in enhancing sub–barrier fusion reaction cross sections (La 85). The coupled–channel method may be used to relate fusion reactions to the excitation of projectile and/or target nuclei and to transfer reactions. This is in contrast to the simple compound nucleus model where the two nuclei that fuse are assumed to be structureless spheres. As we discussed in the previous section, the structure of the nucleus ^{18}O has additional degrees of freedom; it may become excited (inelastic scattering) or it may participate in transfer reactions. Because of the favorable Q–values for the 2–neutron transfer reaction (Q near 0) and for the α–transfer reaction (Q–value = 3.4 MeV), and the relatively small α binding energy (E_b^{α}=6.23 MeV) in ^{18}O, both the inelastic coupling and the transfer reaction coupling are expected to be significant in $^{18}O + ^{18}O$ sub–barrier reactions.

Several authers, for example, S. Landowne and M. Beckerman (Be 85 and La 85) give the details of the coupled–channel method. The starting point is the set of coupled Schrödinger equations:

$$[-\frac{\hbar^2}{2\mu}\frac{d^2}{dx^2} + V(x) - E]u_\alpha(x) = \sum_\beta < \alpha|H_0 + V^c|\beta > u_\beta \qquad (5.50)$$

where H_0 is the intrinsic Hamiltonian, $|\alpha>$, $|\beta>$ are eigenvectors of H_0 with $H_0|\beta> = E_\beta|\beta>$, and V^c is the coupling interaction. With an appropriate choice of coupling interaction V^c and coupled states $|\beta>$, one can reasonably well reproduce the enhancement of the fusion cross section by transfer reactions and inelastic excitation.

Furthermore, there is growing evidence that static and dynamic deformations of the projectile and/or target nuclei may be important in the low–energy regime in fusion reactions. Since the shape of a deformed nucleus is no longer spherical, the barrier is a function of the relative orientation of the projectile and the target nucleus. For statically deformed nuclei, the radius may be written as

$$R(\theta) = R_0\ [1\ +\ \sum \beta_{\lambda i}\ Y_\lambda^0(\theta)] \tag{5.51}$$

and the penetrability is written as an integral with weight function $W(R_1, R_2)$ (St 81 and Vu 86):

$$T_l(E)\ =\ \int\int T_l(E, R_1, R_2)\, W(R_1, R_2)\, dR_1\ dR_2 \tag{5.52}$$

where $T_l(E, R_1, R_2)$ is obtained from a one–dimensional barrier penetration model. The fusion cross sections are then calculated from these penetrabilities (see 5.26 and 5.37). The net effect of this procedure is that the fusion cross sections are significantly enhanced. Since ^{18}O is a heavily deformed nucleus, the nuclear deformation may help in understanding why the $^{18}O + ^{18}O$ reaction shows a fusion cross section much larger than those for the other oxygen isotope fusion reactions.

The $^{18}O + ^{18}O$ reactions form a rich topic for study. They display marvelous reaction features which are not seen in other, similar, light heavy–ion reactions. Several groups have studied some of the aspects of the $^{18}O + ^{18}O$ reactions. (Ka

77, Sh 70, Ku 79). They measured the angular distributions for elastic scattering, inelastic scattering and neutron–transfer reactions. However, none of these have studied the fusion reactions. At this point, we are the only investigators who have simultaneously studied the cross sections for the fusion reactions, inelastic scattering and the transfer reactions. Our experimental results and analyses should be supplemented by further exploration of the $^{18}O + {}^{18}O$ reactions. Immediately suggested experiments are the determination of accurate cross sections and angular distributions for both transfer reactions and inelastic scattering at near– and sub–barrier energies. A more detailed theoretical analysis of the proposed measurements with DWBA and CCBA (coupled–channel Born approximation) would likely result in improved knowledge of both the structure of the ^{18}O nucleus and the mechanisms of the $^{18}O + {}^{18}O$ reactions.

Ultimately, heavy ion cross sections determined from the fusion residue γ–cascades should be compared with those obtained by direct detection of the fusion residues in a recoil spectrometer system to verify the procedure used here. Up to this time, the recoil spectrometer technique has not been applied in the light heavy–ion region of nuclei, except at energies far above the barrier. It will likely be difficult to extend the direct measurement of the fusion residues far below the interaction barrier because of the exponentially decreasing fusion cross section and the rapidly increasing Coulomb scattering cross section. The latter makes it difficult at low energies to separate the fusion residues from the enormously greater yield of elastic events.

REFERENCES

(Aj 78) F. Ajzenberg–Selove, Nucl. Phys. **A300**, 1 (1978).

(Ak 80) O. Akyuz and A. Winther, in
Proceedings of the Enrico Fermi International School of Physics
(ed. R.A.Broglia, *et al.*) North–Holland (1980).

(Al 56) K. Alder, *et al.* Rev. Mod. Phys. **28**, 432 (1956).

(As 85) R. J. Ascutto and E. A. Segle. in
Treatise on Heavy–Ion Science **vol 1**
(ed. D.A.Bromley) Plenum Press (1985).

(Ba 83) A. B. Balantekin, S. E. Koonin, J.W.Negele,
Phys. Rev. **C28**, 1565 (1983).

(Ba 85) C. A. Barnes, S. Trentalange, S–C. Wu. in
Treatise on Heavy–Ion Science **vol 6**
(ed. D.A.Bromley) Plenum Press (1985).

(Be 69) F. D. Bechetti, and G. W. Greenless, Phys. Rev **182**, 1190 (1969).

(Be 85) M. Beckerman, Phys. Rep. **129**, 145 (1985).

(Bo 74) W.W.Bowman and K.W.MacMurdo,
Atomic Data and Nuclear Data Tables **13**, 89 (1974).

(Ch 77a) P. R. Christensen, Z. E. Switkowski and R.D.Dayras,
Nucl. Phys. **A280**, 189 (1977).

(Ch 77b) W. K. Chu. in *Ion Beam Handbook For Material Analysis*
(ed. J. W. Mayer and Z. Rimini). Academic Press, Inc. (1977).

(Ei 77) Y. Eisen *et al*, Nucl. Phys. **A291**, 459 (1977).

(En 78) P. M. Endt, C. Van. Der. Leun, Nucl. Phys. **A310**, 1 (1978).

(Ey 76) Y. Eyal, *et al.* Phys. Rev. **C13**, 1527 (1976).

(Fr 84) P. Fröbrich, Phys. Rep. **116**, 339 (1984).

(Ga 83) M. Gai *et al.* Phys. Rev.Lett. **50**, 239 (1983).

(Ga 86) E. N. Gazis *et al.* Phys. Rev. **C34**, 872 (1986).

(Gi 65) A. Gilbert and A. G.W. Cameron,Can. J. Phys. **43**, 1446 (1965).

(Ha 52) W. Hauser and H. Feshbach, Phys. Rev. **87**, 366 (1952).

(Ho 65) J.T.Holdman and R.M.Thaler, Phys. Rev. Lett. **14**, 81 (1965).

(Ho 76) J. A. Holmes Ph.D. Thesis, Caltech, Pasadena, (1976) Unpublished.

(Ho 78) P. E. Hodgson, *Nuclear Heavy-Ion Reactions* Clarendon Press (1978).

(Ka 75) D. Kalinsky *et al*, Nucl. Phys. **A250**, 364 (1975).

(Ka 77) D. Kalinsky *et al*, Nucl. Phys. **A289**, 205 (1977).

(Ku 79) S. Kubono.*et al*, Nucl. Phys. **A313**, 434 (1979).

(Ku 87) P. D. Kunz. Private communication, 1987. Unpublished.

(La 85) S. Landowne. in *Fusion Reactions Below the Coulomb Barrier* (ed. S. Steadman) Springer (1985).

(Le 78) C.Michael Lederer and Virginia S.Shirley (eds), *Table of Isotopes* Wiley Interscience (1978).

(Mc 66) L. McFadden and G. R. Satchler, Nucl. Phys. **84**, 177 (1966).

(Mo 85) Ulrich Mosel. in *Treatise on Heavy-Ion Science.* **vol 2** (ed. D.A.Bromley) Plenum Press (1985).

(No 70) L. C. Northcliffe, R. F. Schilling, Nucl. Data. **A7**, 233 (1970).

(Pe 74) C. M. Perey and F. G. Perey, Atomic Data and Nuclear Data. Tables. **13**, 293 (1974).

(Ph 76) D. Phillips and J. P. S. Pringle, Nucl. Instrum. Methods **135**, 389 (1976).

(Pr 72) J. P. S. Pringle, J. Electrochem. Soc. **119**, 482 (1972).

(Ra 66) G. H. Rawitscher. Nucl. Phys. **85**, 337 (1966).

(Ra 84) W. D. M. Rae and R. K. Bhowmik, Nucl. Phys. **A427**, 142 (1984).

(Sh 70) R.W.Shaw, R.Vandenbosch and M.K.Mehta, Phys. Rev. Lett **25**, 457 (1970).

(St 81) R. G.Stokstad, E. E. Gross. Phys. Rev. **C23**, 281 (1981).

(Th 86) J. Thomas *et al.* Phys. Rev. **C33**, 1679 (1986).

(Th 87) J. Thomas. Private communication, 1987. Unpublished.

(Tr 80) W.Treu, H.Fröhlich, P.Dück and H.Voit, Phys. Rev **C22**, 2462 (1980).

(Va 81) L. C. Vaz and J. M. Alexander, in *Fusion Reactions Below the Coulomb Barrier* (ed. S.Steadman) Springer (1985).

(Va 74) R. Vandenbosch, W. N. Reisdorf and P. H. Lau, Nucl. Phys. **A230**, 59 (1974).

(Vu 86) E. Vulgaris *et al.* Phys. Rev. **C33**, 2017 (1986).

(Wi 64) D. Wilmore and P. E. Hodgson, Nucl. Phys. **55**, 673 (1964).

(Wu 86) S–C Wu. Private communication to A. Winther and J. Thomas, 1986.

TABLE 1

Efficiency of Ge Detector

The Ge detector efficiency was calibrated in the same geometry as that used in the experiment. The sources used to calibrate the detector are listed, with their γ-ray energies.

The efficiencies listed are full-energy-peak efficiencies.

The curve of the efficiencies versus γ–ray energy is drawn in fig.13.

Table 1

Efficiency of Ge detector

γ Energy KeV	Efficiency %	Source
276.4	1.50±0.06	^{133}Ba
302.8	1.81±0.07	^{133}Ba
356.0	2.12±0.08	^{133}Ba
380.5	2.21±0.08	^{125}Sb
383.9	2.26±0.09	^{133}Ba
427.9	2.27±0.09	^{125}Ba
463.5	2.25±0.09	^{125}Sb
511.0	2.20±0.08	^{22}Na
635.9	2.08±0.08	^{125}Sb
661.6	2.05±0.07	^{137}Cs
846.8	1.88±0.08	^{56}Co
1173.2	1.58±0.06	^{60}Co
1238.3	1.51±0.07	^{56}Co
1274.6	1.46±0.05	^{22}Na
1332.5	1.46±0.05	^{60}Co
1771.5	1.10±0.05	^{56}Co
1836.0	1.11±0.06	^{88}Y
2034.9	0.97±0.06	^{56}Co
2598.4	0.87±0.06	^{56}Co
3253.6	0.73±0.06	^{56}Co

TABLE 2

Gamma–Ray Identification

The γ–ray transitions observed in the $^{18}O + ^{18}O$ reactions, as full energy peaks in the spectra in Fig.8 and 9, are identified in this table. The exit channels, which correspond to these γ–emitters, are also listed.

Table 2

γ Rays Identification in $^{18}O + ^{18}O$

Exit Channel	γ–Transition	γ Energy
$^{18}O(^{18}O, 2n)^{34}S$	2127 → 0.00 keV	2127 keV
	3304 → 0.00 keV	3304 keV
	4622 → 3304 keV	1318 keV
	4622 → 2127 keV	2495 keV
	4688 → 2127 keV	2561 keV
	5689 → 4622 keV	1067 keV
	5689 → 4689 keV	1001 keV
$^{18}O(^{18}O, np)^{34}P$	429 → 0.00 keV	429 keV
	2320 → 429 keV	1891 keV
$^{18}O(^{18}O, n\alpha)^{31}S$	1695 →0.00 keV	1695 keV
	752.5 → 0.00 keV	752.5 keV
	3133 → 1695 keV	1438 keV
$^{18}O(^{18}O, 2\alpha)^{28}Mg$	1474 →0.00 keV	1474 keV
$^{28}Mg \xrightarrow{\beta^-} {}^{28}Al$	1373 → 30.6 keV	1342 keV
	1373 → 972 keV	401 keV
$^{18}O(^{18}O, 3\alpha)^{24}Ne$		
$^{24}Ne \xrightarrow{\beta^-} {}^{24}Na$	472.3 → 0.00 keV	472.3 keV
$^{24}Na \xrightarrow{\beta^-} {}^{24}Mg$	4123 → 1369 keV	2754 keV
	1369 → 0.00 keV	1369 keV
$^{18}O(^{18}O, 3n)^{33}S$	2934 → 1966 keV	967.3 keV
	1966 → 0.00 keV	1966 keV
	4866 →2934 keV	1933 keV
$^{18}O(^{18}O, 2np)^{33}P$	1431 → 0.00 keV	1431 keV
	1848 → 0.00 keV	1848 keV
	1848 → 1431 keV	417 keV
	3627 → 1848 keV	1779 keV
	5638 → 4226 keV	1412 keV
	5453 → 4226 keV	1227 keV
	4226 → 1848 keV	2478 keV

Table 2 (cont'd)

γ Rays Identification in $^{18}O + ^{18}O$

Exit Channel	γ–Transition	γ Energy
$^{18}O(^{18}O, 2n\alpha)^{30}Si$	2236 → 0.00 keV	2236 keV
	5950 → 2236 keV	3714 keV
	7044 → 5950 keV	1094 keV
	3498 → 2236 keV	1262 keV
	5950 → 3498 keV	2452 keV
	5279 → 2236 keV	3043 keV
	3498 → 0.00 keV	3498 keV
$^{18}O(^{18}O, 3n\alpha)^{29}Si$	1273 → 0.00 keV	1273 keV
	2028 → 0.00 keV	2028 keV
	2425 → 0.00 keV	2425 keV
	3067 → 2028 keV	1039 keV
$^{18}O(^{18}O, 2np\alpha)^{29}Al$		
$^{29}Al \xrightarrow{\beta^-} {}^{29}Si$	1273 → 0.00 keV	1273 keV
	2028 → 0.00 keV	2028 keV
	2426 → 0.00 keV	2426 keV
$^{18}O(^{18}O, n2\alpha)^{27}Mg$		
$^{27}Mg \xrightarrow{\beta^-} {}^{27}Al$	844 → 0.00 keV	844 keV
	1014 → 0.00 keV	1014 keV
$^{18}O(^{18}O, ^{18}O)^{18}O^*$	1982→0.00 keV	1982 keV
$^{18}O(^{18}O, ^{16}O)^{20}O^*$	1674→0.00 keV	1674 keV
$^{18}O(^{18}O, ^{16}O)^{20}O$		
$^{20}O \xrightarrow{\beta^-} {}^{20}F$	1057 → 0.00 keV	1057 keV
$^{20}F \xrightarrow{\beta^-} {}^{20}Ne$	1633 → 0.00 keV	1633 keV
$^{18}O(^{18}O, ^{17}O)^{19}O$		
$^{19}O \xrightarrow{\beta^-} {}^{19}F$	1554 → 197 keV	1357 keV

TABLE 3

Gamma–Ray Angular Distributions

The γ–rays from the $^{18}O + {}^{18}O$ reactions were detected by a Ge detector, which was set 4 inches from target at 0° and 90°, with respect to the beam line. $W(0°)/W(90°)$ are the ratios of the photopeak areas of each γ–ray at 0° and 90° detection respectively. The γ–ray angular distributions were assumed to be of the form:

$$W(\theta) \sim 1 + a\cos^2\theta$$

Table 3

γ Ray Angular Distribution in $^{18}O + ^{18}O$

γ Energy	Exit Channel	Transition	$\frac{W(0°)}{W(90°)}$	a
429 keV	$^{18}O(^{18}O, np)^{34}P$	429→ 0 keV	0.85	–0.16
967 keV	$^{18}O(^{18}O, 3n)^{33}S$	2934→1966 keV	0.75	–0.26
1002 keV	$^{18}O(^{18}O, 3n)^{33}S$	2969→1966 keV	0.86	–0.15
1057 keV	$^{18}O(^{18}O, ^{16}O)^{20}O$ $^{20}O \xrightarrow{\beta^-} {}^{20}F$	1057→0 keV	1.01	0.01
1067 keV	$^{18}O(^{18}O, 2n)^{34}S$	5689→4622 keV	1.23	0.24
1273 keV	$^{18}O(^{18}O, 3n\alpha)^{29}Si$	1273→0 keV	0.96	0.04
1431 keV	$^{18}O(^{18}O, 2np)^{33}P$	1431→0 keV	1.13	0.14
1633 keV	$^{18}O(^{18}O, ^{16}O)^{20}O$ $^{20}O \xrightarrow{\beta^-} {}^{20}F \xrightarrow{\beta^-} {}^{20}Ne$	1633→0 keV	0.99	–0.01
1695 keV	$^{18}O(^{18}O, n\alpha)^{31}Si$	1695→0 keV	1.20	0.21
1848 keV	$^{18}O(^{18}O, 2np)^{33}P$	1848→0 keV	1.07	0.07
1878 keV	$^{18}O(^{18}O, np)^{34}P$	2307→429 keV	1.16	0.17
1966 keV	$^{18}O(^{18}O, 3n)^{33}S$	1966→0 keV	1.14	0.15
1982 keV	$^{18}O(^{18}O, ^{18}O)^{18}O^*$	1982→0 keV	1.07	0.07
2127 keV	$^{18}O(^{18}O, 2n)^{34}S$	2127→0 keV	1.09	0.09
2236 keV	$^{18}O(^{18}O, 2n\alpha)^{30}Si$	2236→0 keV	0.99	–0.01

TABLE 4

Level Density Parameters

The level density parameters are defined in section IV.B. The parameters E_0 and T were obtained by fitting to the known bound state levels. All P's, S's and q's were taken from ref (Ho 76). The coefficients a's and back–shift Δ's were calculated with formulae given in IV.B.

Table 4

Parameters of Level Density part(1)

Nucleus	P(Z)	P(N)	S(Z)	S(N)	q_1	q_2	A^{q_3}
^{36}S	1.622	2.039	–9.696	11.392	0.05267	0.001901	73.7
^{35}S	1.622	0.000	–9.696	10.598	0.05260	0.002210	71.3
^{34}S	1.622	1.859	–9.696	9.813	0.05267	0.001901	68.8
^{33}S	1.622	0.000	–9.696	8.936	0.05260	0.002210	66.4
^{35}P	0.000	2.039	–8.969	11.392	0.05260	0.002210	71.3
^{34}P	0.000	0.000	–8.969	10.598	0.05264	0.001593	68.8
^{33}P	0.000	1.859	–8.969	9.813	0.05260	0.002210	66.4
^{34}Si	2.089	2.039	–7.799	11.392	0.05267	0.001901	68.8
^{33}Si	2.089	0.000	–7.799	10.598	0.05260	0.002210	66.4
^{32}Si	2.089	1.859	–7.799	9.813	0.05267	0.001901	64.0
^{31}Si	2.089	0.000	–7.799	8.936	0.05260	0.002216	61.6
^{30}Si	2.089	1.671	–7.799	8.065	0.05260	0.002210	59.2
^{29}Si	2.089	0.000	–7.799	7.437	0.05260	0.002210	56.9
^{31}Al	0.000	1.859	–5.723	9.813	0.05260	0.002210	61.6
^{30}Al	0.000	0.000	–5.723	8.936	0.05264	0.001593	59.2
^{29}Al	0.000	1.671	–5.723	8.065	0.05260	0.002210	56.9
^{28}Mg	2.463	1.671	–4.168	8.065	0.05267	0.001901	54.5
^{27}Mg	2.463	0.000	–4.168	7.437	0.05260	0.002210	52.2
^{24}Ne	2.500	1.795	–0.811	7.212	0.05267	0.001901	45.3

Table 4

Parameters of Level Density part(2)

Nucleus	T	E_0	U'	Δ	a
^{36}S	2.472	0.428	6.666	1.439	4.119
^{35}S	2.115	–1.581	6.785	–0.664	3.893
^{34}S	1.614	1.312	6.912	1.128	3.639
^{33}S	1.675	–0.149	7.045	–0.802	3.381
^{35}P	1.957	–0.550	6.786	–0.247	4.132
^{34}P	1.950	–1.725	6.912	–2.353	3.800
^{33}P	1.839	0.252	7.045	–0.565	3.610
^{34}Si	2.310	0.714	6.912	1.775	4.094
^{33}Si	2.044	–0.937	7.045	–0.335	3.903
^{32}Si	1.275	2.977	7.187	1.448	3.616
^{31}Si	1.974	–0.293	7.339	–0.492	3.395
^{30}Si	2.327	0.080	7.500	1.093	3.148
^{29}Si	2.181	–0.042	7.672	–0.670	2.947
^{31}Al	1.938	0.661	7.339	–0.722	3.797
^{30}Al	2.118	–2.63	7.500	–2.667	3.419
^{29}Al	2.036	1.099	7.672	–1.088	3.287
^{28}Mg	1.811	1.157	7.857	1.277	3.274
^{27}Mg	1.863	–0.431	8.055	–0.500	3.122
^{24}Ne	2.170	2.800	8.752	0.962	2.937

TABLE 5

The $^{18}O + ^{18}O$ Cross Sections

The measured cross sections for fusion, inelastic scattering and two–neutron transfer reactions are listed. Also the partial fusion cross sections are given in part(2), part(3) and part(4) of this table. These experimental cross sections are plotted in Fig.22. The listed errors for total fusion reaction cross sections are statistical errors only.

Table 5

$^{18}O + {}^{18}O$ Cross Sections part(1)

$E_{c.m}$ (MeV)	σ_{total}	σ_{fusion}(error)	$\sigma_{transfer}$	σ_{inel}
6.73	0.034	0.033(35%)	0.000	0.001
6.98	0.083	0.080(20%)	0.000	0.003
7.23	0.264	0.254(10%)	0.002	0.008
7.48	0.633	0.613 (6%)	0.005	0.015
7.73	1.53	1.48 (6%)	0.017	0.028
7.98	3.20	3.11 (5%)	0.033	0.050
8.23	6.98	6.81 (5%)	0.082	0.086
8.49	14.54	14.14 (5%)	0.231	0.16
8.73	25.06	24.53 (5%)	0.341	0.19
8.98	42.21	41.26 (5%)	0.613	0.34
9.23	75.93	74.49 (5%)	1.11	0.33
9.49	111.6	110.0 (4%)	1.18	0.43
9.74	153.6	150.1 (4%)	2.96	0.57
9.99	201.4	195.9 (4%)	4.10	1.31
10.24	272.6	265.5 (4%)	5.18	1.85
10.49	337.8	326.8 (4%)	7.17	3.87
10.74	398.9	385.8 (4%)	7.93	5.12
10.99	449.9	434.4 (4%)	8.89	6.67
11.24	509.7	489.7 (4%)	10.16	9.86
11.49	580.4	558.4 (4%)	10.34	11.6
11.74	652.5	626.9 (4%)	12.0	13.6
11.99	714.0	685.0 (4%)	11.0	18.0
12.24	764.3	733.3 (4%)	11.5	19.5
12.49	813.2	780.3 (4%)	11.7	21.2
12.74	912.9	877.9 (4%)	11.9	23.1
13.24	966.5	925.2 (4%)	12.0	29.3

Note : all cross sections are in mb .

σ_{fusion} = sum over all fusion channels.

$\sigma_{transfer}$= two neutron transfer cross section (α transfer is not included).

σ_{inel} = inelastic scattering cross section.

$\sigma_{total} = \sigma_{fusion} + \sigma_{transfer} + \sigma_{inel}$.

Table 5 $^{18}O + ^{18}O$ **Cross Sections part(2)**

$E_{c.m}$ (MeV)	^{34}S+2n	^{34}P+np	^{33}S+3n	^{33}P+2np	^{31}Si+nα
6.73	0.008	0.004	0.006	0.003	0.004
6.98	0.016	0.009	0.015	0.008	0.010
7.23	0.047	0.023	0.042	0.022	0.032
7.48	0.114	0.039	0.130	0.057	0.062
7.73	0.230	0.095	0.343	0.106	0.113
7.98	0.540	0.186	0.625	0.306	0.268
8.23	1.01	0.397	1.70	0.816	0.462
8.49	2.05	0.820	3.43	1.39	0.923
8.73	3.23	1.38	5.34	2.59	1.85
8.98	5.53	2.19	9.02	5.80	2.61
9.23	8.83	3.51	17.3	11.3	5.23
9.49	11.7	5.36	29.7	13.9	6.67
9.74	13.5	7.14	37.7	21.5	9.50
9.99	20.8	8.81	48.9	25.4	14.8
10.24	24.1	10.7	67.2	40.0	18.4
10.49	26.1	11.7	83.2	41.7	20.9
10.74	28.0	12.8	96.9	65.7	21.7
10.99	29.8	14.6	131.9	64.4	23.8
11.24	32.9	15.9	152.2	78.8	24.8
11.49	33.9	17.1	153.0	85.5	29.9
11.74	33.1	19.0	168.5	110.0	28.5
11.99	38.1	18.5	193.3	108.3	34.6
12.24	38.8	20.0	203.3	118.8	33.0
12.49	41.9	21.1	230.1	125.8	34.5
12.74	44.5	20.8	245.0	169.0	35.6
13.24	48.2	19.2	237.0	173.9	37.1

Table 5 $^{18}O + {}^{18}O$ **Cross Sections part(3)**

$E_{c.m}$(MeV)	^{29}Si+3nα	^{29}Al+dpα	^{28}Mg+2α	^{27}Mg+n2α	^{16}O+$^{20}O^*$
6.73	0.002				
6.98	0.006	0.002			
7.23	0.016	0.008	0.001		
7.48	0.045		0.003		
7.73	0.110	0.058			
7.98	0.236		0.016		
8.23	0.520	0.084		0.023	
8.49	1.21		0.067		
8.73	2.28	0.208	0.092	0.068	
8.98	3.82		0.170		
9.23	7.26		0.260		
9.49	10.8	0.367	0.381	0.178	0.30
9.74	13.9		0.525		
9.99	18.0	0.43	0.635	0.520	
10.24	25.1		1.11		
10.49	30.1		1.21		
10.74	37.8	0.88	1.70	1.39	1.35
10.99	36.6		2.05		
11.24	47.8	1.18	2.55	1.75	1.57
11.49	55.6		2.60		
11.74	60.5		3.50		
11.99	61.4		3.42	3.34	2.56
12.24	69.0	1.50	3.74	3.49	
12.49	75.8		4.27	3.62	3.17
12.74	79.4		4.01		
13.24	75.3	1.55	3.89	5.11	3.74

Table 5 $^{18}O + ^{18}O$ **Cross Sections part(4)**

$E_{c.m}$(MeV)	^{30}Si+2nα	^{24}Ne+^{12}C	$^{22}Ne^* + ^{14}C$		
6.73	0.006		0.006		
6.98	0.014		0.014		
7.23	0.063		0.030		
7.48	0.163		0.053		
7.73	0.421		0.09		
7.98	0.926		0.17		
8.23	1.73	0.007	0.31		
8.49	4.11				
8.73	6.89	0.04			
8.98	12.0				
9.23	19.9				
9.49	30.4	0.08			
9.74	45.2				
9.99	56.7	0.16			
10.24	75.7				
10.49	100.9				
10.74	118.1				
10.99	127.9				
11.24	131.0	0.48			
11.49	156.0				
11.74	193.4				
11.99	225.6	0.60			
12.24	235.9				
12.49	239.6	0.73			
12.74	273.3				
13.24	323.3	0.65			

TABLE 6

Optical Potential Parameters

The optical potentials are assumed to be of the Woods–Saxon form:

$$V_N(r) = -Vf(r; R_r, a_r) - iW_v(r; R_v, a_v) + 4ia_sW_s\frac{d}{dr}f(r; R_s, a_s)$$

and

$$f(r; R_i, a_i) = \left\{1 + exp\left(\frac{r - R_i}{a_i}\right)\right\}^{-1}$$

The magnitudes of the optical potentials (V ,W_i) are given in MeV; the geometrical parameters (R_i and a_i) are in fm.

Table 6

Parameters of Optical Potential

Neutron : (From Wilmore and Hodgson .)

$V = 47.01 - 0.267\ E - 0.0018\ E^2$

$W_i = 0.00$

$W_s = 9.52 - 0.053\ E$

$R_r = [1.322 - 0.0076\ A\ (1.00 - 0.005\ A)]\ A^{\frac{1}{3}}$

$a_r = 0.66$

$R_s = [1.266 - 0.00037A(1.00 - 0.005\ A)]\ A^{\frac{1}{3}}$

$a_s = 0.48$

Proton : (From Becchetti and Greenlees .)

$V = 54.0 - 0.32\ E + 24.0\ (1.00 - 2\ Z/A) + 0.4\ Z\ A^{\frac{1}{3}}$

$W_i = -\ 2.7 + 0.22\ E$

$W_s = 11.8 - 0.25\ E + 12.0\ (1.00 - 2\ Z/A)$

$R_r = 1.17\ A^{\frac{1}{3}}$

$a_r = 0.75$

$R_i = R_s = 1.26\ A^{\frac{1}{3}}$

$a_i = a_s = 0.58$

Deuteron : (From Perey and Perey .)

$V = 81.0 - 0.22\ E + 2.0\ Z\ A^{\frac{1}{3}}$

$W_i = 0.00$

$W_s = 14.4$

$R_r = 1.15$

$a_r = 0.81$

$R_s = 1.34\ A^{\frac{1}{3}}$

$a_s = 0.68$

Triton : (From Becchetti and Greenlees .)

V = 136.4 – 0.17 E + 55.0 (1.00 – 2 Z/A)

W_i = 41.3 – 0.33 E + 63.0 (1.00 – 2 Z/A)

$W_s = 0.00$

$R_r = 1.20\ A^{\frac{1}{3}}$

$a_r = 0.72$

$R_i = 1.40\ A^{\frac{1}{3}}$

$a_i = 0.86$

Helium–3 : (From Becchetti and Greenlees .)

V = 165 – 0.17 E + 7 (1.00 – 2 Z/A)

W_i = 46.0 – 0.33 E – 110 (1.0 – 2 Z/A)

$W_s = 0.0000$

$R_r = 1.2\ A^{\frac{1}{3}}$

$a_r = 0.72$

$R_i = 1.4\ A^{\frac{1}{3}}$

$a_i = 0.86$

Alpha : (From Mcfadden and Satchler .)

V = 185

$W_i = 25.0$

$W_s = 0.0000$

$R_r = R_i = 1.40\ A^{\frac{1}{3}}$

$a_r = a_i = 0.52$

$^{18}O + {}^{18}O$ (From Kalinsky .)

V = 100.0

$W_i = 30.0$

$W_s = 0.0000$

$R_r = 6.289$

$R_i = 6.813$

$a_r = 0.51$

$a_i = 0.30$

$^{12}C + {}^{24}Ne$

V = 100.0

$W_i = 27.0$

$W_s = 0.0000$

$R_r = 6.51$

$R_i = 7.14$

$a_r = 0.48$

$a_i = 0.22$

FIGURE 1

$^{18}O + {}^{18}O$ Potential $V_l(r)$

The $^{18}O + {}^{18}O$ potential, i.e., the sum of the optical potential (real part), Coulomb potential and centrifugal potential, is plotted as a function of the inter–nuclear distance r for several orbital angular momentum values l.

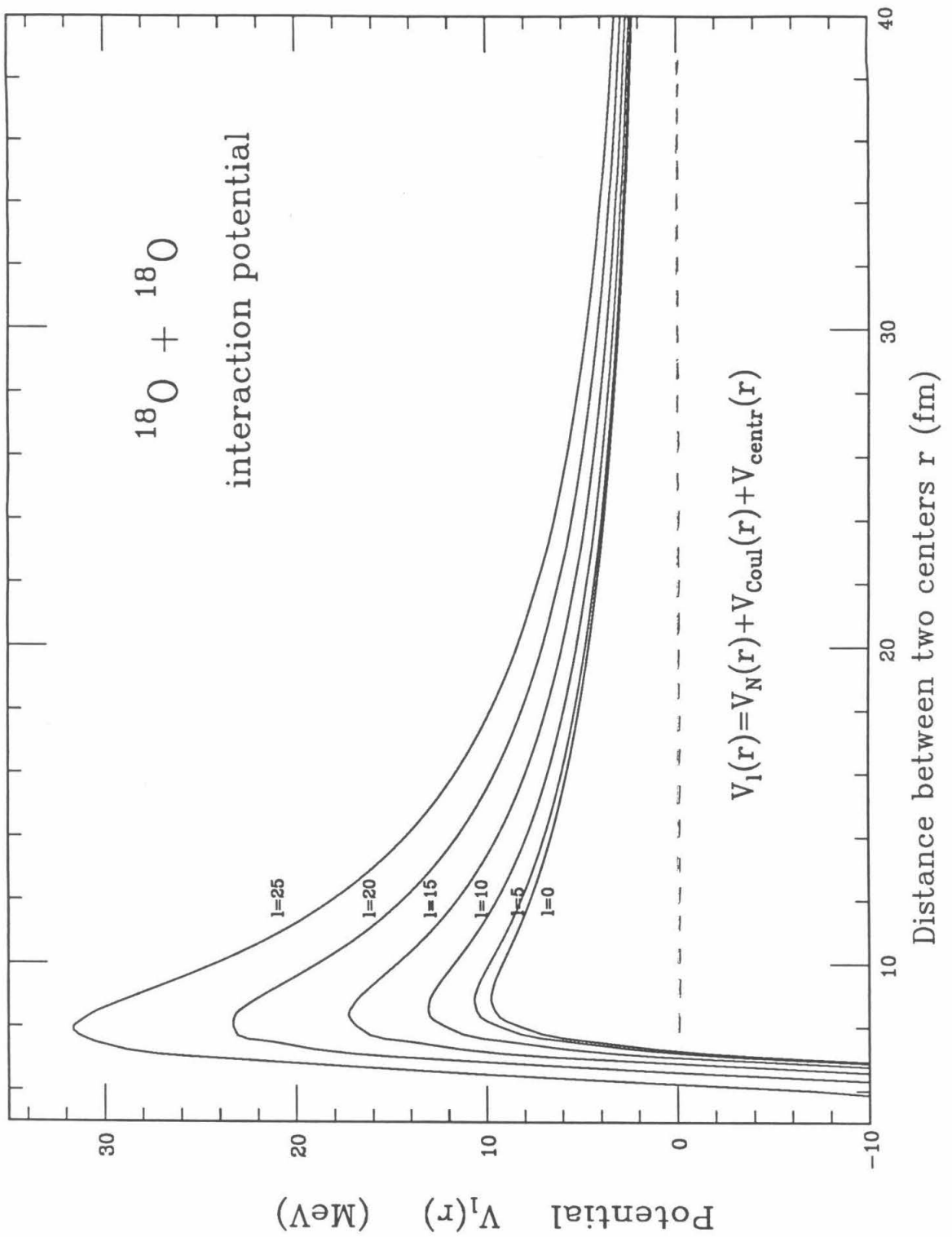
$^{18}O + ^{18}O$
interaction potential
$V_l(r)=V_N(r)+V_{Coul}(r)+V_{centr}(r)$
l=25
l=20
l=15
l=10
l=5
l=0
Potential $V_l(r)$ (MeV)
Distance between two centers r (fm)
30
20
10
0
-10
10
20
30
40

FIGURE 2

Classical Picture of Heavy–Ion Collision

This is a classification scheme of heavy–ion interactions showing the classical trajectories corresponding to distant, peripheral, dissipative, and penetrating collisions. The quantity R_c denotes the distance of closest approach (associated with the impact parameter). Its relation to the interaction radius $R_{int} = R_1 + R_2$ determines the character of the reaction.

b_{gr} corresponds to a grazing impact parameter, K_∞ is the wave number when the incoming ion is at $-\infty$.

SCHEME OF COLLISIONS

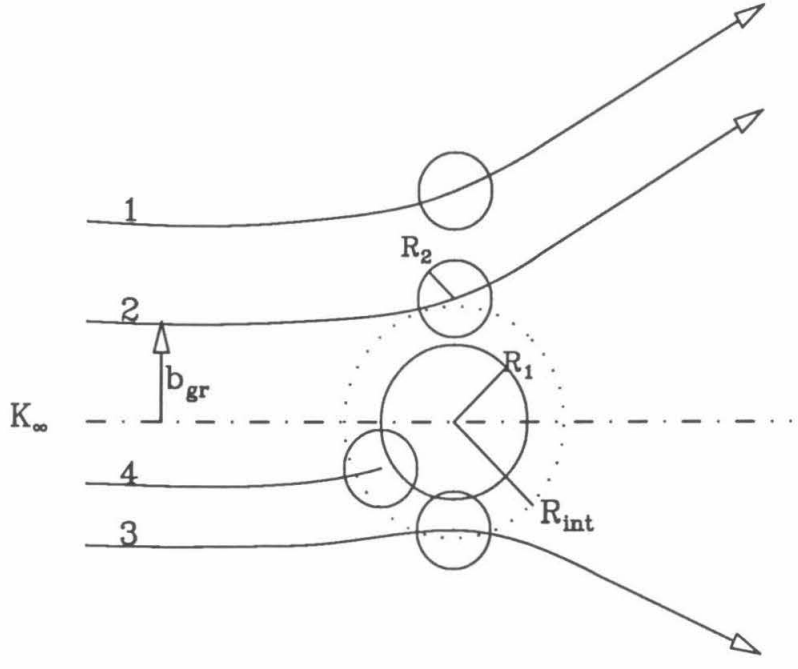

REACTION CHARACTERISTECS

1. $R_c > R_{int}$ distant collision

(elastic scattering & Coulomb excitation)

2. $R_c \sim R_{int}$ peripheral collision

(inelastic scattering & nucleon exchange)

3. $R_c < R_{int}$ dissipative collision

(deep inelastic reactions)

4. $R_c \sim 0$ penetrating collision

(compound nuclear formation & evaporation)

FIGURE 3

Above–Barrier Cross Section of $^{20}Ne + ^{27}Al$

The measured fusion excitation function for $^{20}Ne+^{27}Al$ as a function of $1/E_{c.m}$ is compared with a surface friction model calculation (solid line) of P. Fröbrich (Fr.84). At higher energies complete fusion (dots) and incomplete+complete fusion (squares) are different. The measured total reaction cross section (crosses) is also shown.

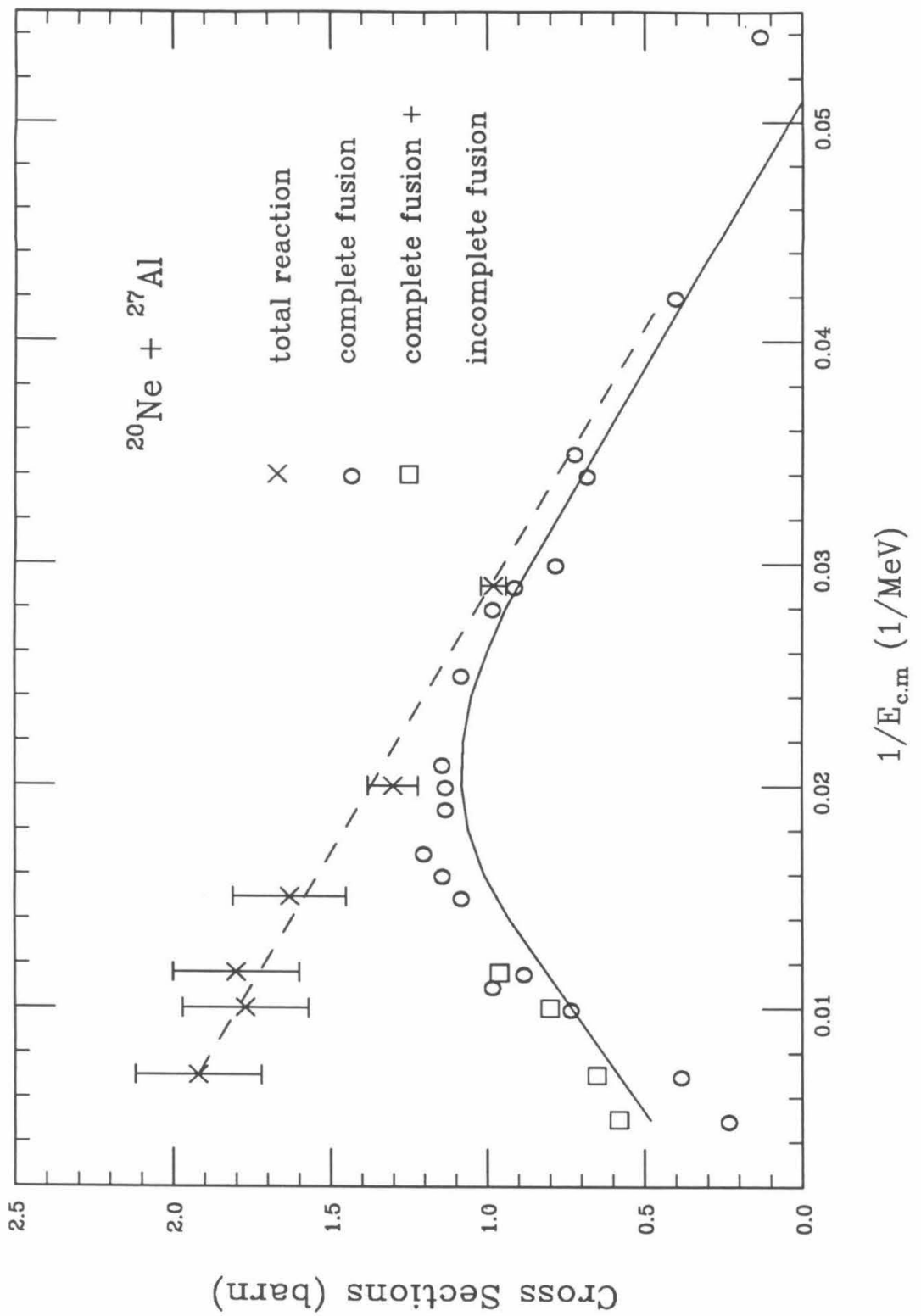
$^{20}Ne + ^{27}Al$
total reaction
complete fusion
complete fusion + incomplete fusion
Cross Sections (barn)
$1/E_{c.m}$ (1/MeV)
0.0
0.5
1.0
1.5
2.0
2.5
0.01
0.02
0.03
0.04
0.05

FIGURE 4

Partial Wave Contributions

The partial wave contributions to the fusion cross section for $^{18}O + ^{18}O$ are given as a function of energy. The fraction of the reaction strength in each partial wave was computed from the transmission functions of an optical model. The optical potentials used here are listed in table 6 of present work and in table 1 of ref.(Ka 77). The general features of these curves are not very sensitive to the choice of optical potential. Curves are labeled with their orbital angular momentum l. Only even l waves contribute to the fusion reaction for $^{18}O + ^{18}O$ since the colliding particles are identical spinless bosons.

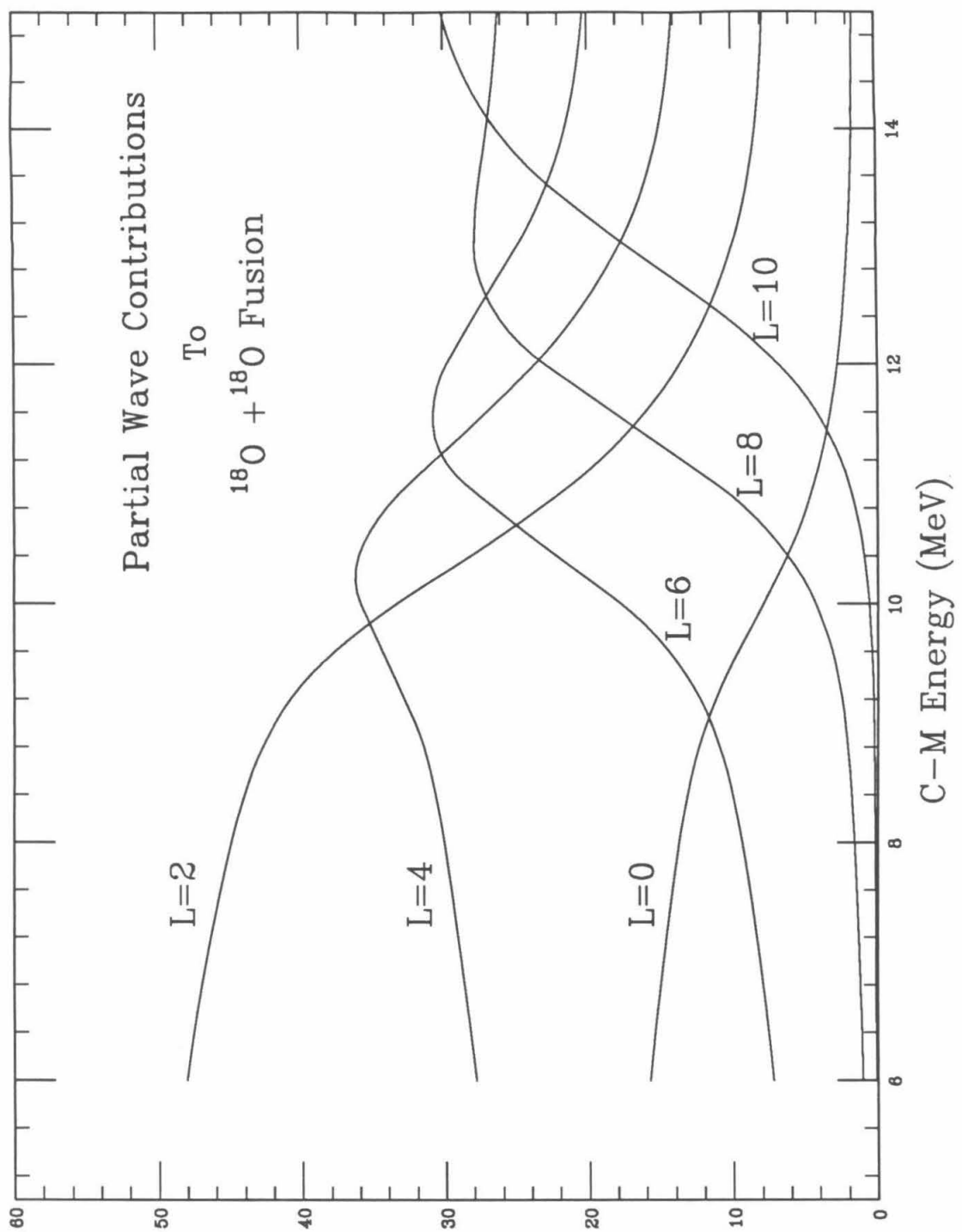
Partial Wave Contributions
To
$^{18}O + ^{18}O$ Fusion
L=2
L=4
L=0
L=6
L=8
L=10
Fraction (%)
C-M Energy (MeV)
0
10
20
30
40
50
60
6
8
10
12
14

FIGURE 5

Schematic Representation of Fusion Products

For fusion reactions involving moderately heavy nuclei ($A \geq 40$), only a small transverse momentum is imparted to the recoiling nucleus by emitted particles. Thus the evaporation residues recoil in a tight cone about the beam axis. In light heavy–ion reactions things are slightly different, because the fraction of the momentum carried by α, n, p and other particles is not as small as in heavier ion collisions. Thus the recoiling residues are more spread out.

If the life–time, τ, of the residual nucleus is smaller than or comparable to its stopping time, t_{sp}, in target material, $\tau \leq t_{sp}$, Doppler shifting and broadening occur. In the present situation $t_{sp} \approx 1$ ps.

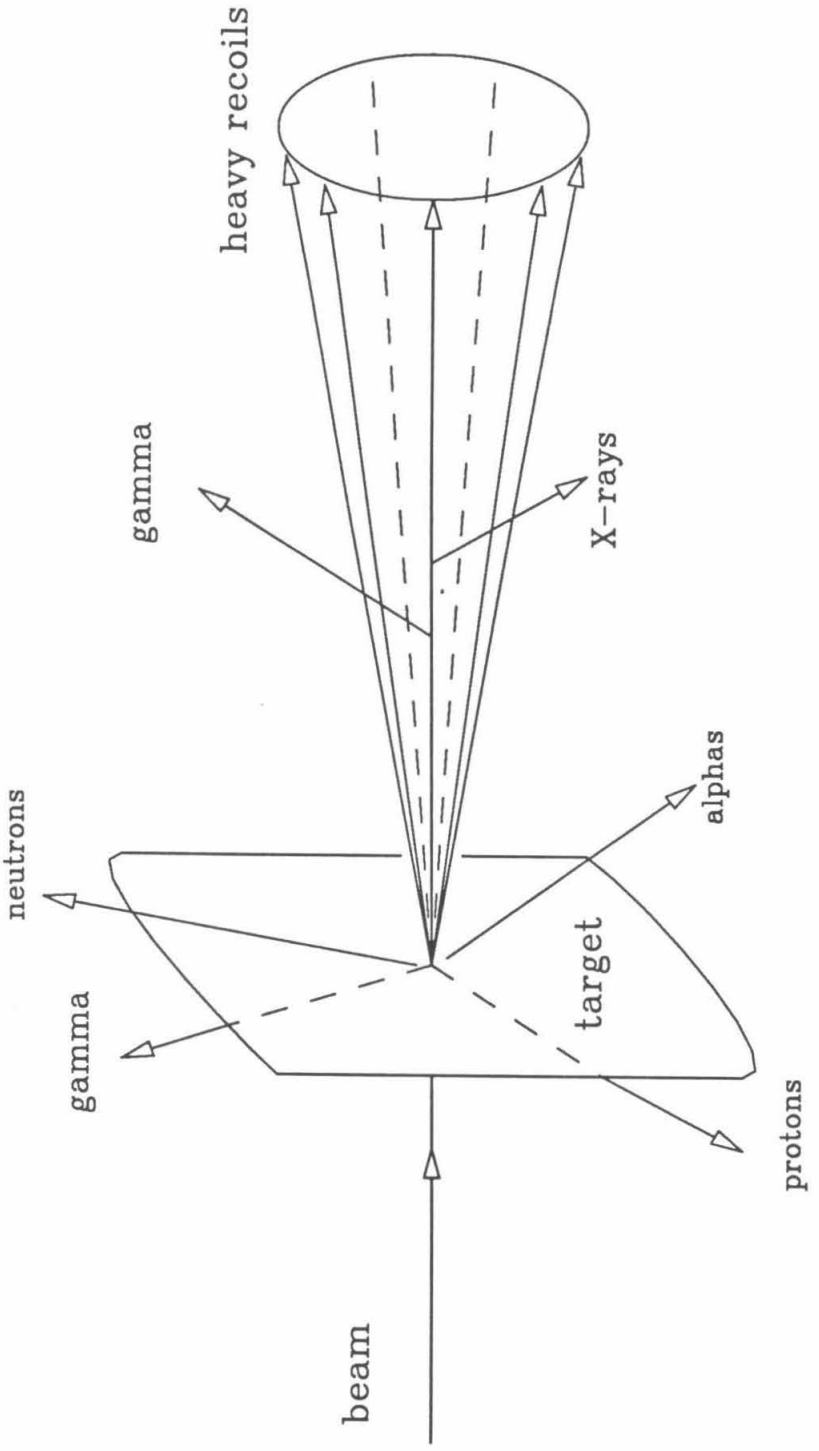
heavy recoils
gamma
X-rays
neutrons
alphas
gamma
target
protons
beam

Figure 6

Energy Levels of Oxygen Isotopes

Energy levels of ^{17}O and ^{18}O with the decay threshold into ^{16}O+neutron(s) as zero energy. The levels of the band for $\alpha + {}^{14}C$ clusters in ^{18}O are plotted. They are:

0^+(3.65 MeV) 1^-(4.45 MeV) 2^+(5.26 MeV)

3^-(8.29 MeV) 4^+(10.26 MeV).

The head of this band is a 2h–4p state (Ga 83).

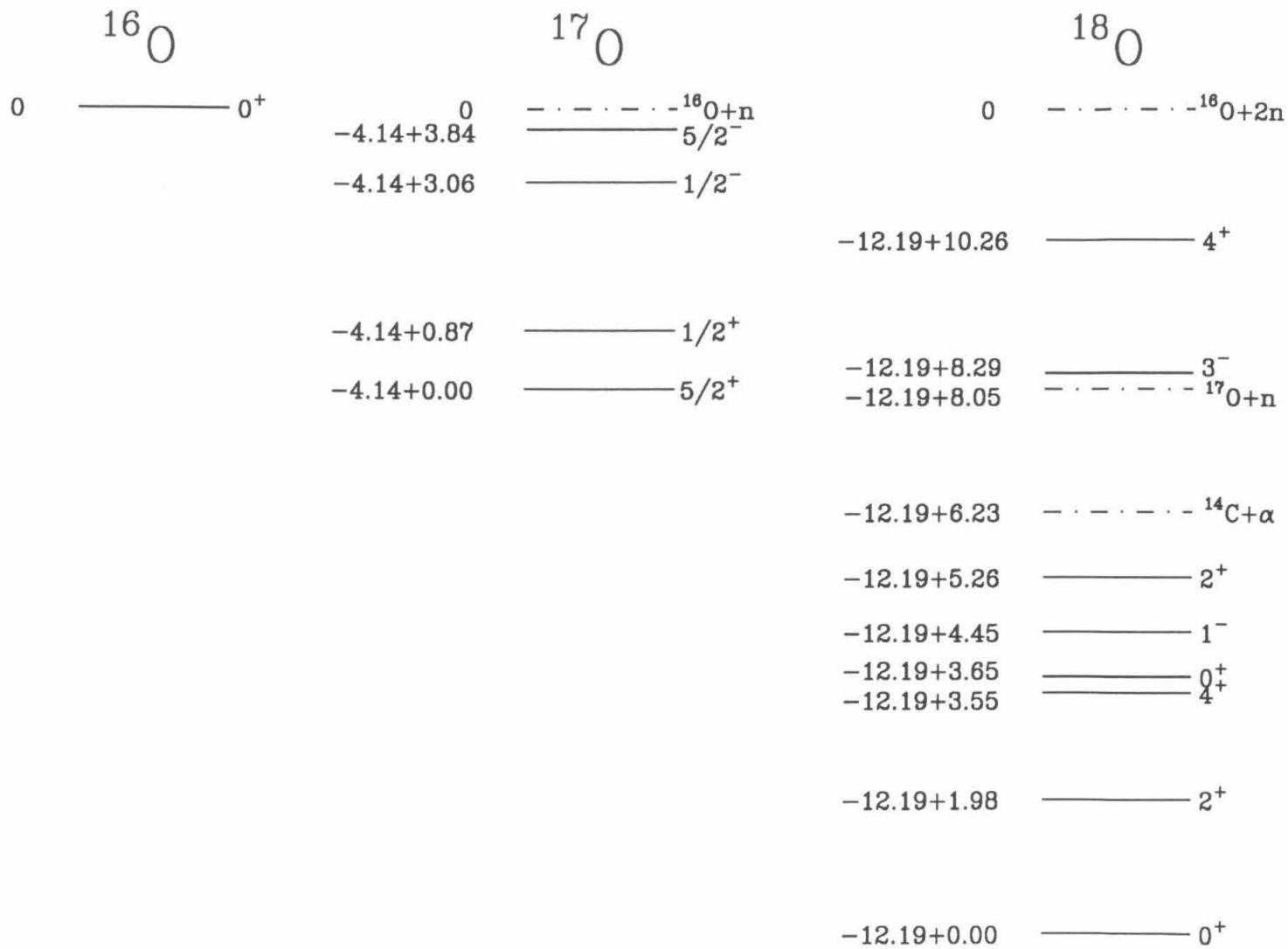
^{16}O
^{17}O
^{18}O
0
0^+
0
$^{16}O+n$
$-4.14+3.84$
$5/2^-$
$-4.14+3.06$
$1/2^-$
$-4.14+0.87$
$1/2^+$
$-4.14+0.00$
$5/2^+$
$-12.19+10.26$
4^+
$-12.19+8.29$
3^-
$-12.19+8.05$
$^{17}O+n$
$-12.19+6.23$
$^{14}C+\alpha$
$-12.19+5.26$
2^+
$-12.19+4.45$
1^-
$-12.19+3.65$
0^+
$-12.19+3.55$
4^+
$-12.19+1.98$
2^+
$-12.19+0.00$
0^+
$^{16}O+2n$

FIGURE 7

Experimental Apparatus

The Ge detector, target, and ultra–high vacuum target chamber used to measure the fusion cross section were set up on the center beamline of the ONR–Caltech EN tandem. The experimental apparatus is described more fully in section II.A.

This figure is schematic only (not to scale).

G — Ge detector; T — target; M — Magnet to supress secondary electros;

A — aperture; P — ion pump; N — LN cold trap;

L — lead bricks; W — cooling water; S — sorption pump;

B — beam line; V — valves; C — ceramic tube.

EXPERIMENTAL APPARATUS

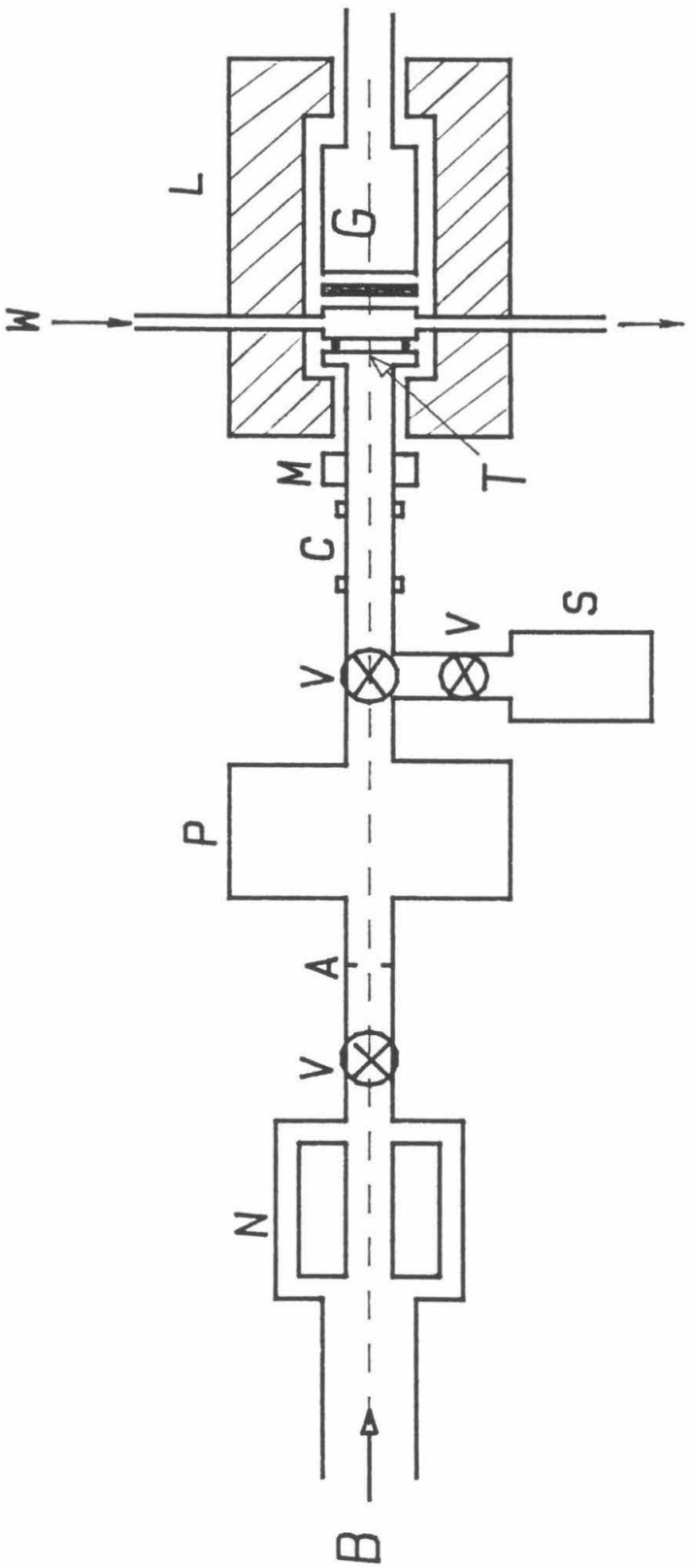

FIGURE 8

$^{18}O + ^{18}O$ γ–Spectrum at Beam Energy 20 MeV

This is a sample of the γ–ray pulse–height spectra for an ^{18}O beam on an ^{18}O target in the close target–detector geometry. The data were recorded in a 4096 channel MCA. The energy calibration is such that the γ–ray energy, in keV, is close to the channel number. Note the strong Doppler broadening of the peaks, such as ^{29}Si $E_\gamma = 1274$ keV, ^{33}S $E_\gamma = 1966$ keV, ^{34}S $E_\gamma = 2127$ keV, and ^{30}Si $E_\gamma = 2236$ keV peaks. The details of the γ–ray identification are given in table 2.

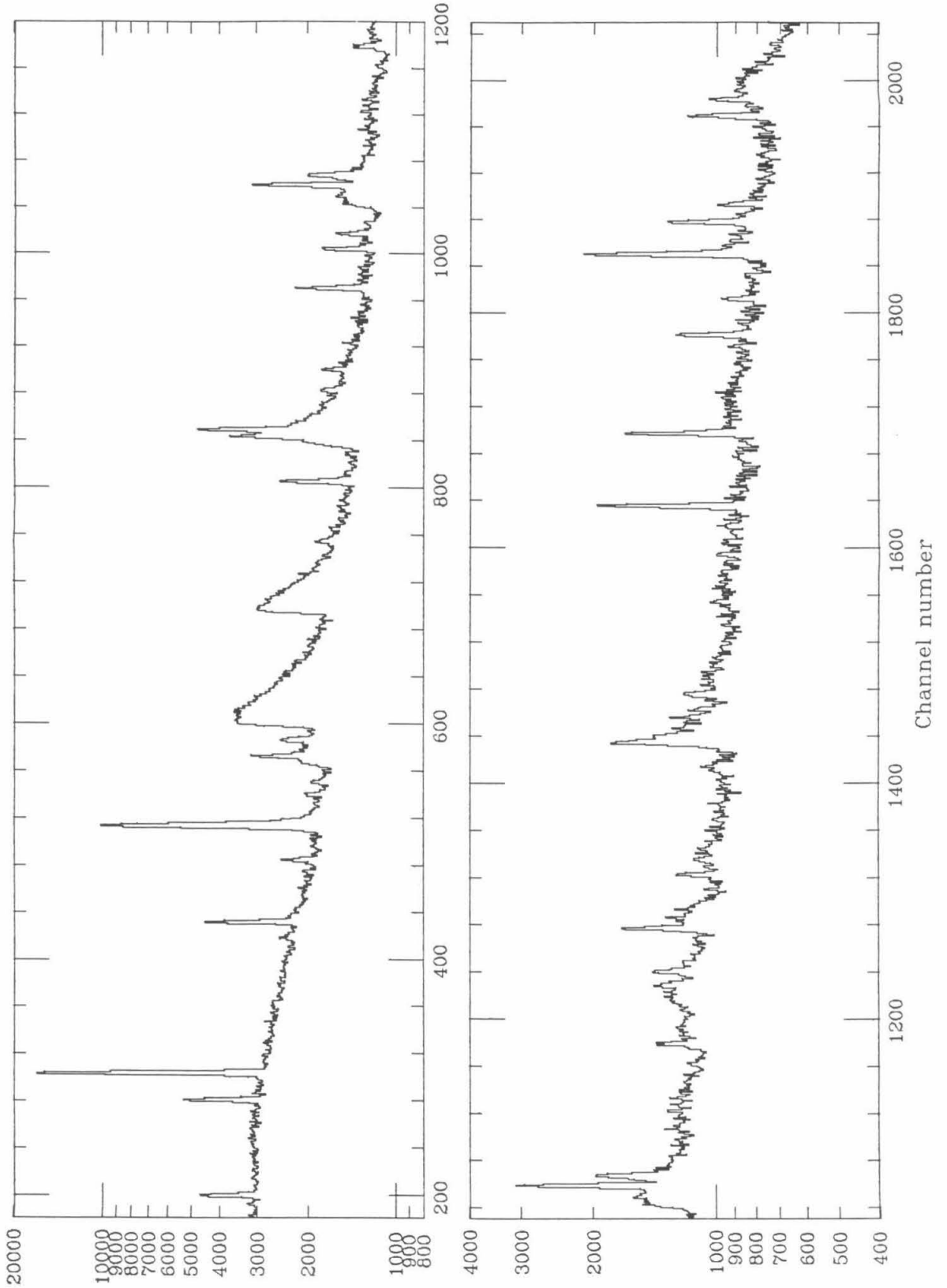
$^{18}O+^{18}O$ γ Spectrum at E_b=20.0 MeV (lab)
Channel number

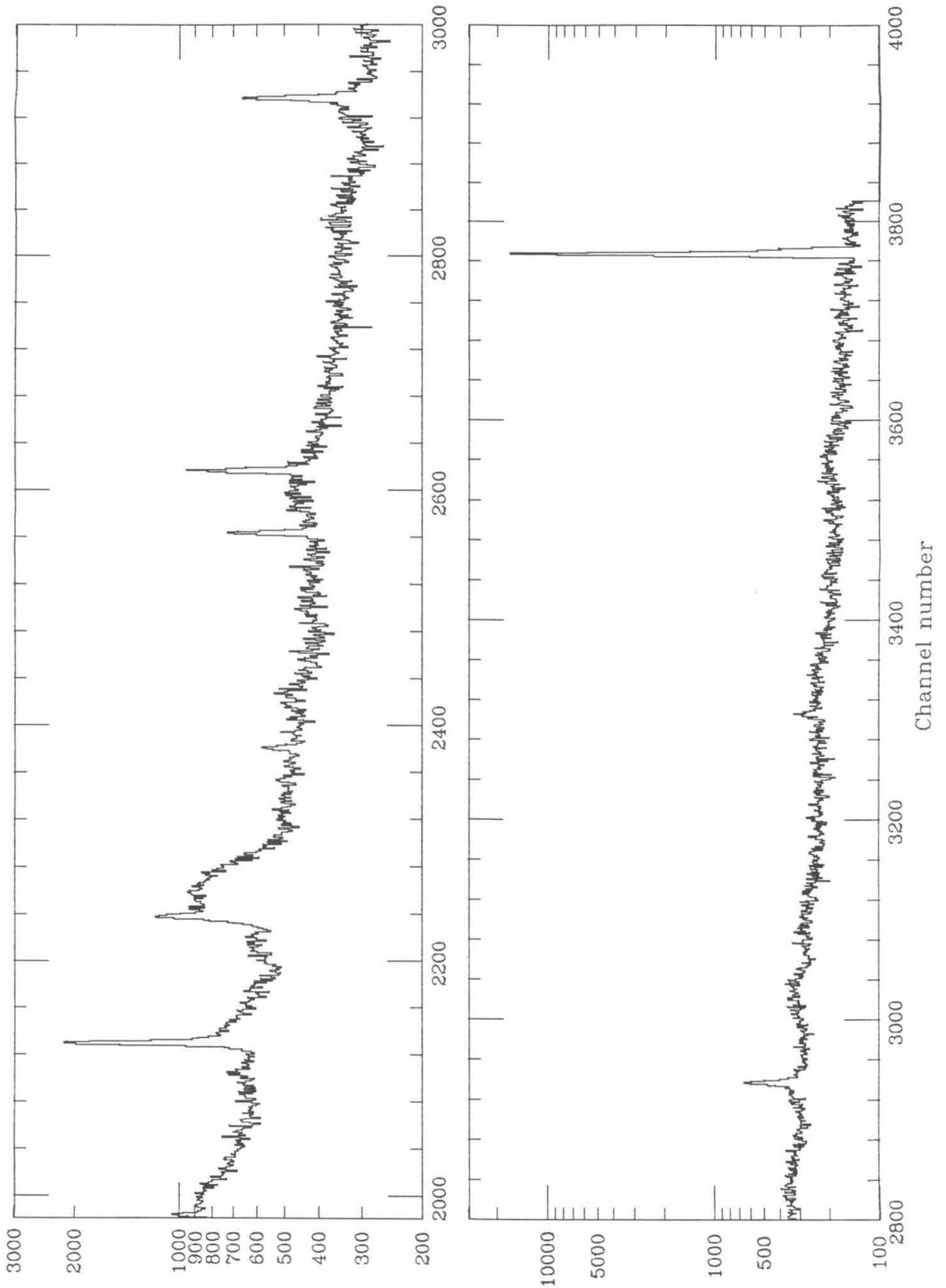
$^{18}O+^{18}O$ γ Spectrum at E_b=20.0 MeV (lab)
Channel number

FIGURE 9

γ–Spectrum of Residual Radioactivity

The residual radioactivity was determined immediately after the beam was turned off. The exit channels with nuclei such as ^{24}Ne, ^{29}Al, and ^{27}Mg were determined in such measurements.

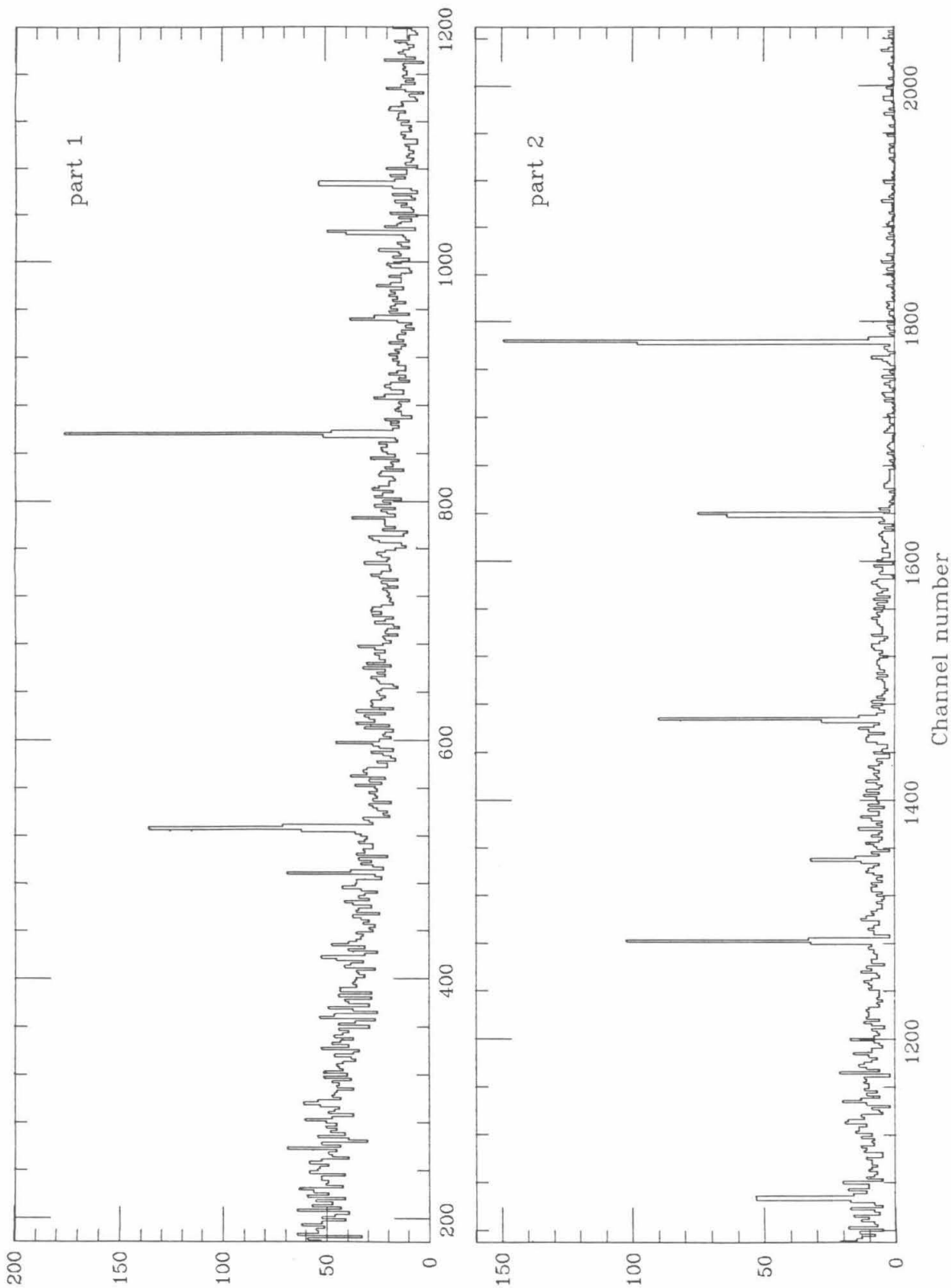
$^{18}O+^{18}O$ Residual γ-Radioactivity
part 1
part 2
Channel number
0
50
100
150
200
400
600
800
1000
1200
1400
1600
1800
2000

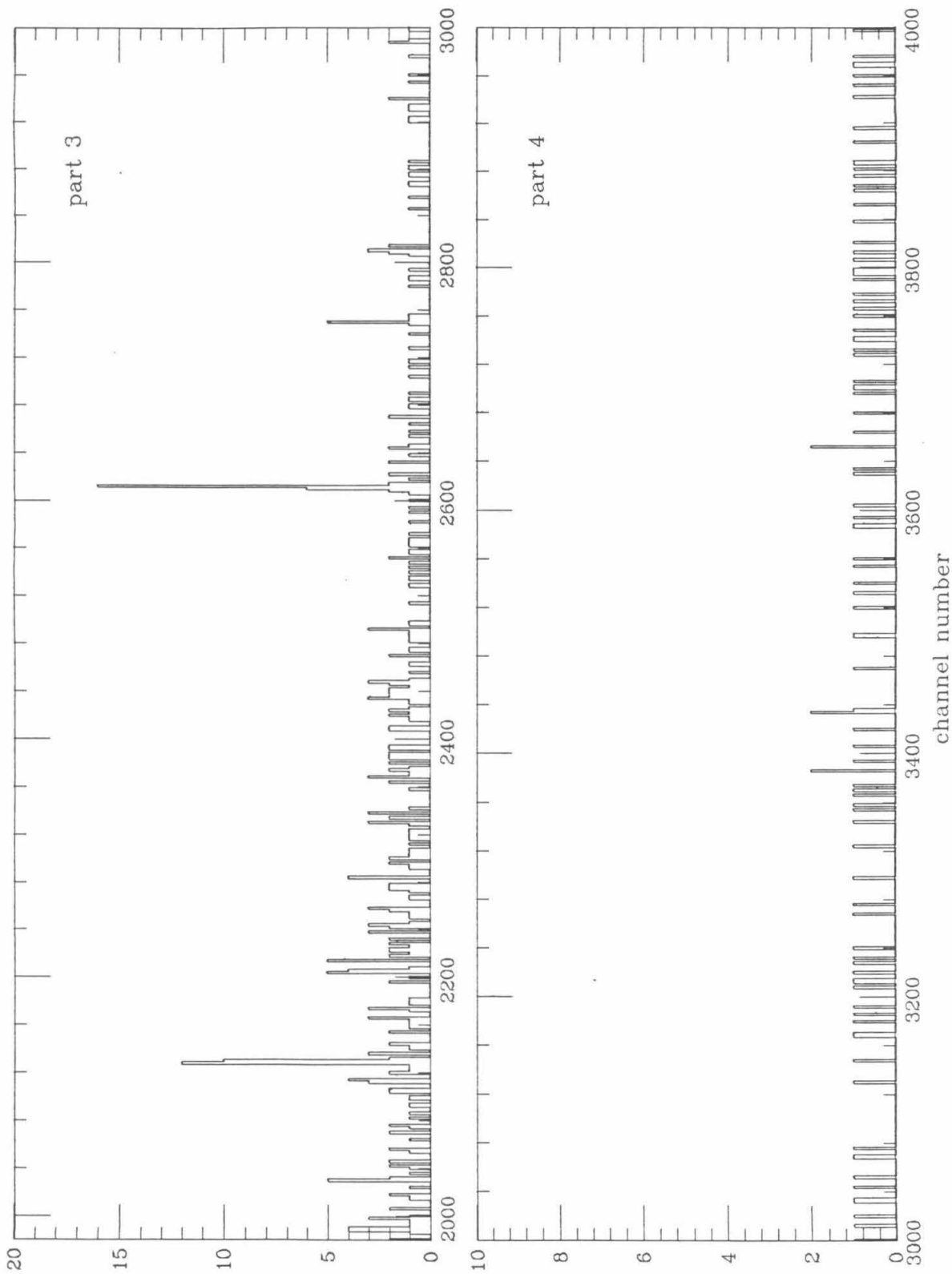
$^{18}O+^{18}O$ Residual γ-Radioactivity
part 3
part 4
channel number

FIGURE 10

Anodizing Apparatus

The chemically etched Ta disk as anode is placed underneath the ^{18}O–enriched water. The cathode is a small tantalum ring. The anode and the cathode are separated by the Lucite container. The base of this anodizing cell is made of stainless steel. The diameter of the anodized area on the Ta disk surface is 20 mm.

ANODIZING APPARATUS

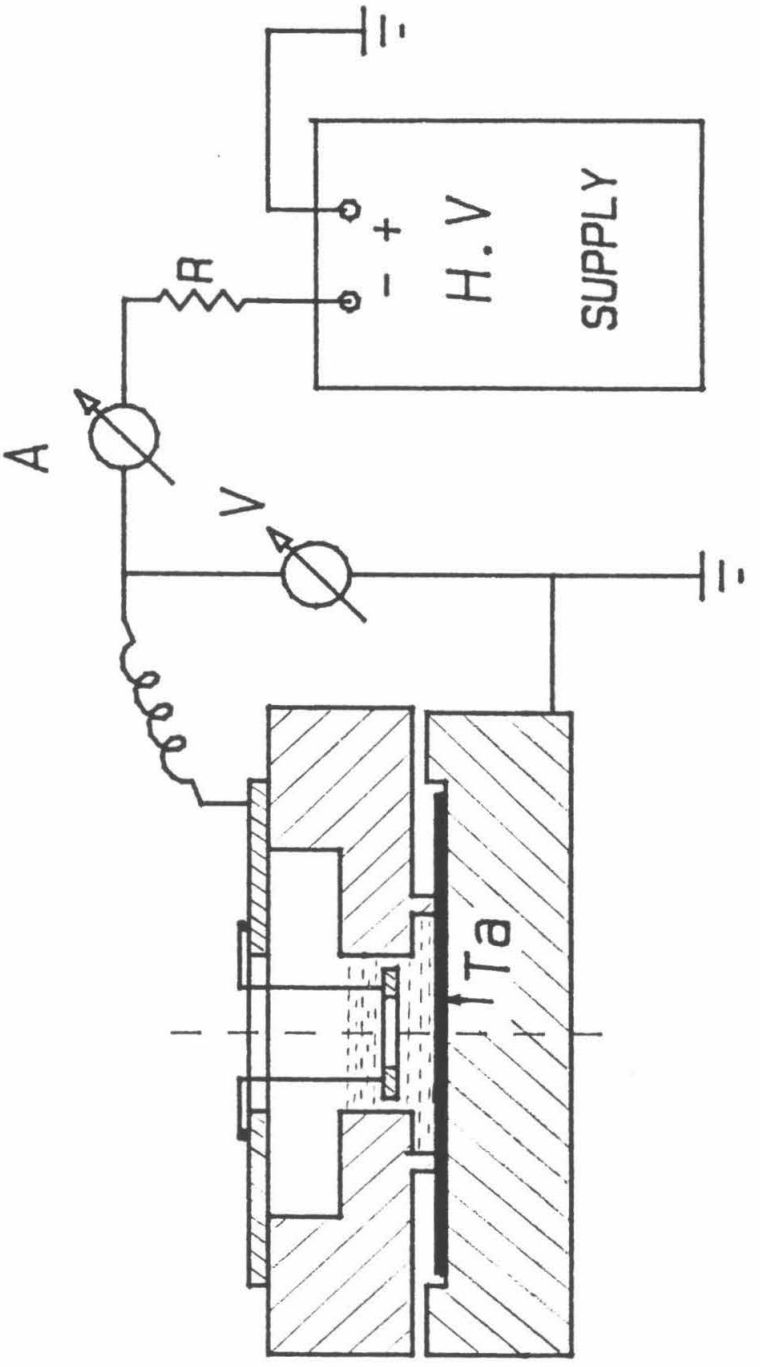

FIGURE 11

$^{16}O + ^{18}O$ γ–Spectrum at Beam Energy 21.33 MeV

This spectrum was recorded with target, detector and target–detector geometry the same as those in the $^{18}O + ^{18}O$ measurement described in fig.8. However, we replaced the ^{18}O beam with an ^{16}O beam of energy 21.33 MeV. This spectrum was used to determine the ^{18}O target thickness, while it also served as a monitor of possible ^{16}O contamination in the ^{18}O target. The fact that the strong 2028 keV γ–ray peak in the $^{16}O + ^{18}O$ spectrum was not found in the $^{18}O + ^{18}O$ spectrum is evidence for the high isotopic purity of the ^{18}O target.

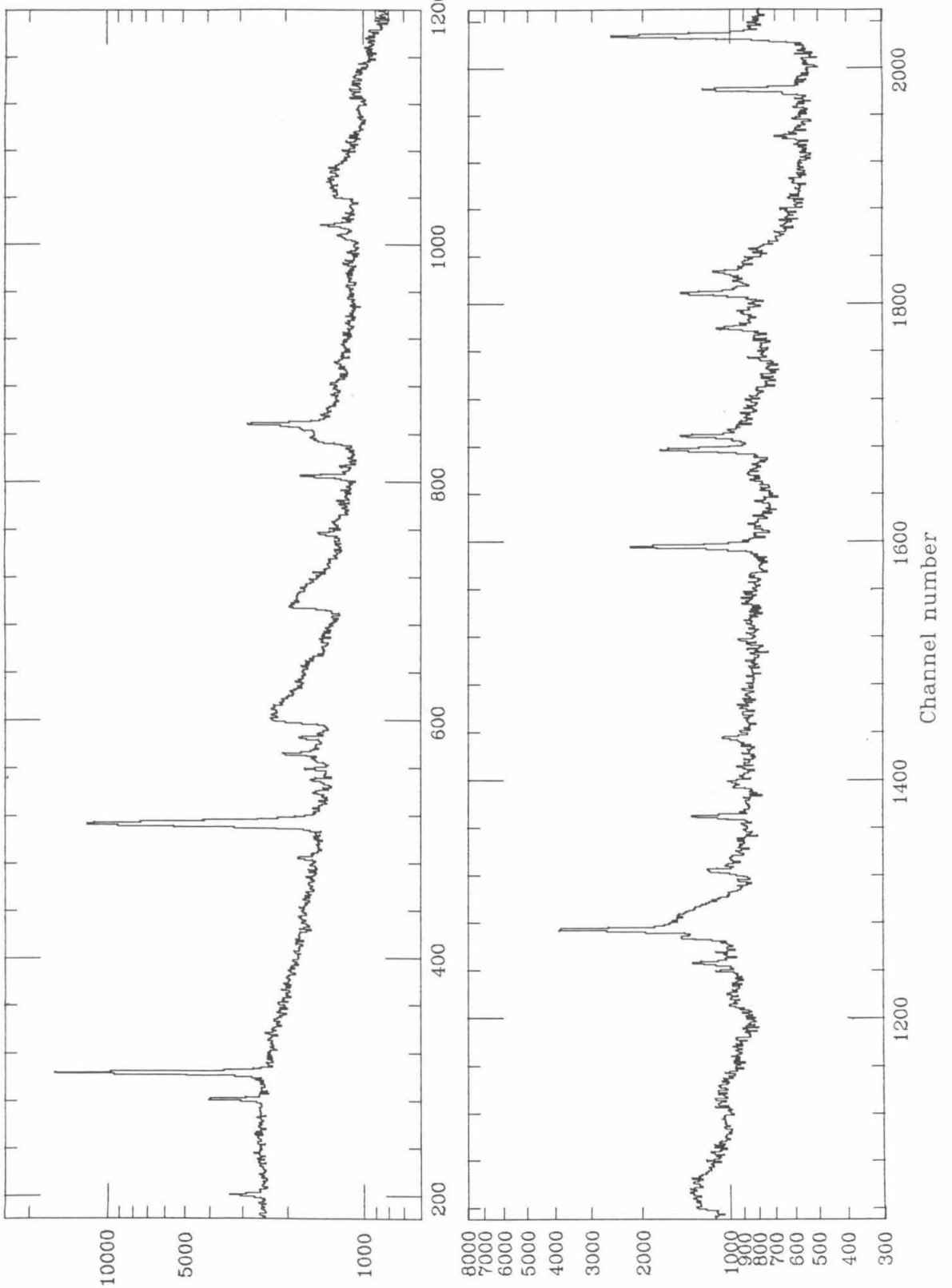
$^{16}O+^{18}O$ γ Spectrum at E_b=21.3 MeV(lab)
Channel number

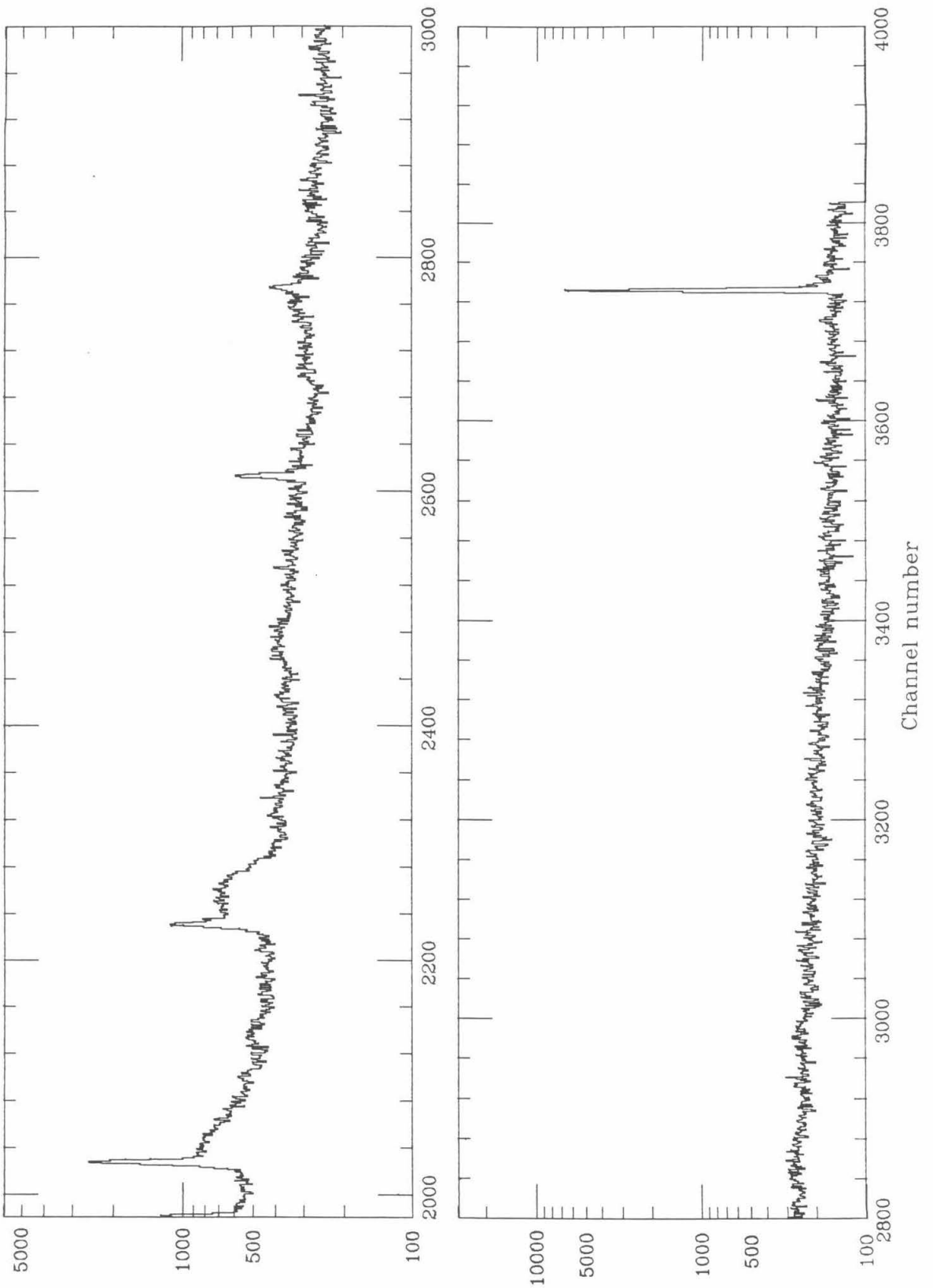
$^{16}O+^{18}O$ γ Spectrum at E_b=21.3 MeV(lab)
5000
1000
500
100
2000
2200
2400
2600
2800
3000
10000
5000
1000
500
100
2800
3000
3200
3400
3600
3800
4000
Channel number

FIGURE 12

α–Backscattering Spectum From WO_3

The experiment was performed in the 24–inch diameter scattering chamber. The beam charge state was 1^+. The α–particle energy was 2.0 MeV. The high peak in the spectrum corresponds to the α backscattering from tungsten nuclei. The plateau–like area represents the scattering from an Al foil, which was used as backing for the WO_3 layer. The small bump on the plateau is the spectrum of α–particles backscattered from the oxygen nuclei in the WO_3 target.

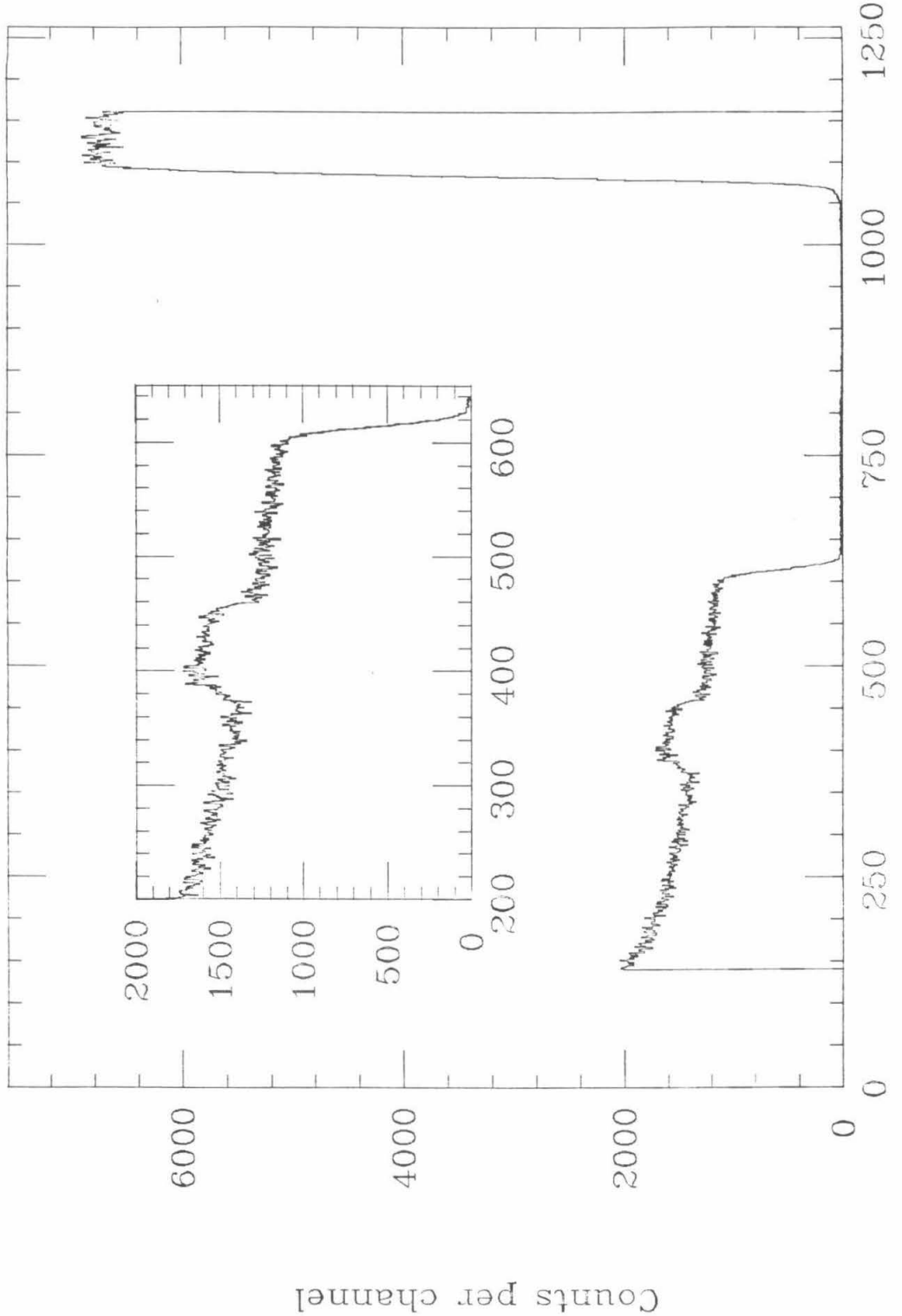
α Backscattering Spectrum from Tungsten Oxide
Counts per channel
Channel number
0
2000
4000
6000
0
250
500
750
1000
1250
0
500
1000
1500
2000
200
300
400
500
600

FIGURE 13

Detector Efficiency

Full–energy–peak efficiencies were determined over the range 276 $keV \leq E_\gamma \leq$ 3300 keV for the Ge detector in the geometry shown in Fig.7. The experimental points are labeled by radioactive nuclide. Full detail are given in section II.C.

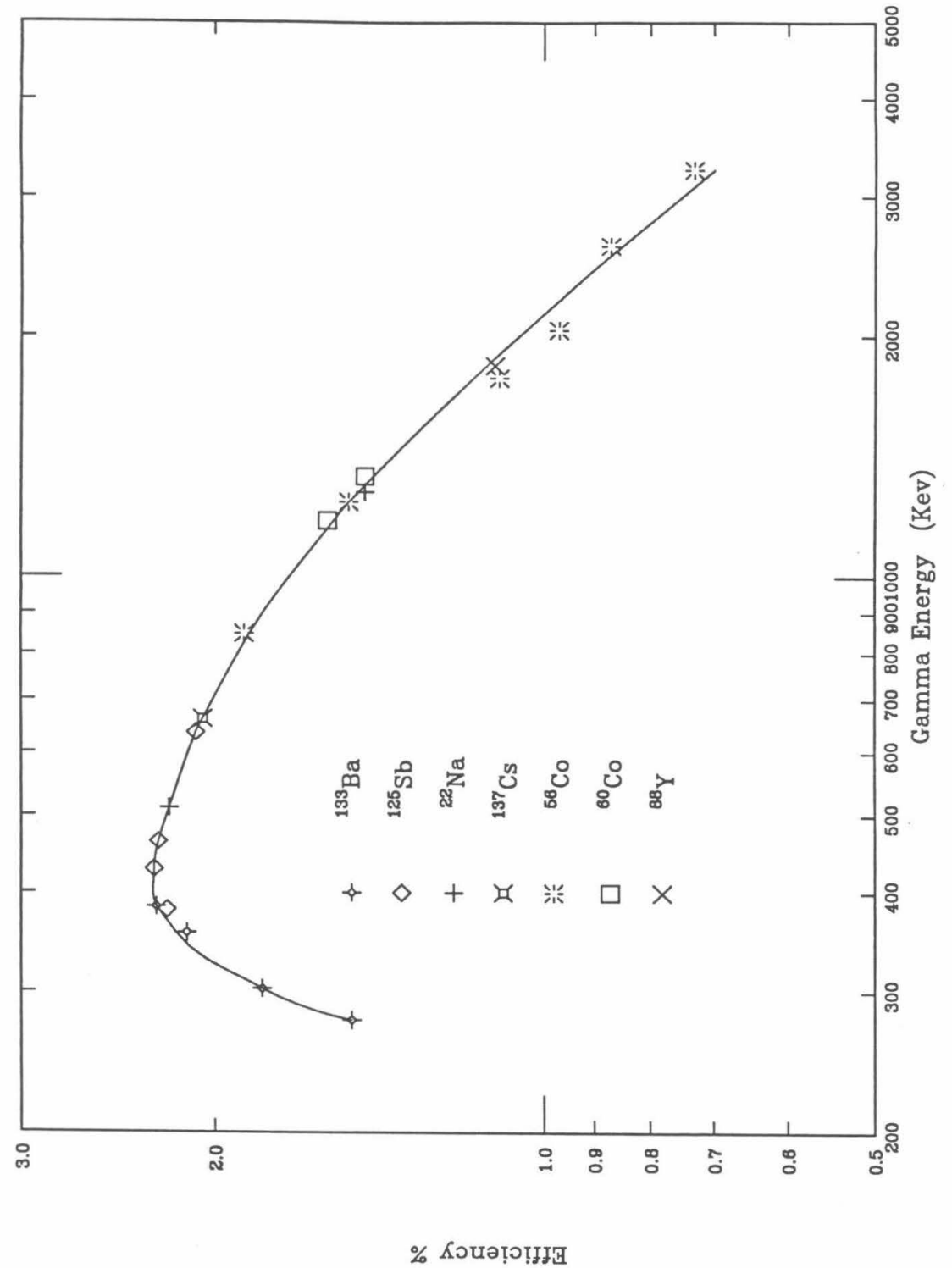
Ge Detector photopeak Efficiency
Efficiency %
Gamma Energy (Kev)
3.0
2.0
1.0
0.9
0.8
0.7
0.6
0.5
200
300
400
500
600
700
800
900
1000
2000
3000
4000
5000
133Ba
125Sb
22Na
137Cs
56Co
60Co
88Y

FIGURE 14

Doppler Effect on the ^{30}Si and ^{34}S γ–spectra

There are two assumptions for the calculation:

1. The residual nucleus initially carries the full momentum of the incident particle in the lab system.

2. The residual nucleus was assumed to be stopped when it lost 98 % of its energy in the target material. (Because dE/dX data for such slow ions are too sparse). The dip in the curves near the low energy peak is an artifact of the calculations arising from this assumption.

The stopping power data dE/dX were taken from (No 70).

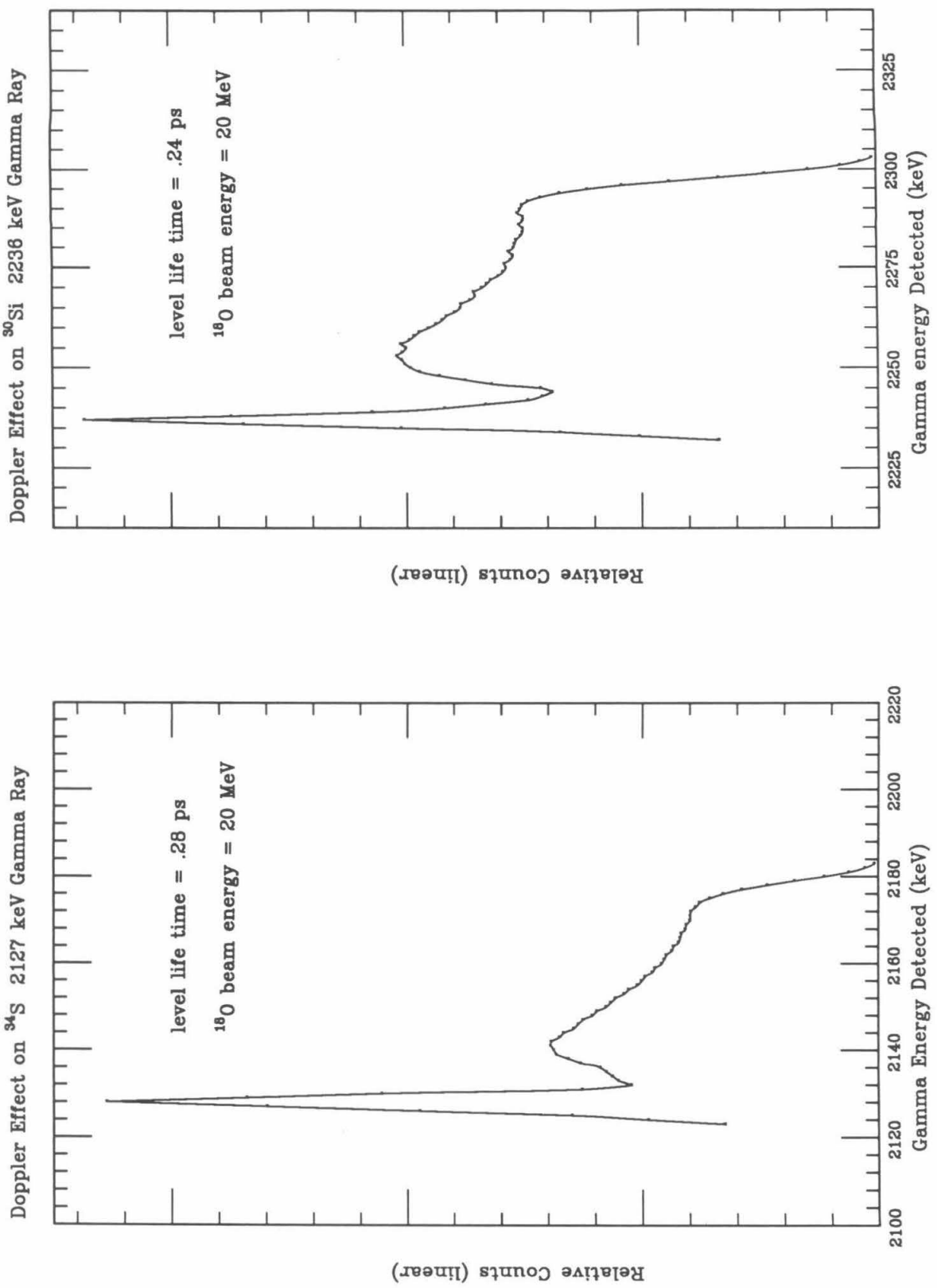
Doppler Effect on ^{30}Si 2236 keV Gamma Ray
level life time = .24 ps
^{18}O beam energy = 20 MeV
Relative Counts (linear)
2225
2250
2275
2300
2325
Gamma energy Detected (keV)
Doppler Effect on ^{34}S 2127 keV Gamma Ray
level life time = .28 ps
^{18}O beam energy = 20 MeV
Relative Counts (linear)
2100
2120
2140
2160
2180
2200
2220
Gamma Energy Detected (keV)

FIGURE 15

Ratio of Cross Sections

The ratio of the ^{34}S production cross sections as determined from the yield of 2127 keV γ–rays to those determined by the yield of 2561 keV γ–rays is plotted as a function of incident energy. Error bars are omitted. The cross sections determined from the two γ–ray measurements agree with one another fairly well, except at the lowest energies.

Another example is the ratio of 2–neutron transfer cross sections, which were determined from the ^{20}F 1057 keV γ–ray and from the ^{20}Ne 1634 keV γ–ray, respectively.

RATIO OF CROSS SECTIONS

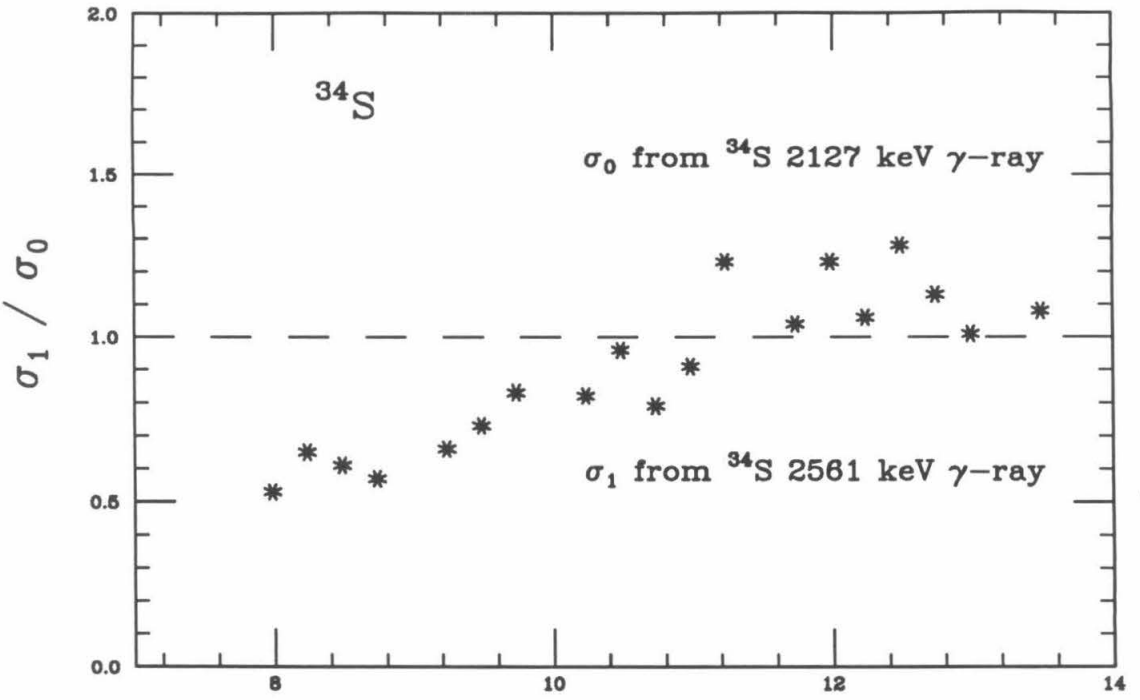

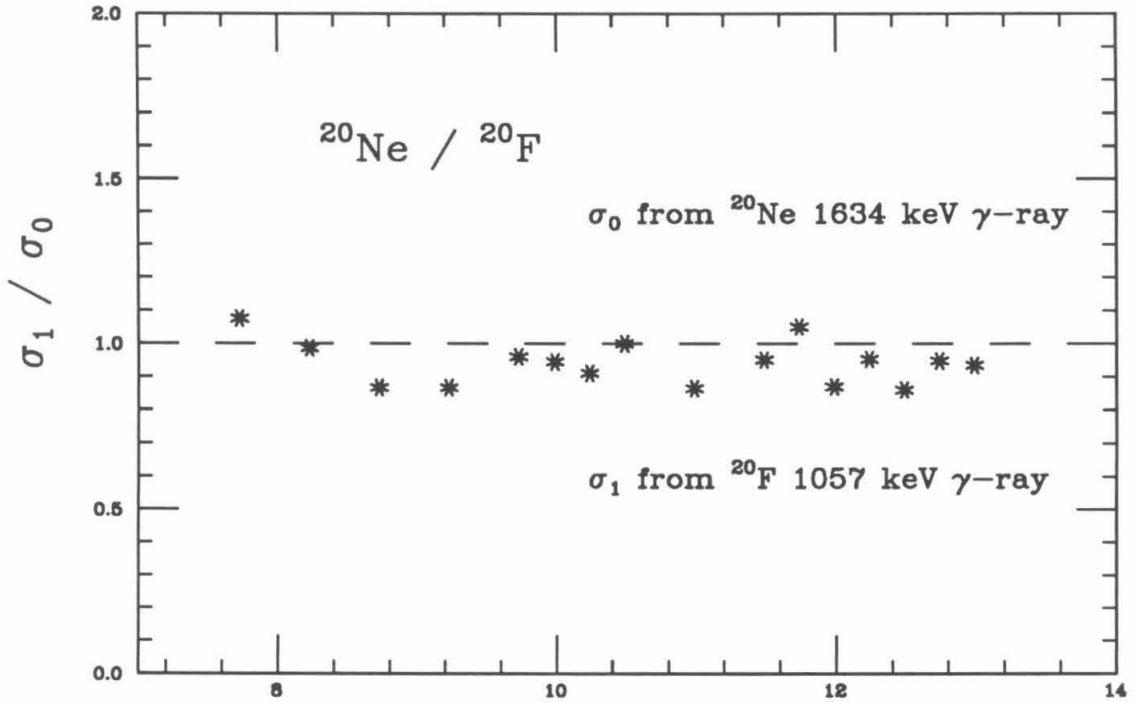

FIGURE 16

0° and 90° γ–Spectra

As described in section III.B, 0° and 90° γ–Spectra at beam energy 20.0 MeV were measured to determine the γ–ray angular distributions for the $^{18}O + {}^{18}O$ reactions. The measurement was performed in a scattering chamber where the vacuum was $10^{-6}\tau$. Carbon buildup is indicated by the large peak at 1779 keV, which comes from the transition of the ^{28}Si 2^+ state to the ground state. ^{28}Si is the main product of $^{12}C + {}^{18}O$. The interferences arising from carbon contamination were considered when we calculated the angular distributions.

The Doppler shifting and broadening effects can be clearly recognized by comparing the two spectra. For more details, see section III.A.

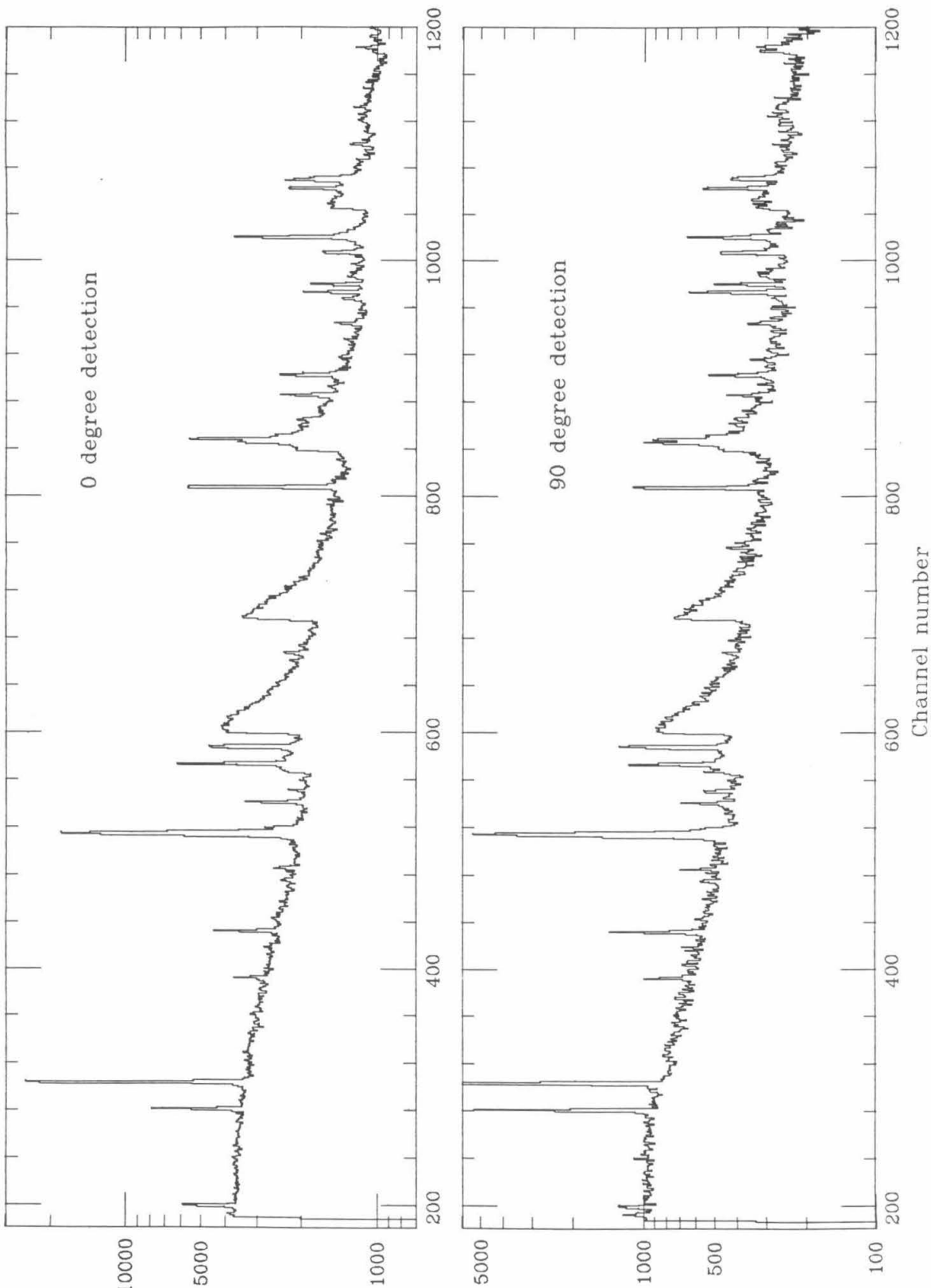
$^{18}O+^{18}O$ γ spectrum at beam energy 20 MeV(lab)
0 degree detection
90 degree detection
Channel number
10000
5000
1000
5000
1000
500
100
200
400
600
800
1000
1200

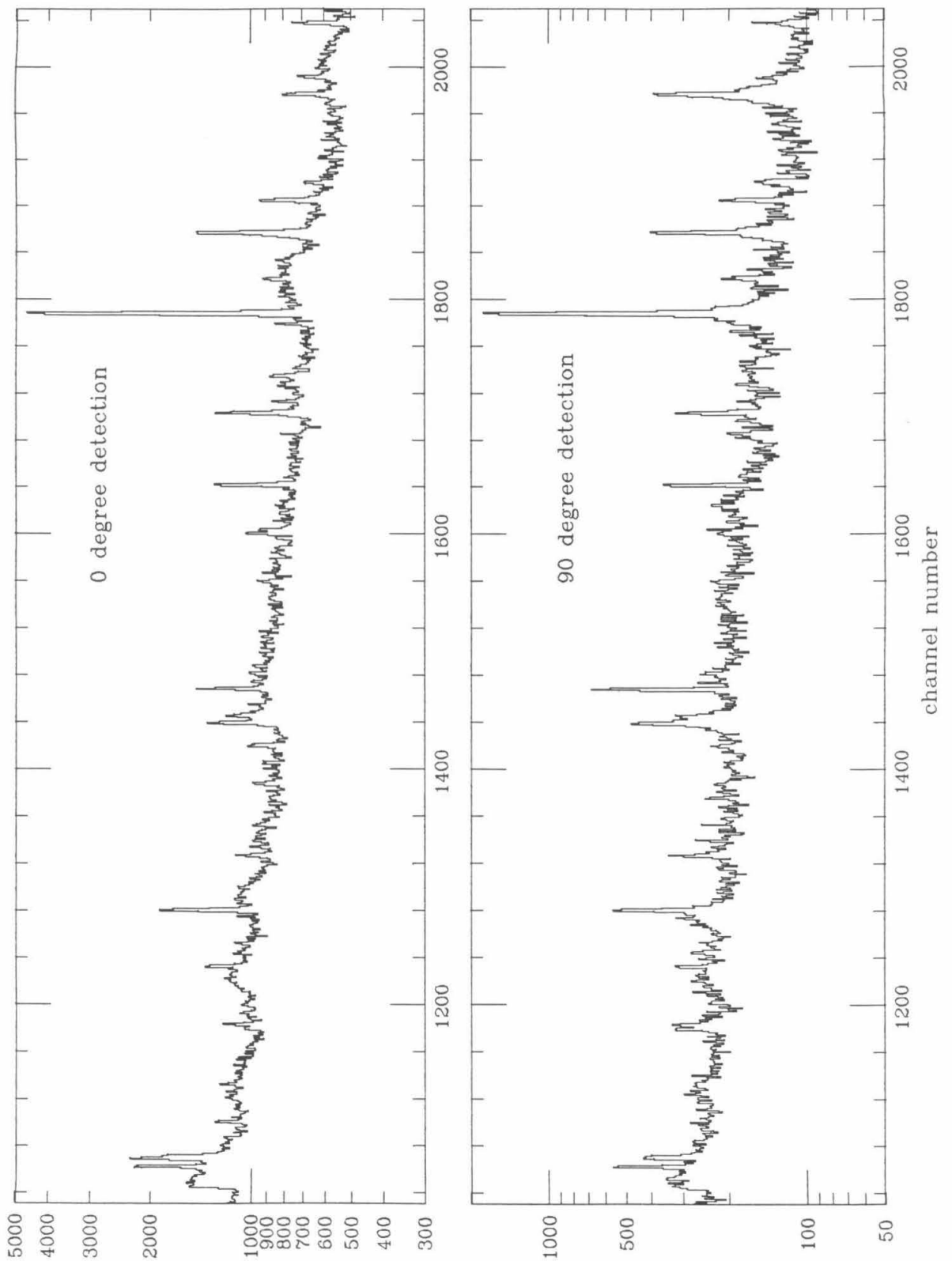
$^{18}O+^{18}O$ γ spectrum at beam energy 20 MeV(lab)
0 degree detection
90 degree detection
channel number
5000
4000
3000
2000
1000
900
800
700
600
500
400
300
1000
500
100
50
1200
1400
1600
1800
2000

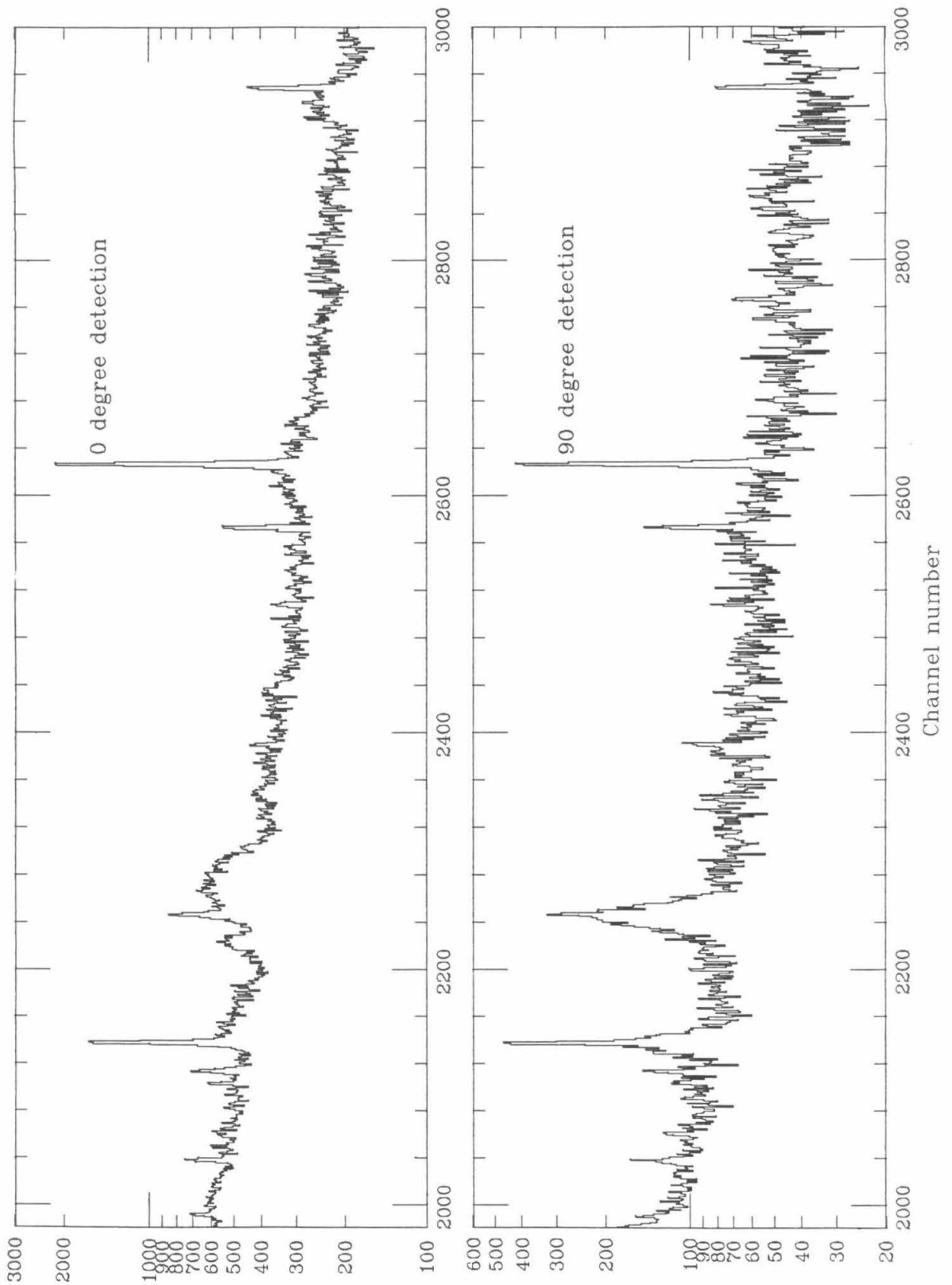
$^{18}O+^{18}O$ γ spectrum at beam energy 20 MeV(lab)
0 degree detection
90 degree detection
Channel number

FIGURE 17

Q–Values Scheme for Exit Channels of $^{18}O + ^{18}O$ Reactions

The Q–Values for all energetically possible exit channels are plotted. The energy region marked by the arrows corresponds to the range of center of mass energies covered by the present measurements.

Q–Value Scheme for Exit Channels of $^{18}O + ^{18}O$ Reactions

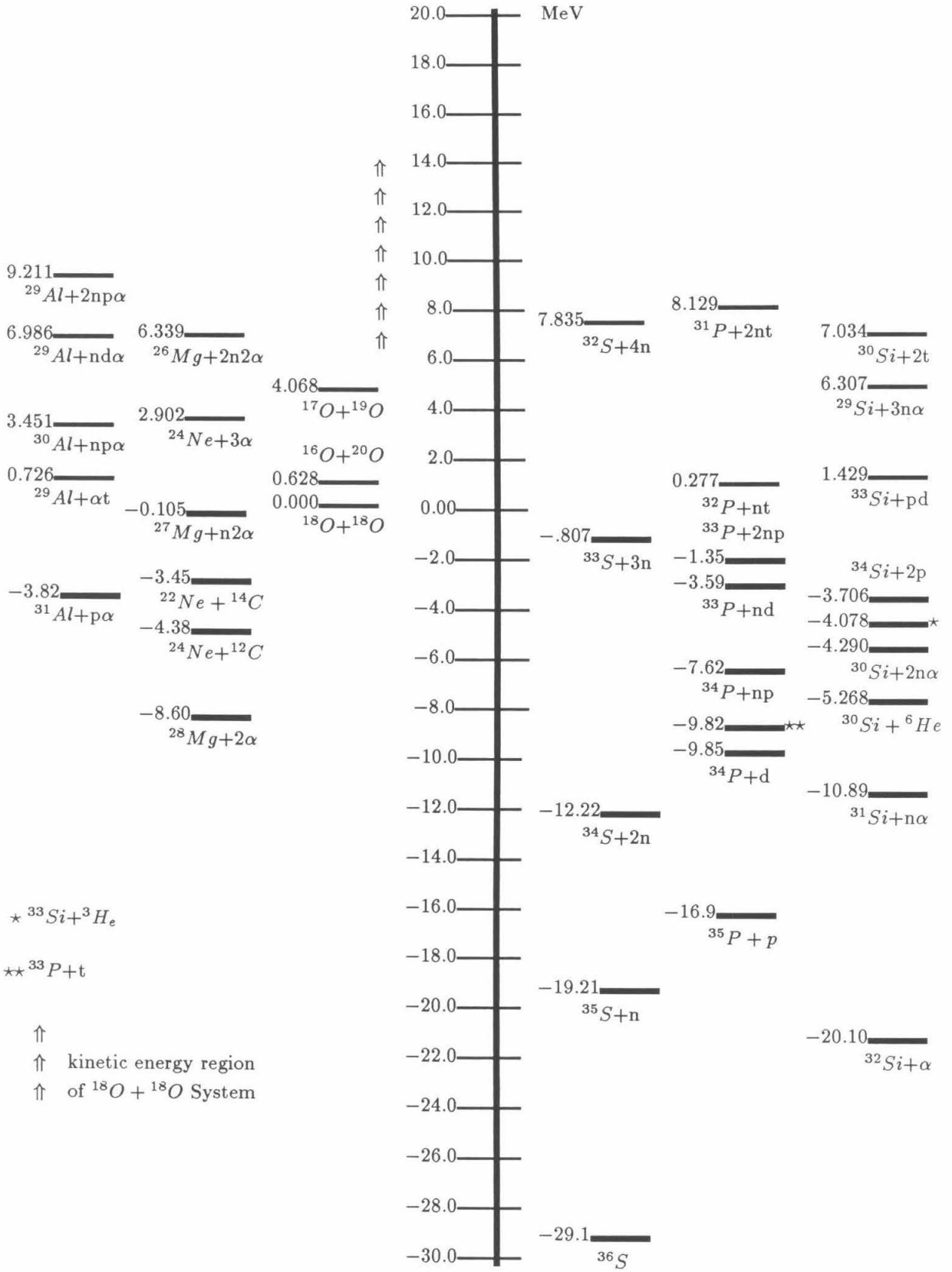

FIGURE 18

Decay Process Leading to Production of ^{30}Si

This is an illustration of the procedure to calculate 4–body reaction cross sections with the code Hauser*5.

The J and π are the spin and parity of the compound nucleus. $E_{c.m}$ is the kinetic energy in the incident channel. E_n and l are the neutron energy and orbital angular momentum. E_x, J_x, and π_x are the excitation energy, spin and parity of the residue ^{35}S, respectively. B_n is the neutron binding energy in the compound nucleus. See section IV.A. for details.

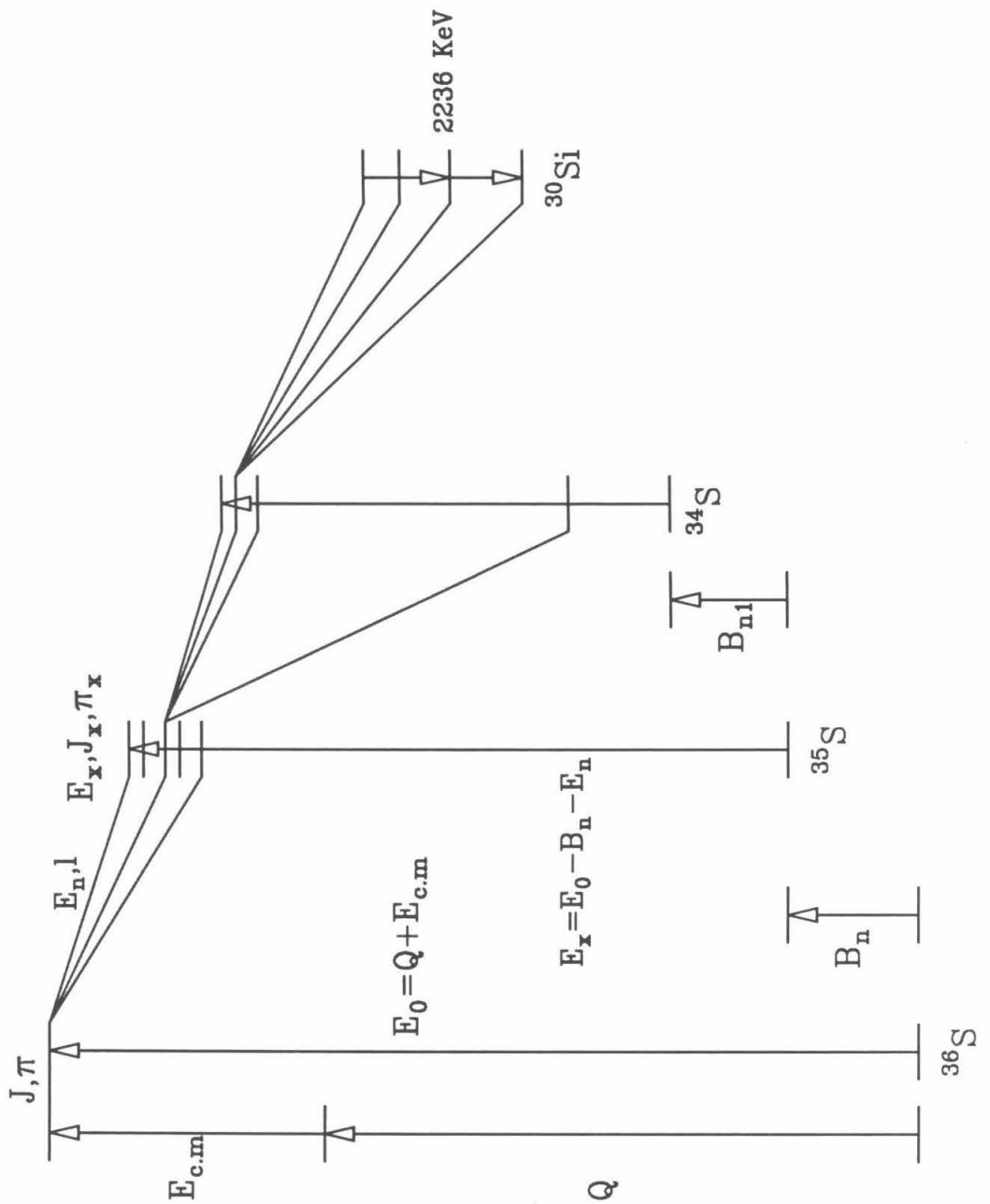
J,π
E_n,l
E_x,J_x,π_x
E_c.m
Q
E_0=Q+E_c.m
E_x=E_0−B_n−E_n
B_n
B_n1
36S
35S
34S
30Si
2236 KeV

FIGURE 19

Hauser–Feshbach Cross Sections

The total fusion cross section and the partial fusion cross sections were computed with Hauser–Feshbach statistical model. The optical potential and level density used in the calculation are given in table 4 and table 6. For details, see IV.B.

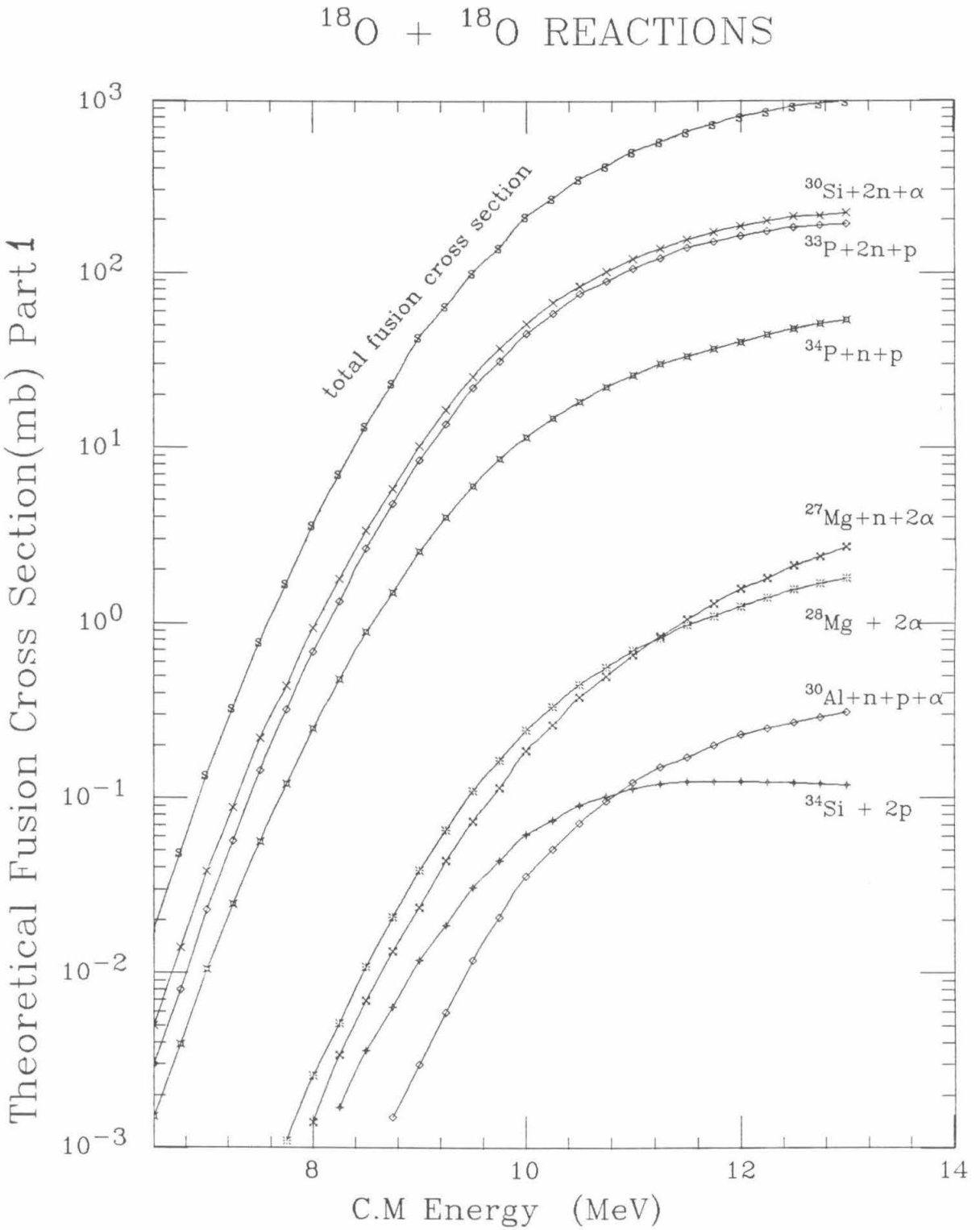
$^{18}O + {}^{18}O$ REACTIONS
Theoretical Fusion Cross Section(mb) Part 1
C.M Energy (MeV)
total fusion cross section
$^{30}Si+2n+\alpha$
$^{33}P+2n+p$
$^{34}P+n+p$
$^{27}Mg+n+2\alpha$
$^{28}Mg + 2\alpha$
$^{30}Al+n+p+\alpha$
$^{34}Si + 2p$
10^{3}
10^{2}
10^{1}
10^{0}
10^{-1}
10^{-2}
10^{-3}
8
10
12
14

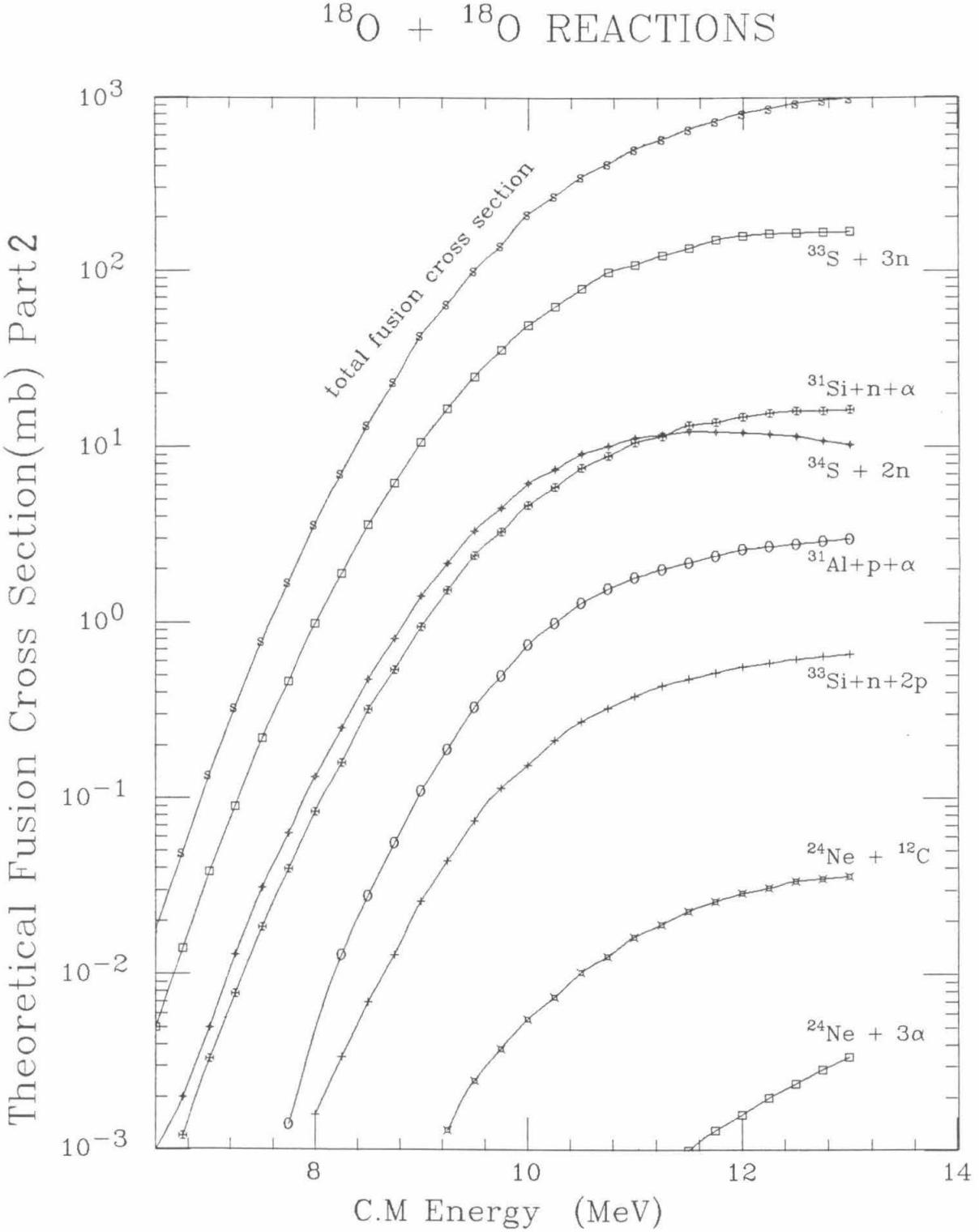
$^{18}O + {}^{18}O$ REACTIONS
Theoretical Fusion Cross Section(mb) Part2
C.M Energy (MeV)
total fusion cross section
$^{33}S + 3n$
$^{31}Si+n+\alpha$
$^{34}S + 2n$
$^{31}Al+p+\alpha$
$^{33}Si+n+2p$
$^{24}Ne + {}^{12}C$
$^{24}Ne + 3\alpha$
10^3
10^2
10^1
10^0
10^{-1}
10^{-2}
10^{-3}
8
10
12
14

FIGURE 20

The Spectra of n, p, d and α

The cross sections for productions of n, p, d and α–particles, which were emitted from compound nuclei, are calculated with Hauser*5. These data are plotted in the figure. It was found that the average energies do not increase strongly with the increasing incident energies. For beam energy from $E_{01} = 14MeV$ to $E_{11} = 26MeV$, (in lab system), the average energies are:

Neutron average energy = 3.7 MeV to 4.0 MeV

Proton average energy = 5.5 MeV to 5.9 MeV

Deuteron average energy = 4.8 MeV to 5.4 MeV

Alpha average energy = 7.7 MeV to 8.0 MeV

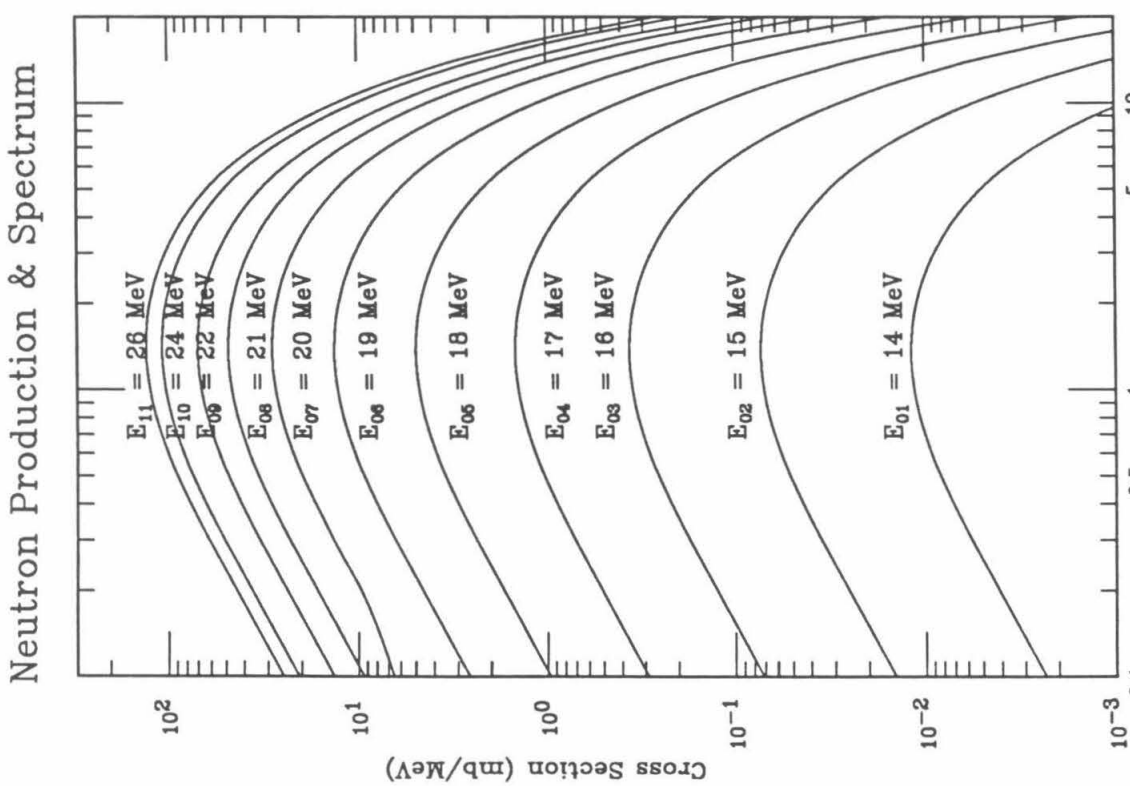
Neutron Production & Spectrum
Cross Section (mb/MeV)
Neutron Energy (MeV)
E_{11} = 26 MeV
E_{10} = 24 MeV
E_{09} = 22 MeV
E_{08} = 21 MeV
E_{07} = 20 MeV
E_{06} = 19 MeV
E_{05} = 18 MeV
E_{04} = 17 MeV
E_{03} = 16 MeV
E_{02} = 15 MeV
E_{01} = 14 MeV
10^{2}
10^{1}
10^{0}
10^{-1}
10^{-2}
10^{-3}
0.1
0.5
1
5
10

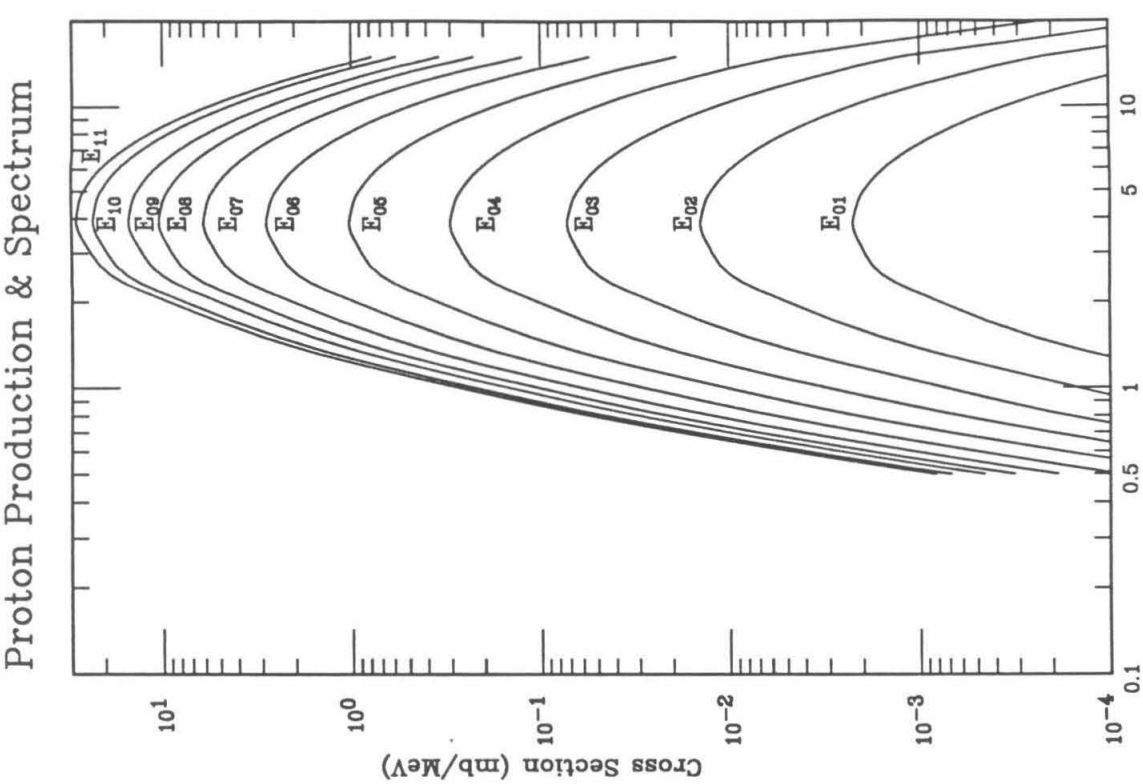
Proton Production & Spectrum
Cross Section (mb/MeV)
Proton Energy (MeV)
E_{11}
E_{10}
E_{09}
E_{08}
E_{07}
E_{06}
E_{05}
E_{04}
E_{03}
E_{02}
E_{01}
10^{1}
10^{0}
10^{-1}
10^{-2}
10^{-3}
10^{-4}
0.1
0.5
1
5
10

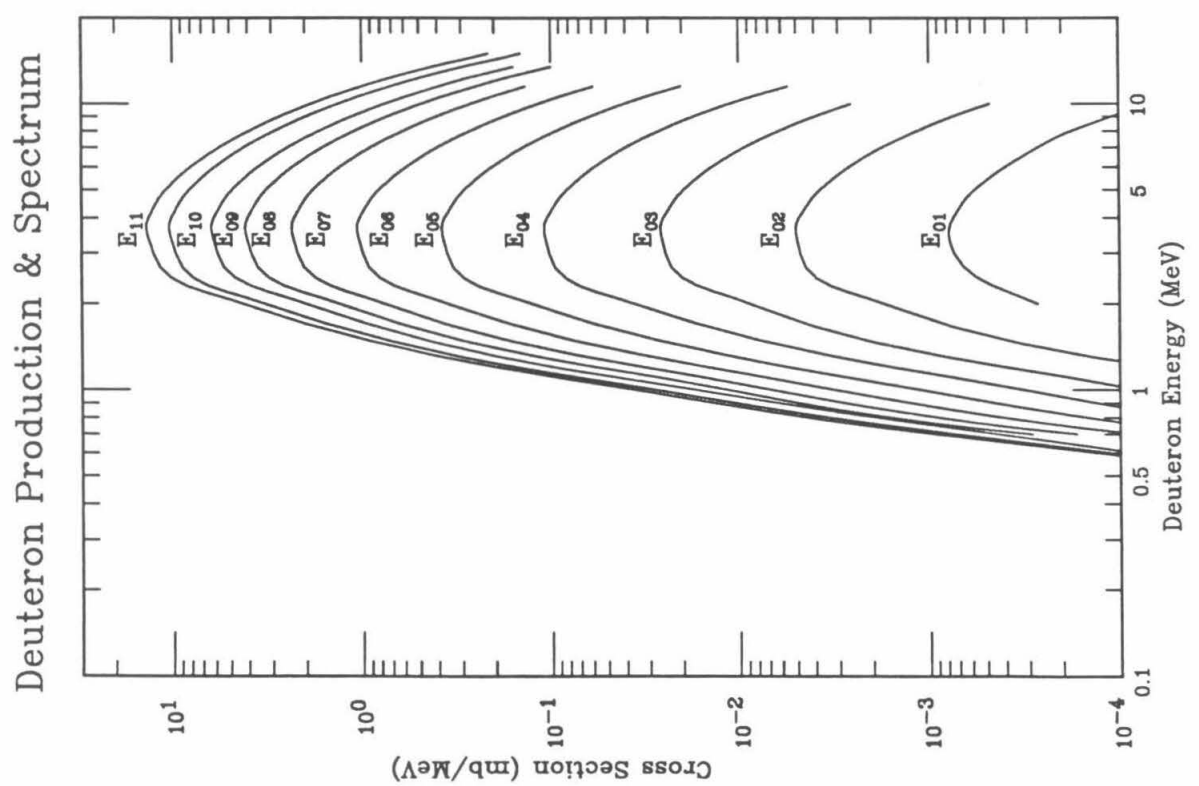
Deuteron Production & Spectrum
Cross Section (mb/MeV)
Deuteron Energy (MeV)
E_{11}
E_{10}
E_{09}
E_{08}
E_{07}
E_{06}
E_{05}
E_{04}
E_{03}
E_{02}
E_{01}
10^{1}
10^{0}
10^{-1}
10^{-2}
10^{-3}
10^{-4}
0.1
0.5
1
5
10

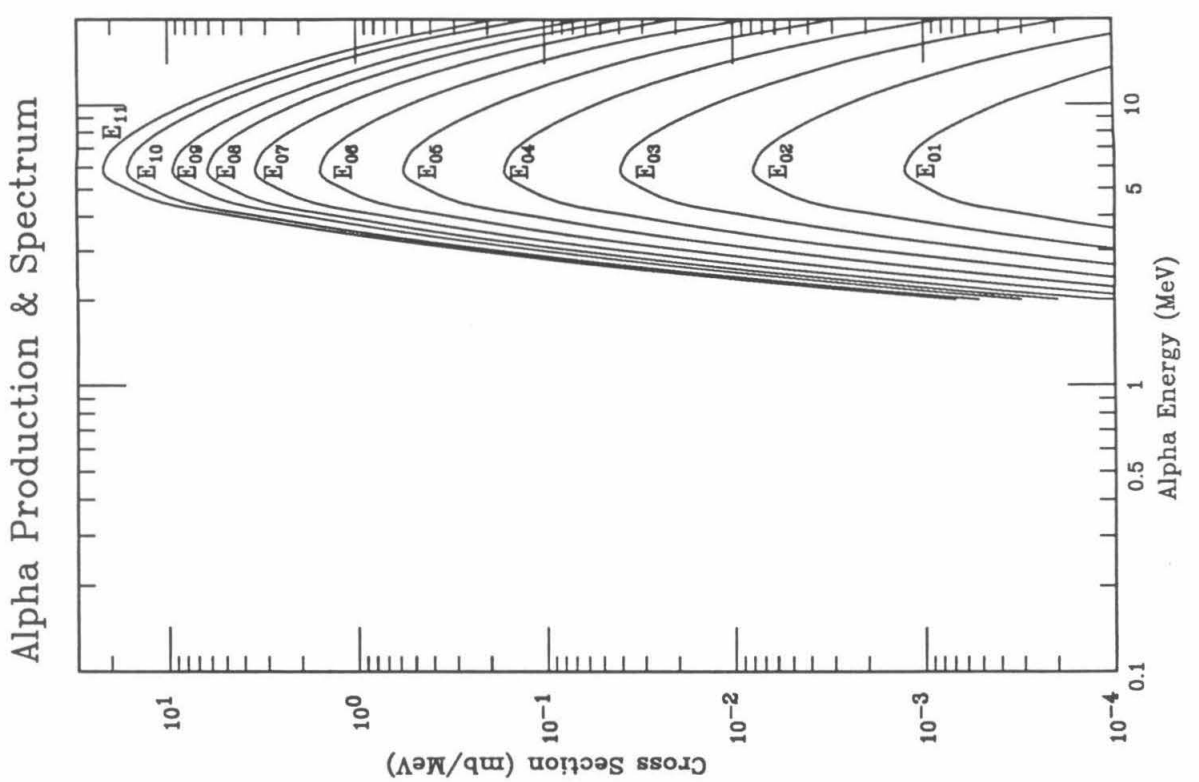
Alpha Production & Spectrum
Cross Section (mb/MeV)
Alpha Energy (MeV)
E_{11}
E_{10}
E_{09}
E_{08}
E_{07}
E_{06}
E_{05}
E_{04}
E_{03}
E_{02}
E_{01}
10^{1}
10^{0}
10^{-1}
10^{-2}
10^{-3}
10^{-4}
0.1
0.5
1
5
10

FIGURE 21

Summing and Branching Factors

Summing and branching correction factors (or β–values) calculated for γ–transitions observed in the $^{18}O + {}^{18}O$ fusion reactions are plotted versus collision energy $E_{c.m.}$ The populations of excited states are obtained from calculations carried out with the Hauser–Feshbach statistical model; the resulting cascade corrections are computed by using published nuclear level diagram (Aj 78), (En 78) and (Le 78). The details are given in section III.C.

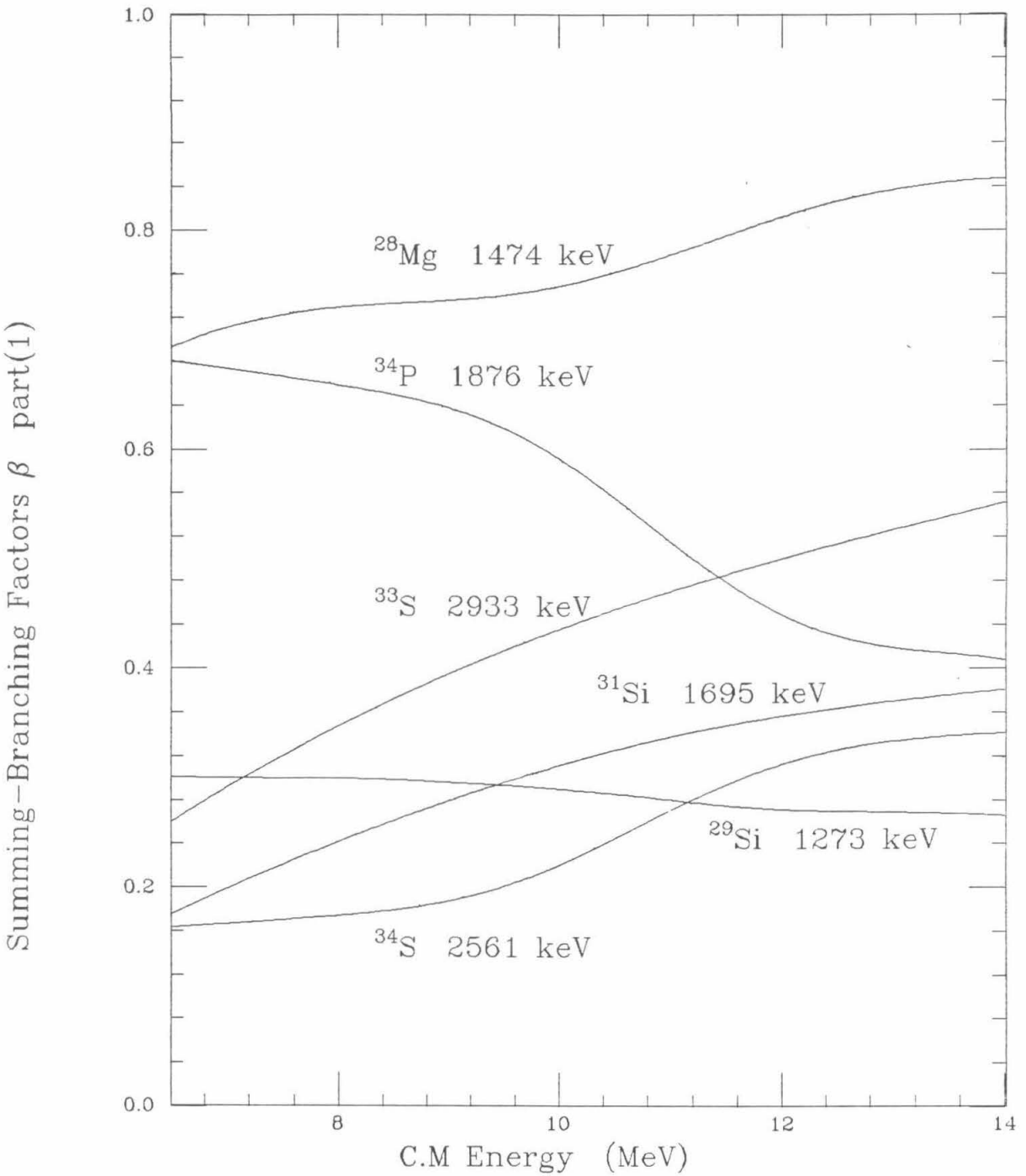
1.0
0.8
0.6
0.4
0.2
0.0
8
10
12
14
C.M Energy (MeV)
Summing-Branching Factors β part(1)
28Mg 1474 keV
34P 1876 keV
33S 2933 keV
31Si 1695 keV
29Si 1273 keV
34S 2561 keV

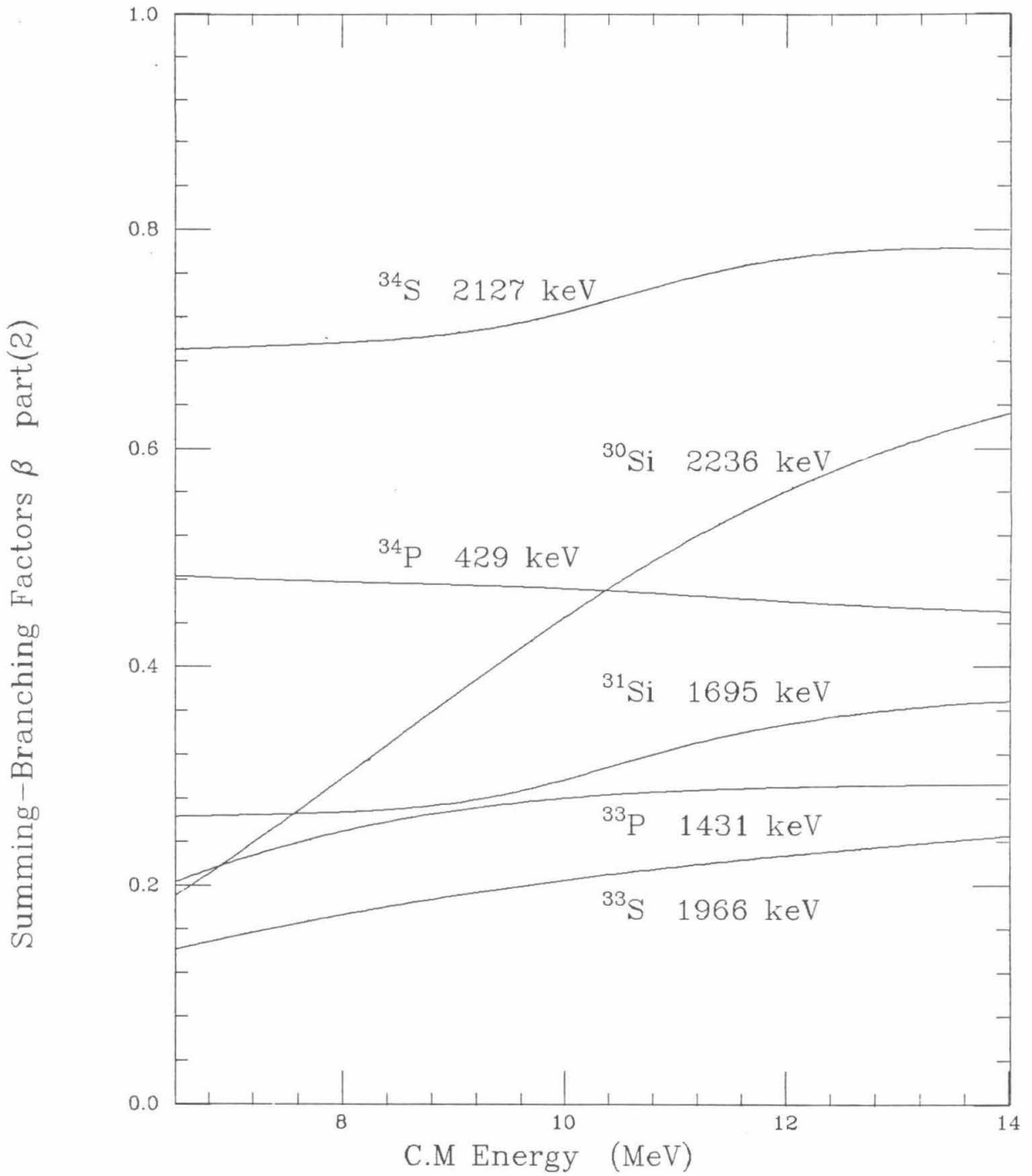
1.0
0.8
0.6
0.4
0.2
0.0
8
10
12
14
C.M Energy (MeV)
Summing-Branching Factors β part(2)
34S 2127 keV
30Si 2236 keV
34P 429 keV
31Si 1695 keV
33P 1431 keV
33S 1966 keV

FIGURE 22

Experimental Cross Sections

The observed cross sections for three different kinds of reactions (fusion, inelastic excitation and transfer reaction) in the $^{18}O + {}^{18}O$ experiment are plotted as functions of incident energy $E_{c.m.}$. The details are given in Chapter IV. (The curve labelled neutron transfer is only for the two–neutron transfer reaction $^{18}O + {}^{18}O \longrightarrow {}^{16}O + {}^{20}O$).

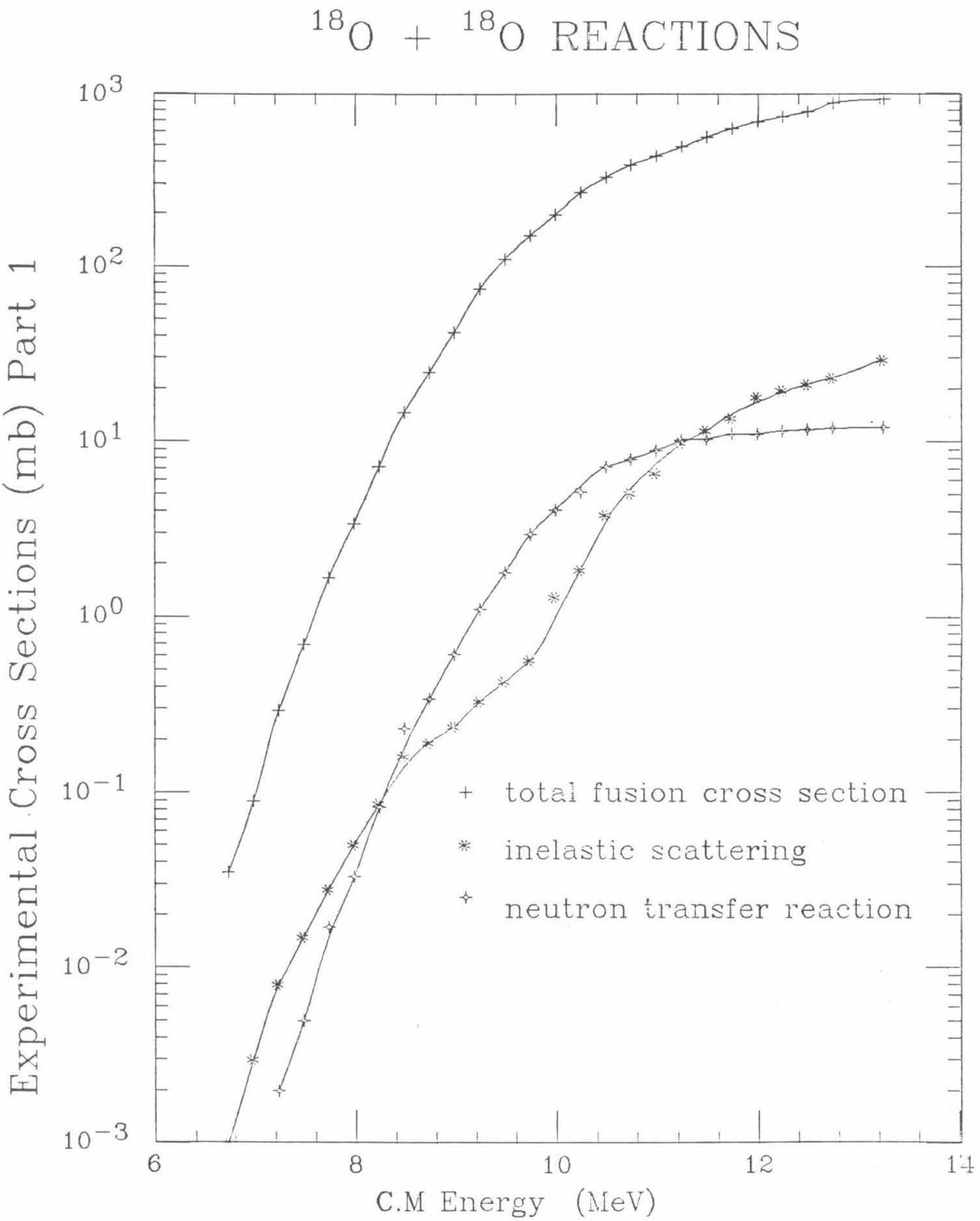
$^{18}O + ^{18}O$ REACTIONS
Experimental Cross Sections (mb) Part 1
10^3
10^2
10^1
10^0
10^{-1}
10^{-2}
10^{-3}
6
8
10
12
14
C.M Energy (MeV)
+ total fusion cross section
* inelastic scattering
neutron transfer reaction

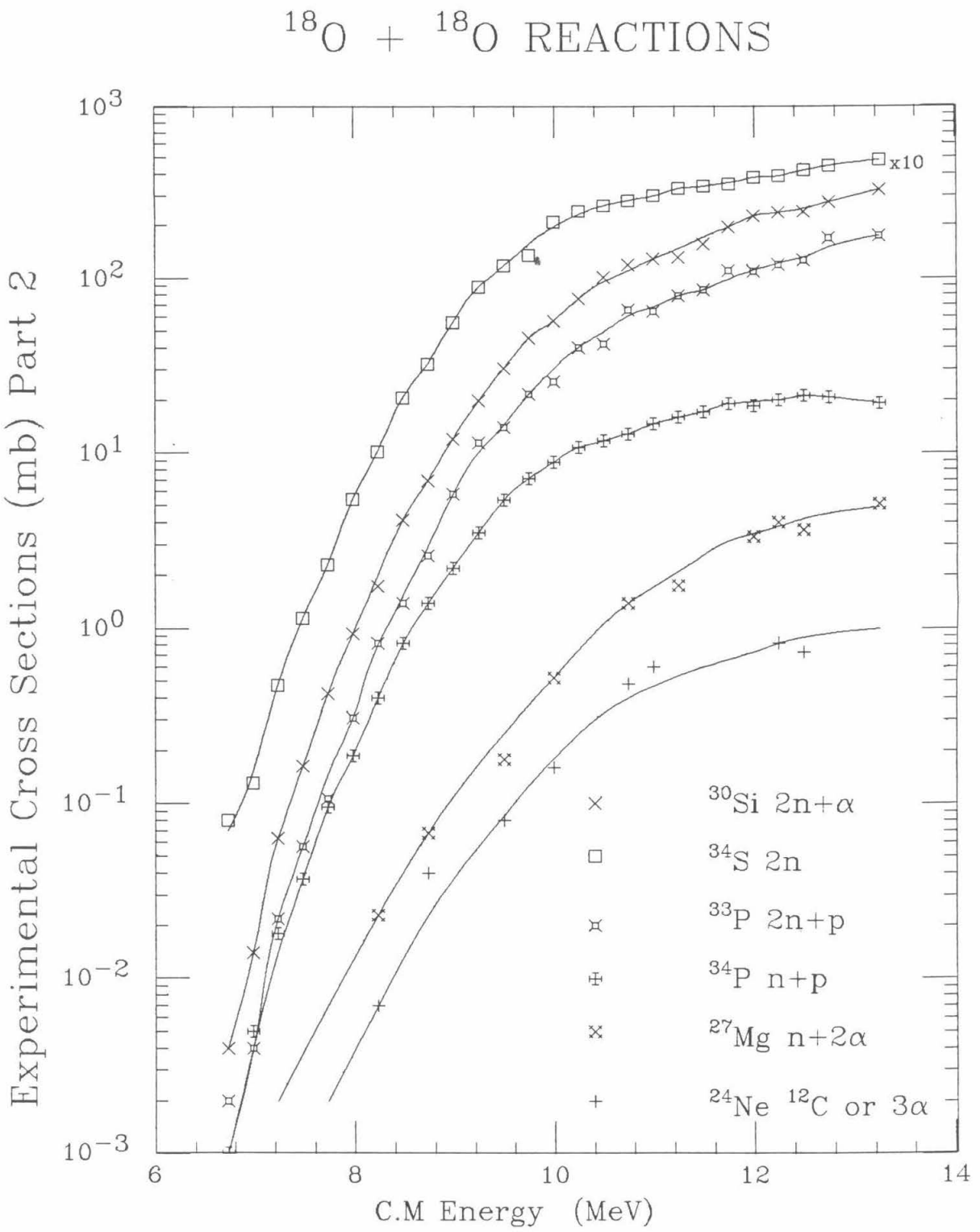
$^{18}O + {}^{18}O$ REACTIONS
Experimental Cross Sections (mb) Part 2
C.M Energy (MeV)
x10
^{30}Si 2n+α
^{34}S 2n
^{33}P 2n+p
^{34}P n+p
^{27}Mg n+2α
^{24}Ne ^{12}C or 3α

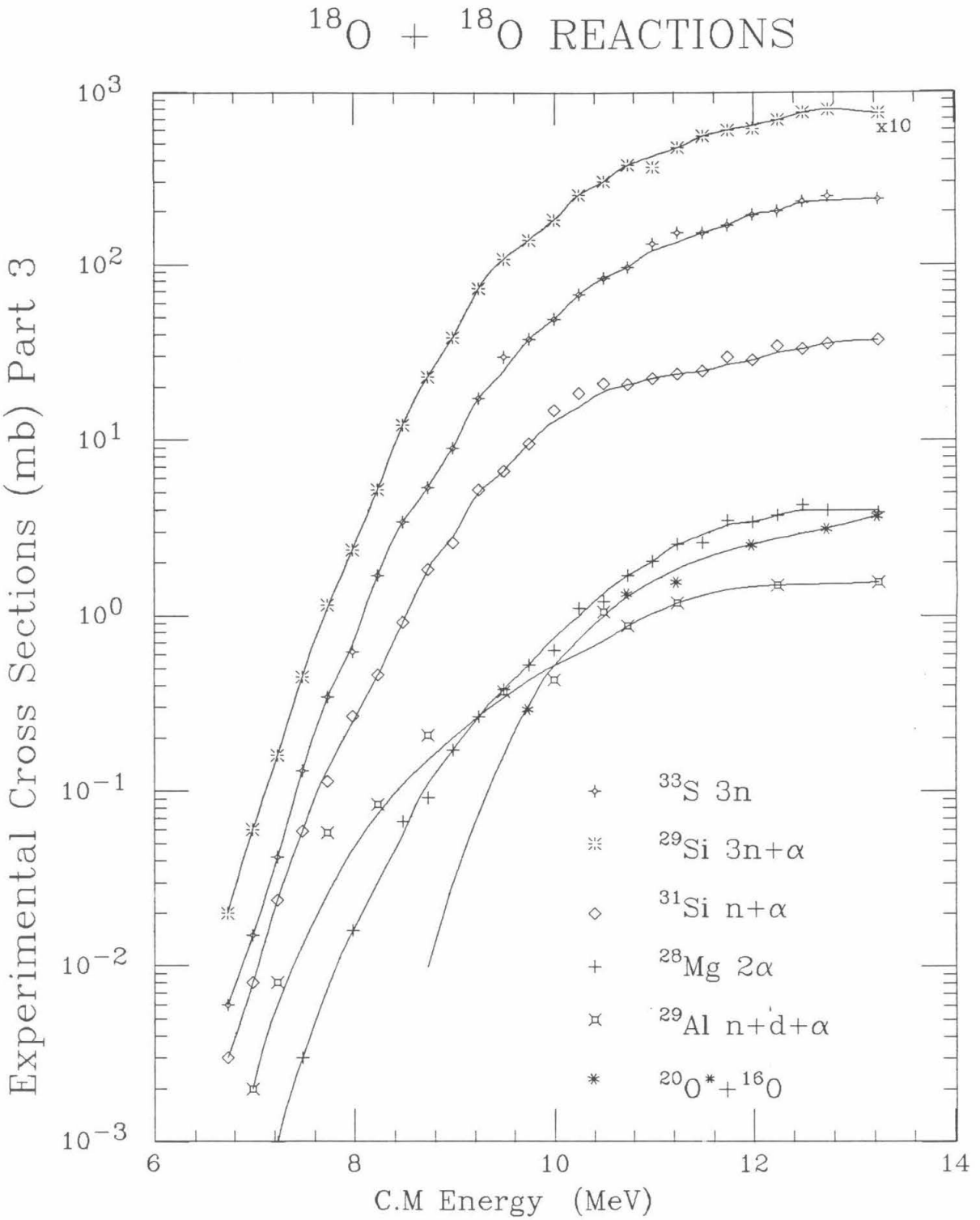
$^{18}O + ^{18}O$ REACTIONS
Experimental Cross Sections (mb) Part 3
C.M Energy (MeV)
x10
^{33}S 3n
^{29}Si 3n+α
^{31}Si n+α
^{28}Mg 2α
^{29}Al n+d+α
$^{20}O^* + ^{16}O$

FIGURE 23

IWBC Fit to Fusion Cross Section

The total fusion cross section of $^{18}O + {}^{18}O$ is compared to model predictions. The points are experimental values and the dotted curve represents the Hauser–Feshbach calculation as in fig.19. The dash curve is the result of an optical model calculation. The solid curve is IWBC fit.

The potentials used to reproduce the total fusion cross section are :

For Hauser–Feshbach Model

V = 100 MeV R_r=6.289 fm a_r=0.51 fm

W_i = 30 MeV R_i=6.813 fm a_i=0.30 fm

For Optical Model

V = 50 MeV R_r=6.289 fm a_r=0.51 fm

W_i = 30 MeV R_i=6.813 fm a_i=0.30 fm

χ^2 per degree of freedom=0.85

For IWBC

V = 100 MeV R_r=6.63 fm a_r=0.51 fm

χ^2 per degree of freedom=0.95

The Woods–Saxon radius R_r=6.63 fm corresponds to the S–wave Coulomb barrier radius R_B=9.225 fm. The definitions of the rest of parameters are the same as in table 6.

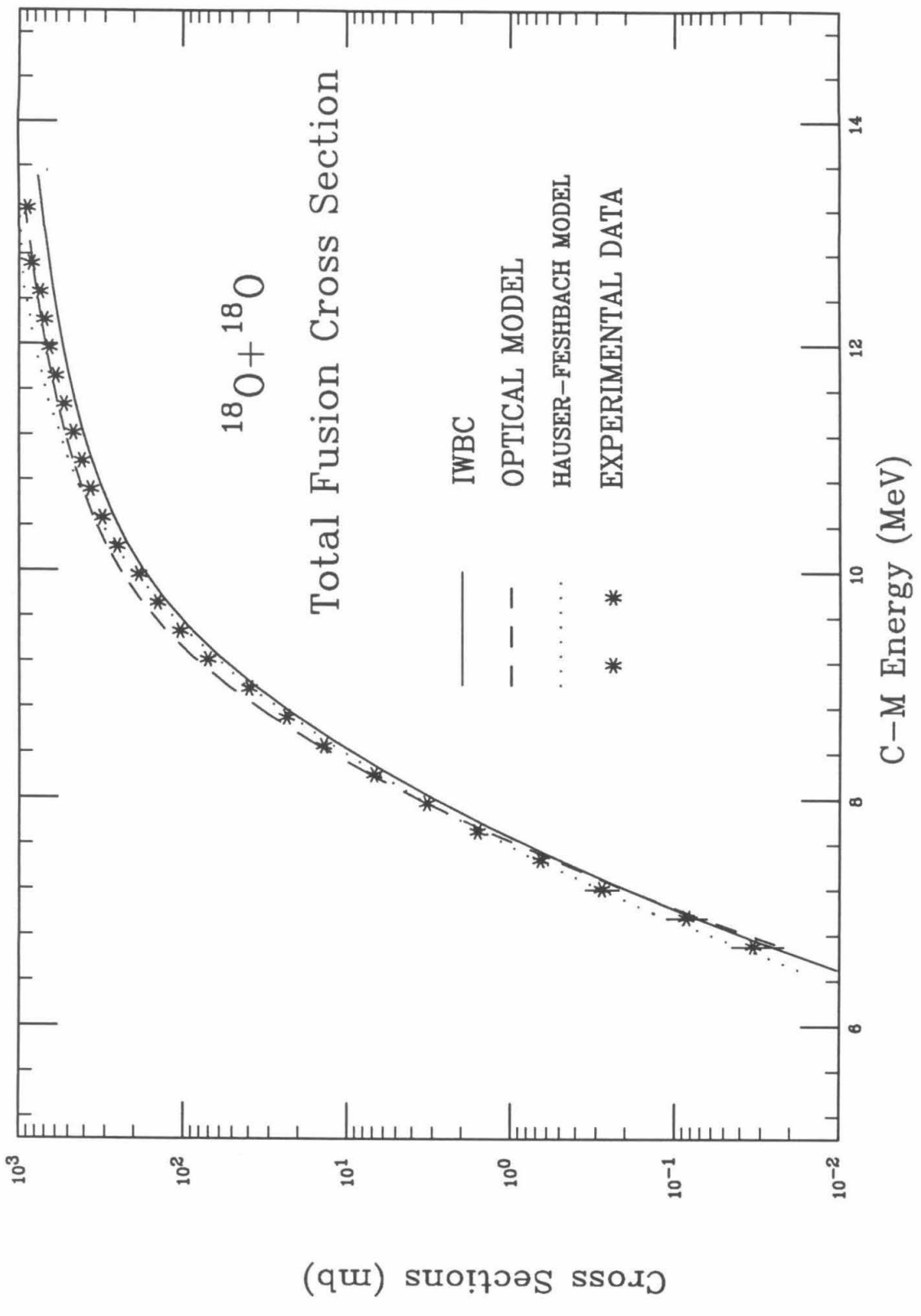
Total Fusion Cross Section
$^{18}O+^{18}O$
IWBC
OPTICAL MODEL
HAUSER-FESHBACH MODEL
EXPERIMENTAL DATA
Cross Sections (mb)
C-M Energy (MeV)
10^{3}
10^{2}
10^{1}
10^{0}
10^{-1}
10^{-2}
6
8
10
12
14

FIGURE 24

IWBC Fit to S–Factor

All the parameters of the potentials used here to fit the S–factor are the same as those employed to fit the total fusion cross section in fig.23. See caption to fig.23.

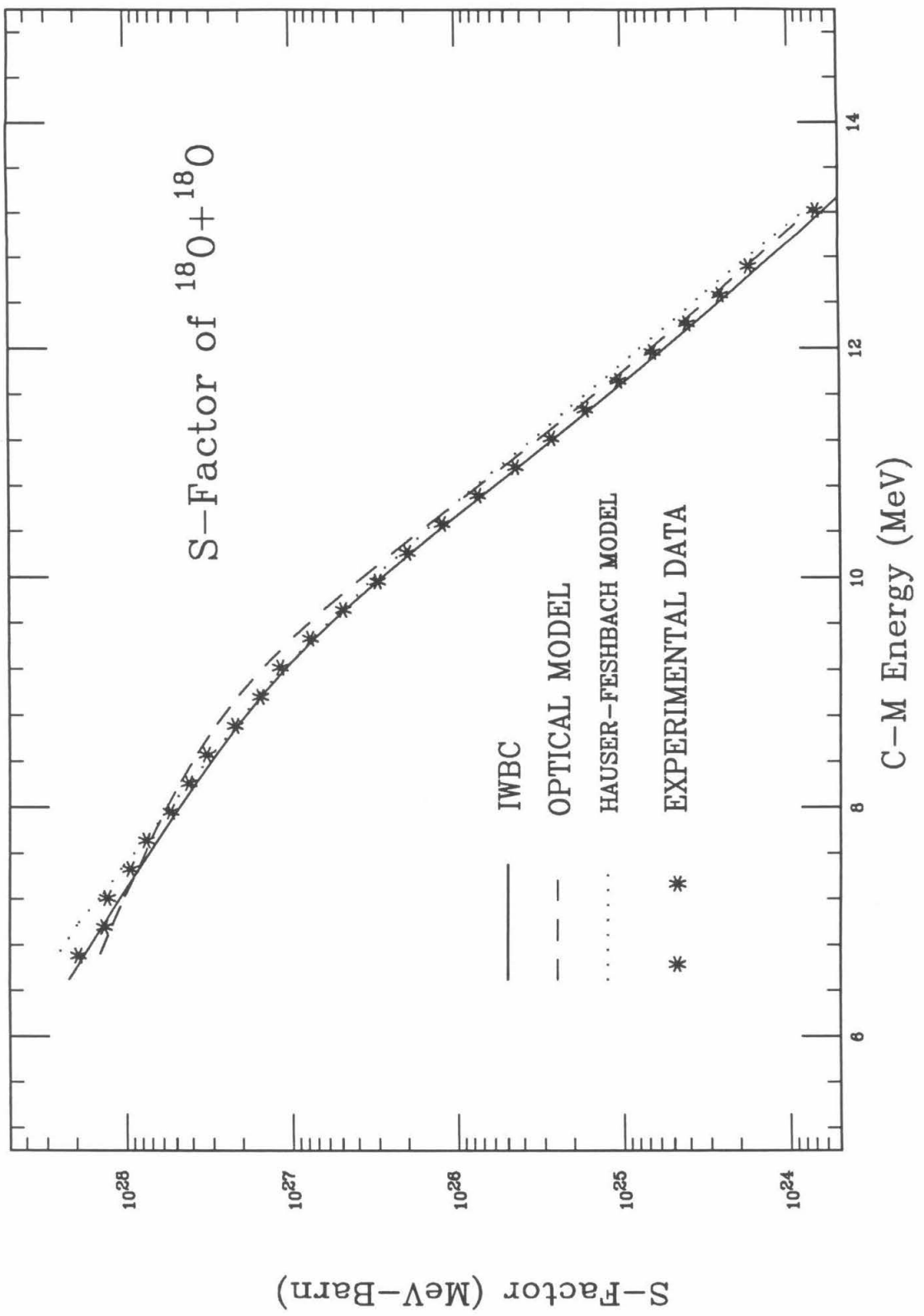
S-Factor of $^{18}O+^{18}O$
IWBC
OPTICAL MODEL
HAUSER-FESHBACH MODEL
EXPERIMENTAL DATA
S-Factor (MeV-Barn)
C-M Energy (MeV)
10^{28}
10^{27}
10^{26}
10^{25}
10^{24}
6
8
10
12
14

FIGURE 25

IWBC Fit to Elastic Scattering Cross Section

The IWBC was used to fit the elastic scattering cross section, obtained from ref.(Ka 77). The solid curve is the original coupled channel calcalation. The potential used in the coupled–channel calculation is the same as that used to calculate fusion reaction cross section with Hauser–Feshbach model (see table 6). The dash curve is our IWBC fit and dot curve is the fit with optical model. The details of the calculations are described in section V.A. The parameters of the potentials which are used in the model calculations are:

For Coupled–Channel calculation

V = 100 MeV R_r=6.289 fm a_r=0.51 fm

W_i = 30 MeV R_i=6.813 fm a_i=0.30 fm

For Optical Model

V = 50 MeV R_r=6.289 fm a_r=0.51 fm

W_i = 30 MeV R_i=6.813 fm a_i=0.30 fm

χ^2 per degree of freedom=0.85

For IWBC

V = 100 MeV R_r=6.63 fm a_r=0.51 fm

χ^2 per degree of freedom=0.95

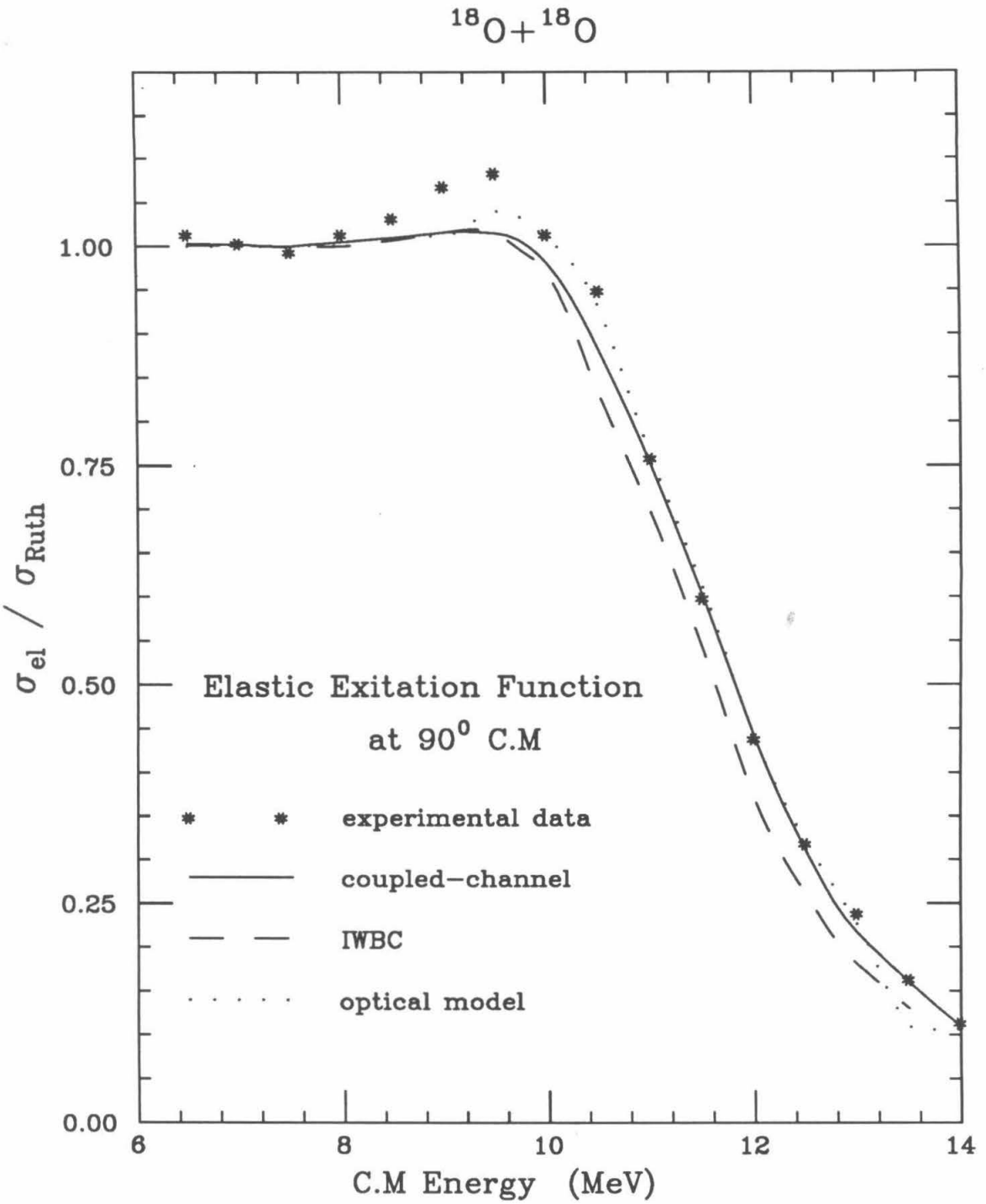
$^{18}O+^{18}O$
1.00
0.75
0.50
0.25
0.00
σ_{el} / σ_{Ruth}
Elastic Exitation Function
at 90^0 C.M
experimental data
coupled−channel
IWBC
optical model
6
8
10
12
14
C.M Energy (MeV)

FIGURE 26

Angular Distribution of Elastic scattering

The experimental angular distribution for $^{18}O + ^{18}O$ elastic scattering and the fit with the coupled channel method are plotted (Ka 77). The parameters of the optical potential as input for the calculation are the same as in table 6.

This potential was also employed in the calculation of total elastic scattering cross section (Coupled–channel method) and total fusion cross section (Hauser–Feshbach model). The parameters are:

V = 100 MeV R_r=6.289 fm a_r=0.51 fm.

W_i = 30 MeV R_i=6.813 fm a_i=0.30 fm.

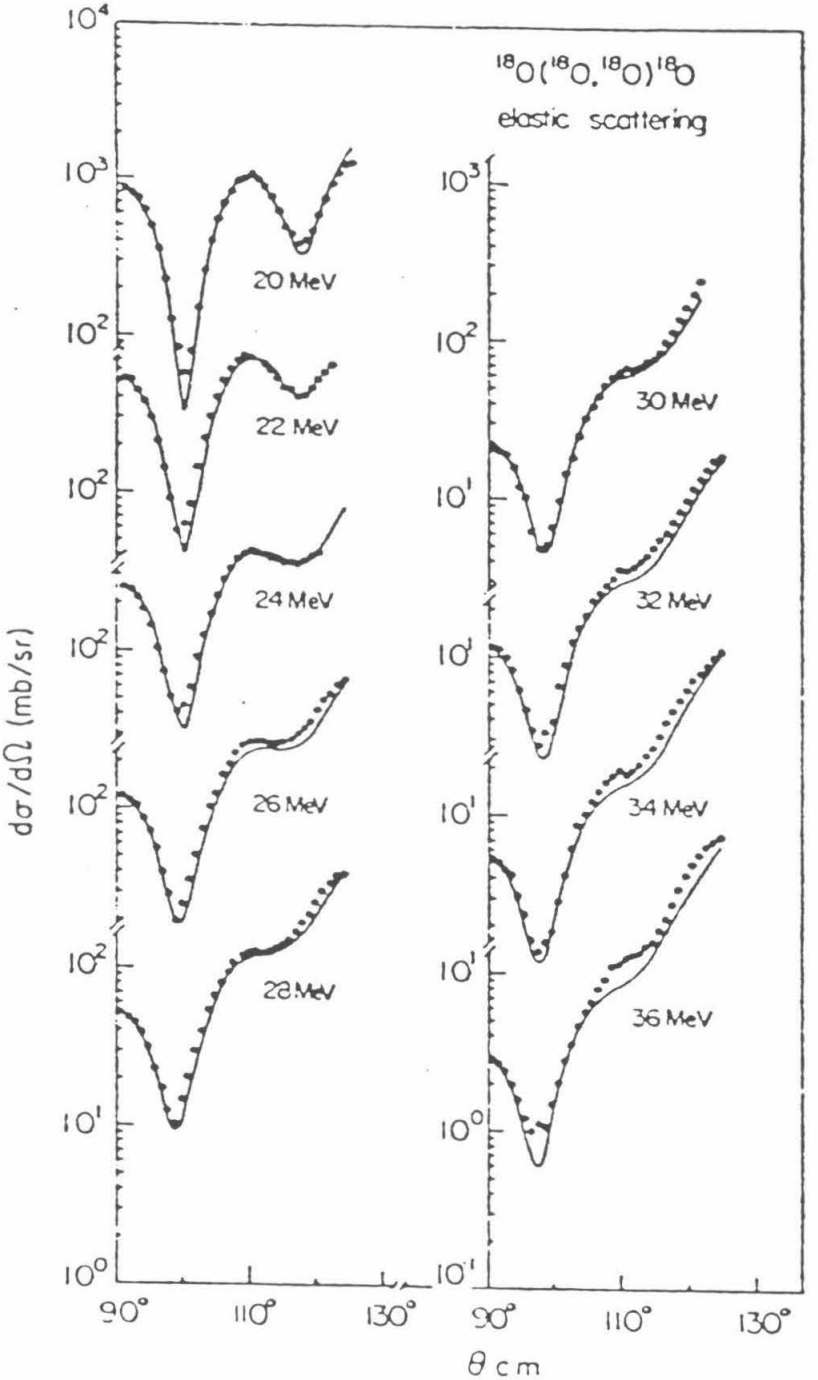
$^{18}O(^{18}O,^{18}O)^{18}O$
elastic scattering
20 MeV
22 MeV
24 MeV
26 MeV
28 MeV
30 MeV
32 MeV
34 MeV
36 MeV
dσ/dΩ (mb/sr)
θ c m
90°
110°
130°

FIGURE 27

$^{18}O + {}^{18}O$ Barrier from BKN Inversion

The $^{18}O + {}^{18}O$ barrier obtained from the one-dimensional BKN inversion procedure is shown as a function of C–M energy together with the uncertainty in the derived barrier.

For the $^{18}O + {}^{18}O$ fusion cross section:

The input barrier radius R_B = 8.59 fm.

The output barrier radius R_B = 8.92 fm.

The output barrier height V_B = 9.26 MeV.

To investigate why the barrier height determined for $^{18}O + {}^{18}O$ is so low, we input a false fusion cross section (66.7% of the true $^{18}O + {}^{18}O$ fusion cross section) to the IWBC program. The results are:

For the false fusion cross section (dotted curve):

The input barrier radius R_B = 8.59 fm.

The output barrier radius R_B = 8.92 fm.

The output barrier height V_B = 9.58 MeV.

The barrier for the S–wave optical potential used for the Hauser–Feshbach calculation is also plotted for comparison (dashed curve).

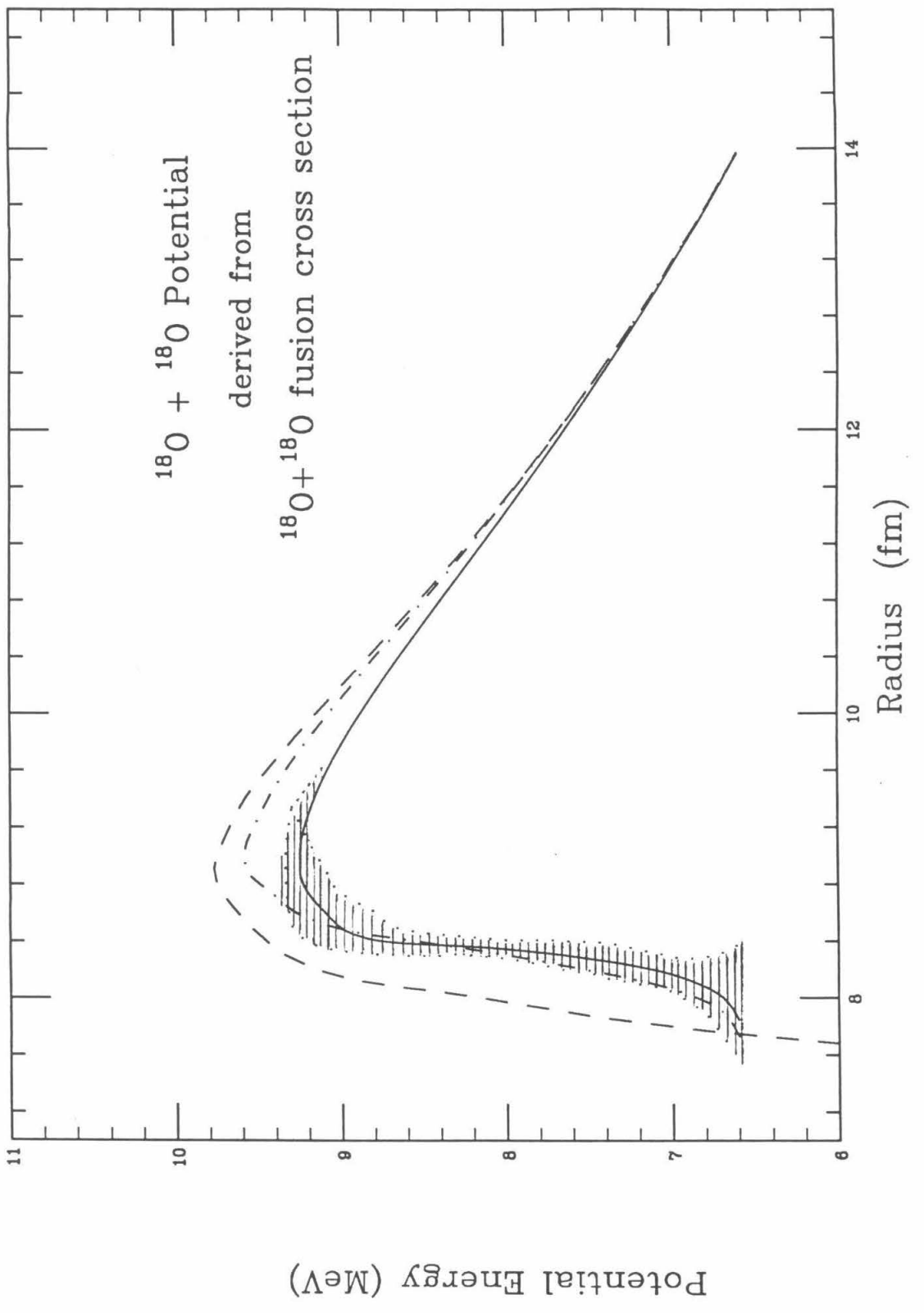
$^{18}O + ^{18}O$ Potential
derived from
$^{18}O+^{18}O$ fusion cross section
Potential Energy (MeV)
Radius (fm)
11
10
9
8
7
6
8
10
12
14

FIGURE 28

Oxygen Isotope Barriers from BNK Inversion

The Barriers between $^{16}O + ^{16}O$, $^{16}O + ^{17}O$, $^{16}O + ^{18}O$ *and* $^{18}O + ^{18}O$ are plotted together as functions of $E_{c.m}$. The last of these is the result of the present work, the others are from (Th 86).

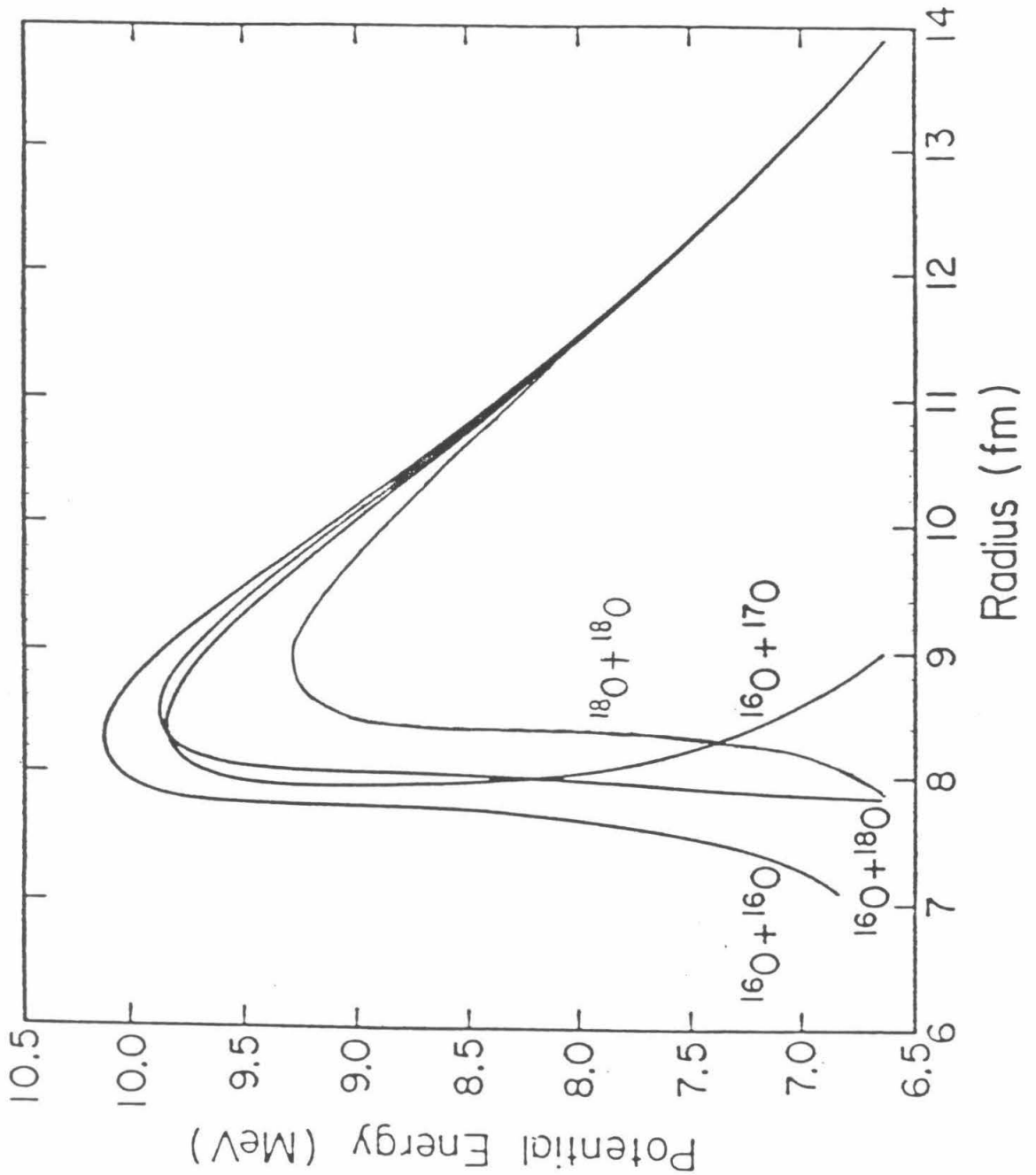
Potential Energy (MeV)
Radius (fm)
10.5
10.0
9.5
9.0
8.5
8.0
7.5
7.0
6.5
6
7
8
9
10
11
12
13
14
$^{16}O+^{16}O$
$^{16}O+^{18}O$
$^{16}O+^{17}O$
$^{18}O+^{18}O$

FIGURE 29

Fusion cross sections of oxygen isotopes Versus $E_{c.m} - V_B$

The total fusion cross sections between $^{16}O + ^{16}O$, $^{16}O + ^{17}O$, $^{16}O + ^{18}O$ and $^{18}O + ^{18}O$ are plotted together as functions of $E_{c.m} - V_B$. The last of these is the result of the present work, the others are from (Th 86). The barrier heights were calculated from the Akyuz—Winther model (Ak 80) for all of reactions.

The calculated barrier radii and heights are:

$^{16}O + ^{16}O$	$R_B = 8.2$ fm	$V_B = 10.34$ MeV
$^{16}O + ^{17}O$	$R_B = 8.3$ fm	$V_B = 10.24$ MeV
$^{16}O + ^{18}O$	$R_B = 8.4$ fm	$V_B = 10.14$ MeV
$^{18}O + ^{18}O$	$R_B = 8.6$ fm	$V_B = 9.95$ MeV

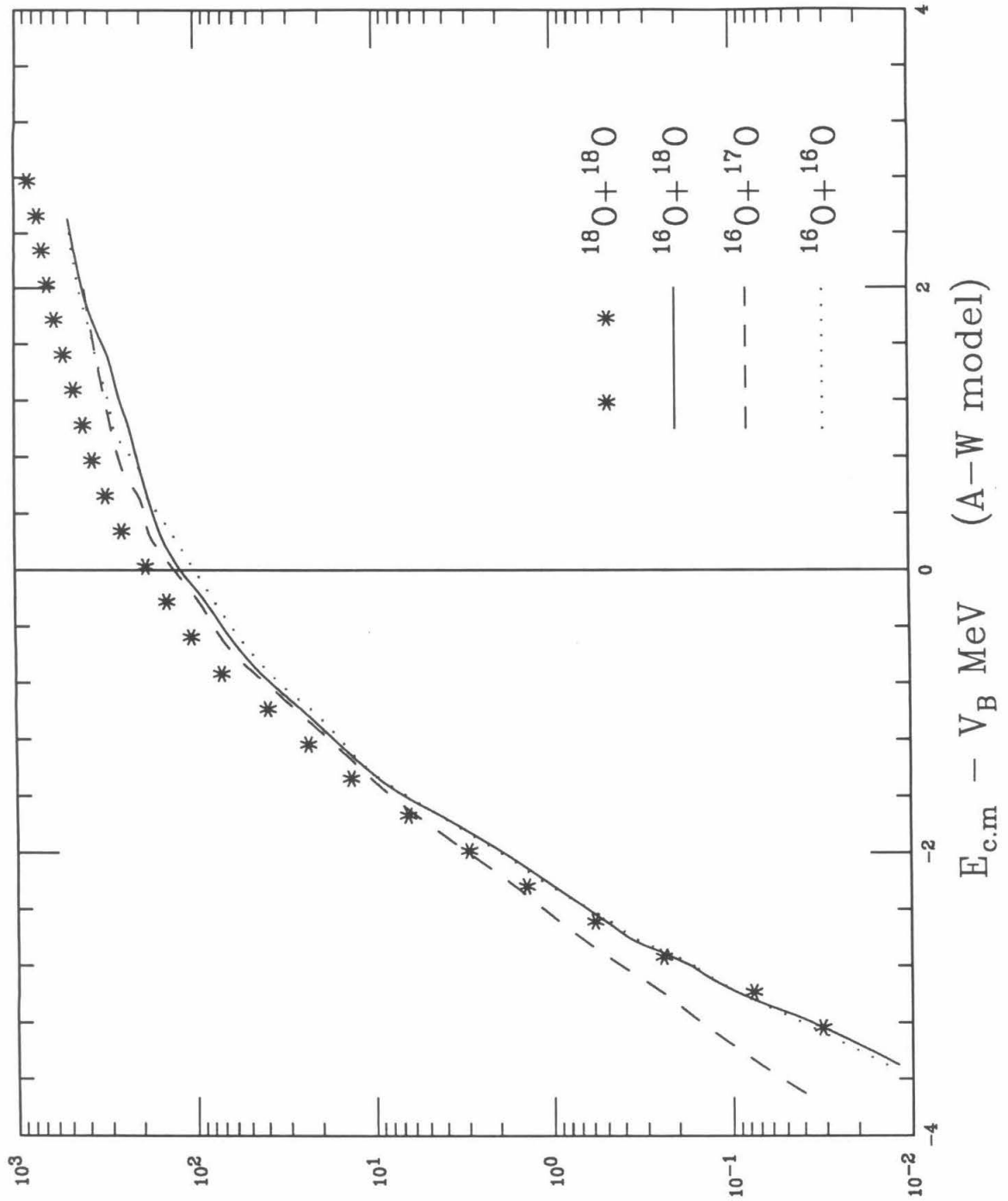
Cross Section (mb)
10^3
10^2
10^1
10^0
10^{-1}
10^{-2}
-4
-2
0
2
4
$E_{c.m} - V_B$ MeV
(A−W model)
$^{18}O+^{18}O$
$^{16}O+^{18}O$
$^{16}O+^{17}O$
$^{16}O+^{16}O$

Figure 30

Cross Section for $^{18}O + ^{18}O$ Inelastic Scattering

The experimental data from the present work are shown. The dashed curve represents the cross section as given by the semiclassical Coulomb excitation theory. The solid curve is the result of a DWBA calculation for the nuclear excitation. The details of these theoretical calculations are given in section V.C. The two vertical dotted lines plotted here show the three energy regions. From low energy to high energy, the regions are:

1. Pure Coulomb excitation;
2. Interference between Coulomb and nuclear excitation;
3. Mainly nuclear excitation.

In the DWBA calculation (Ku 87), the potential employed to produce the initial and the final distorted waves is that used to fit the elastic scattering and fusion cross sections.

$$\text{V} = 100 \text{ MeV} \quad R_r = 6.289 \text{ fm} \quad a_r = 0.51 \text{ fm}$$

$$W_i = 30 \text{ MeV} \quad R_i = 6.813 \text{ fm} \quad a_i = 0.30 \text{ fm}$$

The single–particle form factor is given by the potential (between one of the projectile nucleons and the target nucleus):

$$V' = 100 \text{ MeV} \quad R'_r = 6.080 \text{ fm} \quad a'_r = 0.68 \text{ fm}$$

$$W'_i = 0.0 \text{ MeV}$$

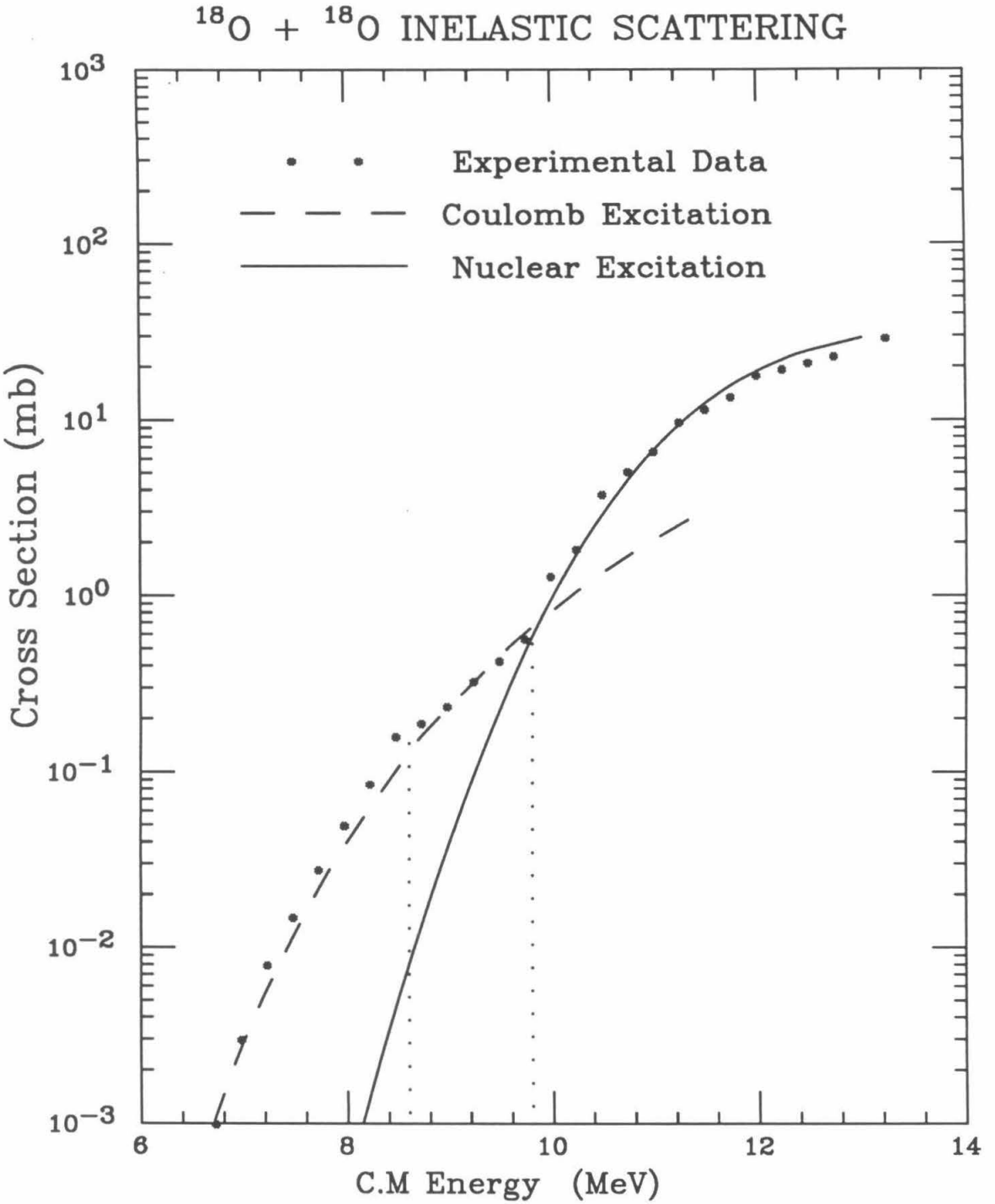
^{18}O + ^{18}O INELASTIC SCATTERING
Experimental Data
Coulomb Excitation
Nuclear Excitation
Cross Section (mb)
10^3
10^2
10^1
10^0
10^{-1}
10^{-2}
10^{-3}
6
8
10
12
14
C.M Energy (MeV)

Figure 31

The different shapes of the 1274 keV γ–ray peak

The shape of the structure of the 1274 keV γ–ray peak does not vary much with beam energy when $E > 20$ MeV. However, for $E < 20$ MeV, the lower the beam energy, the stronger (relatively) the sharp, unshifted peak becomes. See section V.D for details.

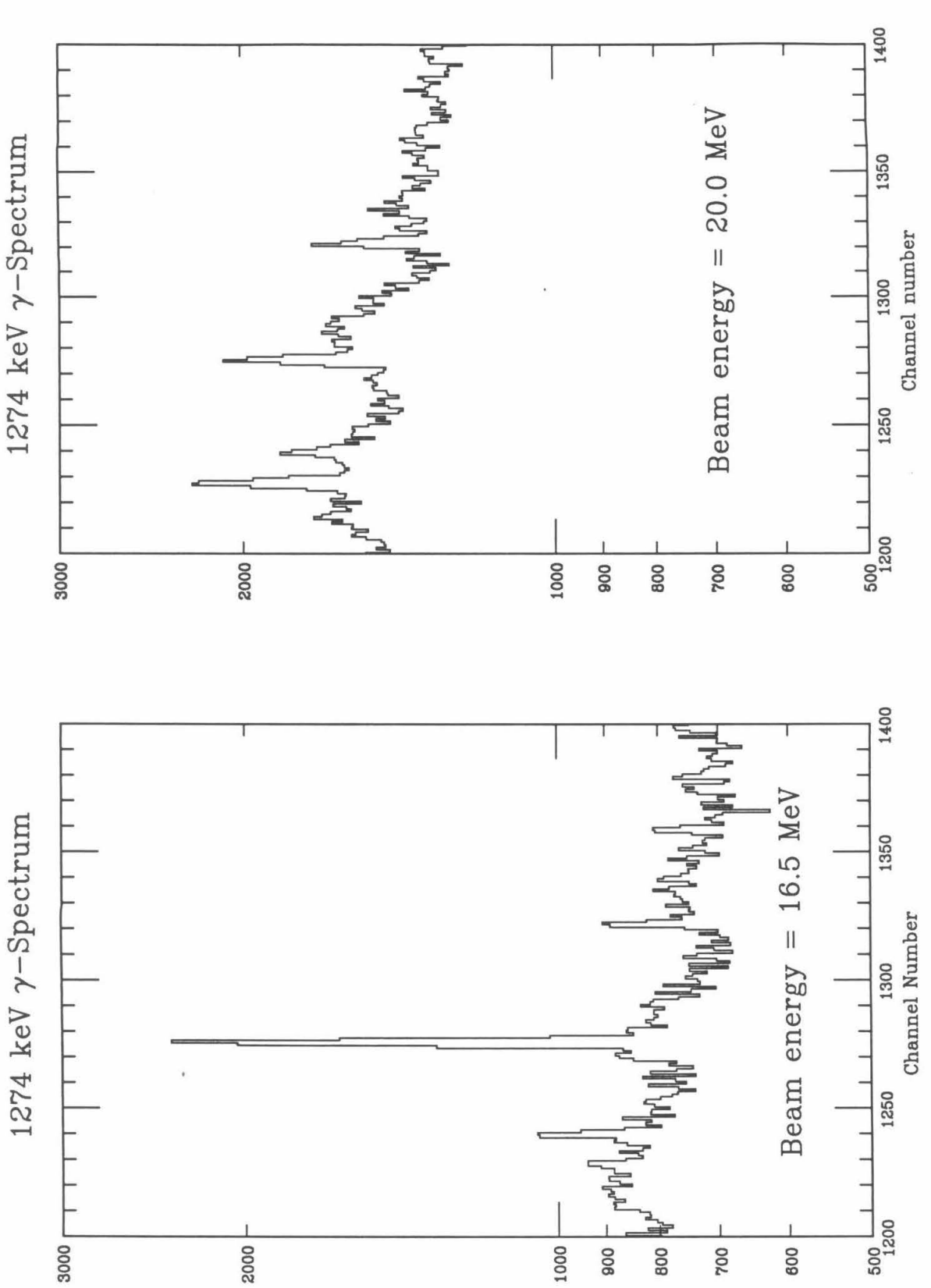
1274 keV γ−Spectrum
Beam energy = 20.0 MeV
1274 keV γ−Spectrum
Beam energy = 16.5 MeV
Channel number
Channel Number

Figure 32

Cross Section for $^{18}O + ^{18}O$ 2n–Transfer Reaction

The experimental data from the present work are shown. The solid curve represents the cross section as given by the DWBA calculation, described in section V.D.

Same potential was employed to produce the initial and the final distorted waves.

$$\text{V} = 100 \text{ MeV} \quad R_r = 6.552 \text{ fm} \quad a_r = 0.51 \text{ fm}$$

$$W_i = 30 \text{ MeV} \quad R_i = 6.552 \text{ fm} \quad a_i = 0.30 \text{ fm}$$

To compute a two–particle type form factor, the potential used here is:

$$V' = 47 \text{ MeV} \quad R'_r = 5.72 \text{ fm} \quad a'_r = 0.66 \text{ fm}$$

$$W'_i = 0.0 \text{ MeV}$$

The two valence neutrons of ^{18}O were assigned to the $d_{5/2}$ states.

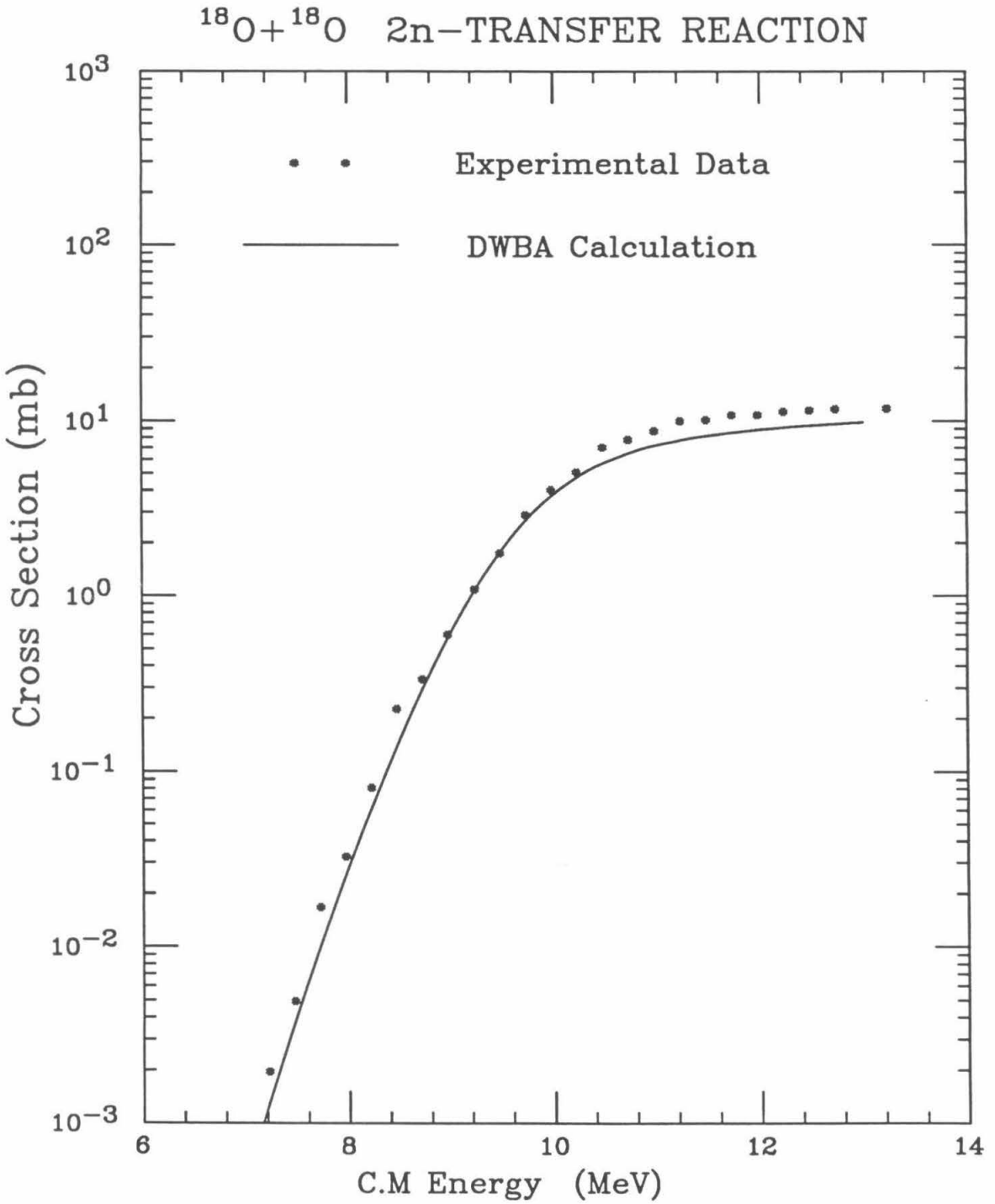
$^{18}O+^{18}O$ 2n−TRANSFER REACTION
Experimental Data
DWBA Calculation
Cross Section (mb)
10^3
10^2
10^1
10^0
10^{-1}
10^{-2}
10^{-3}
6
8
10
12
14
C.M Energy (MeV)

FIGURE 33

Cross Sections of Oxygen Isotope Reactions

The total fusion cross sections between pairs of oxygen isotopes obtained from earlier work in Kellogg Radiation Lab (Th 86) and the present study are plotted together as functions of C–M energy. The inelastic scattering cross sections for $^{16}O + {}^{17}O$, $^{16}O + {}^{18}O$ and $^{18}O + {}^{18}O$ are also shown. The reaction cross section for the two neutron transfer reaction $^{18}O + {}^{18}O \longrightarrow {}^{16}O + {}^{20}O$, is plotted as well.

REACTIONS BETWEEN OXYGEN ISOTOPES

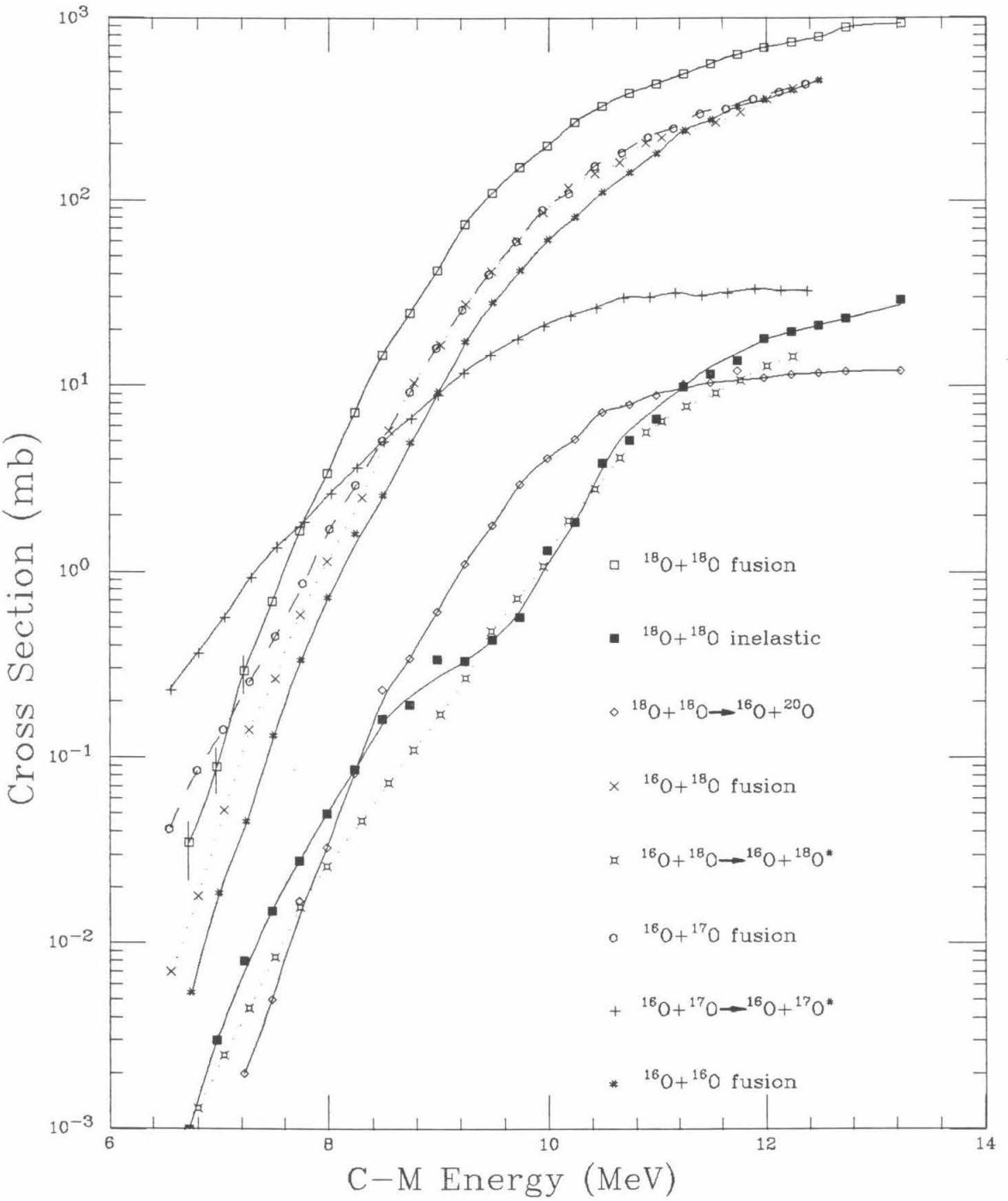

FIGURE 34

Reaction of Oxygen Isotopes with ^{12}C

The fusion cross sections of ^{16}O, ^{17}O, and ^{18}O with ^{12}C at sub–barrier energies were published in (Ey 76). This study found an increase of the interaction radii and a decrease of the barrier heights with an increase of the oxygen isotope mass.

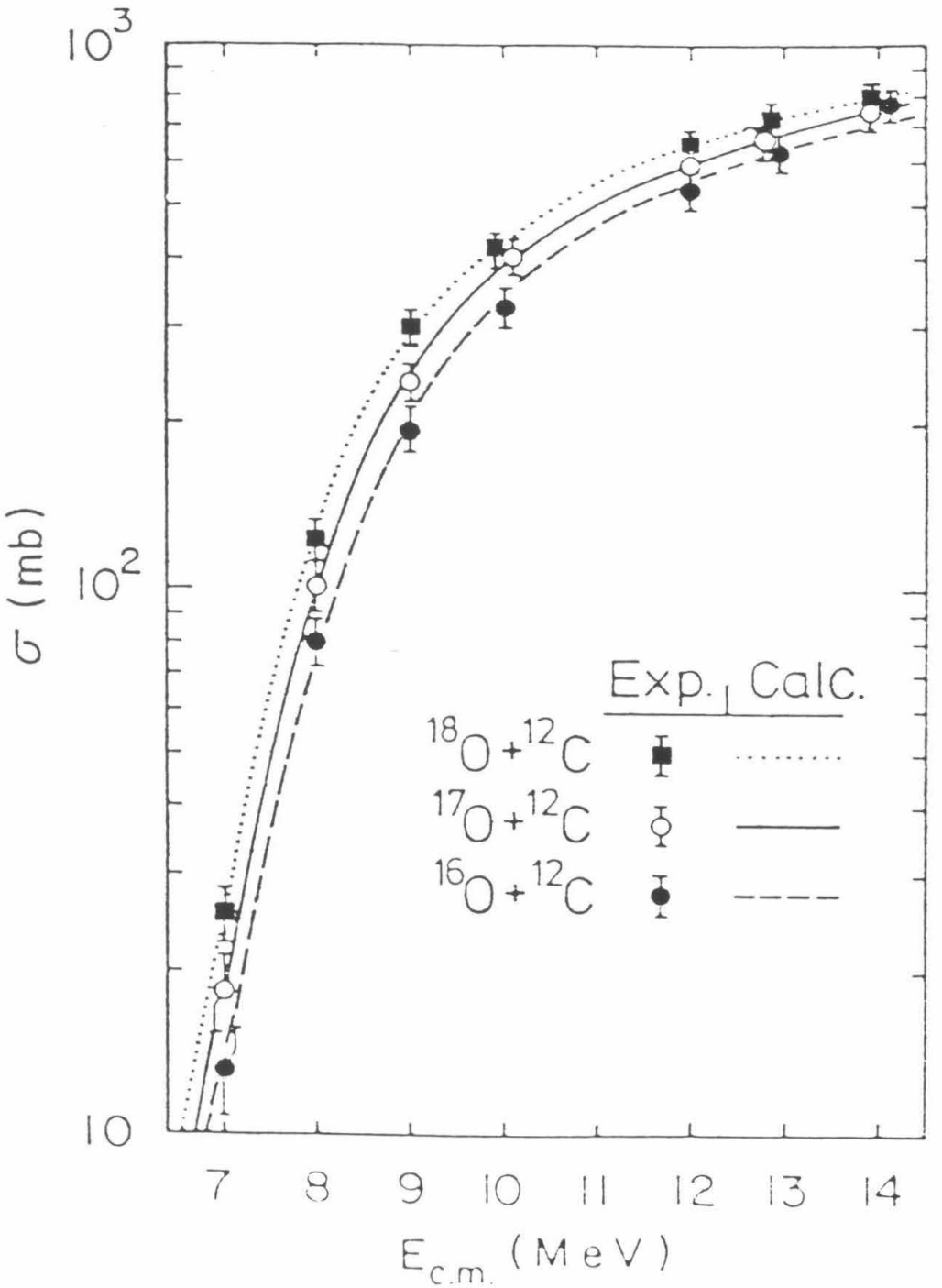
10^3
10^2
10
σ (mb)
7
8
9
10
11
12
13
14
$E_{c.m.}$ (MeV)
Exp. | Calc.
$^{18}O + ^{12}C$
$^{17}O + ^{12}C$
$^{16}O + ^{12}C$

FIGURE 35

Reaction of Oxygen Isotopes with ^{27}Al

This fusion cross sections of ^{16}O, ^{17}O and ^{18}O with ^{27}Al at above–barrier energies were published in (Ei 77). This study was for the same purpose as in (Ey 76), and again showed that the cross sections increase with the oxygen isotope mass.

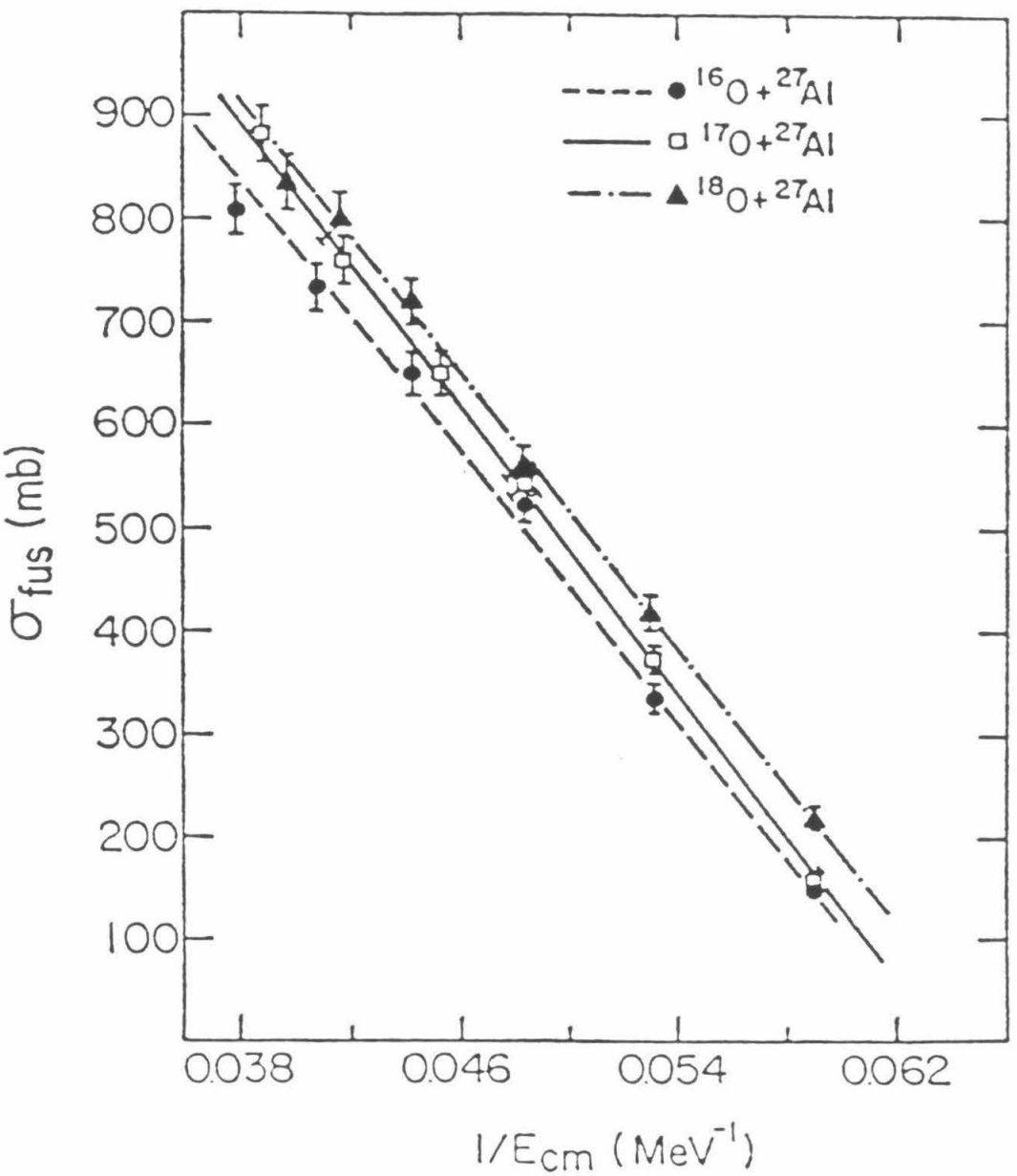
$^{16}O+^{27}Al$
$^{17}O+^{27}Al$
$^{18}O+^{27}Al$
900
800
700
600
500
400
300
200
100
σ_{fus} (mb)
0.038
0.046
0.054
0.062
$1/E_{cm}$ (MeV^{-1})